UNIVERSITY OF CALIFORNIA
Santa Barbara

Image Reconstruction for Multistatic Stepped Frequency-Modulated Continuous Wave (FMCW) Ultrasound Imaging Systems With Reconfigurable Arrays

A Dissertation submitted in partial satisfaction
of the requirements for the degree of

Doctor of Philosophy

in

Electrical and Computer Engineering

by

Michael Lee

Committee in Charge:

Professor Michael Liebling, Chair

Professor Shivkumar Chandrasekaran

Professor Nadir Dagli

Professor Emeritus Ronald Iltis

March 2015

The Dissertation of
Michael Lee is approved:

Professor Shivkumar Chandrasekaran

Professor Nadir Dagli

Professor Emeritus Ronald Iltis

Professor Michael Liebling, Committee Chairperson

December 2014

Image Reconstruction for Multistatic Stepped Frequency-Modulated Continuous Wave (FMCW) Ultrasound Imaging Systems With Reconfigurable Arrays

by

Michael Lee

To Bobi.

Acknowledgements

As grateful as I am for the technical inspirations that have guided me to this point, the personalities behind them are what I will treasure most. Professor Liebling has not only been patient and understanding but also incredibly courageous in welcoming me to his group despite short notice. Some of the most genuinely friendly people I will ever meet were part of the Systems BioImaging Lab group and it is no wonder that our lab meetings had a uniquely pleasant atmosphere. Professors Chandrasekaran, Iltis, Dagli, and Hespanha have all been supportive in many ways from the very beginning. I cannot thank them enough.

I would also like to thank Val, Alex, and the ECE administration for their part in keeping the road smooth during this journey. With their consideration, I even had the opportunity to TA the ECE 130 sequence, which was a fun and challenging experience that taught me a lot about myself. There is little doubt in my mind that it will prove to be as crucial for my personal and professional growth as any other aspect of my graduate study.

To Mich, my parents, Uncle Mo, Daniel, the Autogolazo intramural soccer team, and all of my friends, thank you for making my life unforgettable in both big and small ways.

Curriculum Vitæ

Michael Lee

Education

2015	Ph.D. in Electrical and Computer Engineering,
	University of California, Santa Barbara.
2008	M.S. in Biomedical Engineering,
	University of California, Los Angeles.
2006	B.S. in Electrical Engineering,
	University of California, Santa Barbara.

Academic Appointments

2012 – 2014	Graduate Teaching Assistant, ECE 130A-B-C (Signal Analysis),
	University of California, Santa Barbara.
2011 – 2013	Graduate Student Researcher,
	University of California, Santa Barbara.
2008 – 2011	Graduate Student Researcher,
	University of California, Los Angeles.

Awards

2013	Outstanding ECE Teaching Assistant Award 2012-2013, University of California, Santa Barbara.
2011	Graduate Student Paper Award, 2nd place, International Telemetering Conference.
2002 – 2006	Regents Scholarship, University of California, Santa Barbara.
2005	Joseph J. Sayovitz Scholarship, University of California, Santa Barbara.
2004	Undergraduate Student Paper Award, 2nd place, International Telemetering Conference.
2003	Venkataraman Scholarship, University of California, Santa Barbara.
2002	National Semiconductor-Monticelli Fellowship, University of California, Santa Barbara.
2002	Anna Bell Karr Scholarship, University of California, Santa Barbara.
2002	Raytheon Company Ventures Scholarship.

Selected Publications

Michael Lee, Rahul S Singh, Martin O Culjat, Shyam Natarajan, Brian P Cox, Elliott R Brown, Warren S Grundfest, and Hua Lee. Waveform synthesis for the design and image reconstruction of step FMCW ultrasound imaging systems with conformal transducer arrays. In *SPIE Medical Imaging*, pages 72650C–72650C. International Society for Optics and Photonics, 2009

Michael Lee, Rahul S Singh, Martin O Culjat, Shyam Natarajan, Brian P Cox, Elliott R Brown, Warren S Grundfest, and Hua Lee. Space-time image reconstruction algorithm for diverse ultrasound transducer element distributions. In *Biomedical Imaging: From Nano to Macro, 2009. ISBI'09. IEEE International Symposium on*, pages 177–180. IEEE, 2009

Martin O Culjat, David B Bennett, Michael Lee, Elliott R Brown, Hua Lee, Warren S Grundfest, and Rahul S Singh. Polyimide-based conformal ultrasound transducer array for needle guidance. *Sensors Journal, IEEE*, 9(10):1244–1245, 2009

Martin O Culjat, Aaron E Dann, Michael Lee, David B Bennett, Peter G Schulam, Hua Lee, WS Grundfest, and Rahul S Singh. Transurethral ultrasound catheter-based transducer with flexible polyimide joints. In *Ultrasonics Symposium (IUS), 2009 IEEE International*, pages 2209–2212. IEEE, 2009

Rahul S Singh, Shyam Natarajan, Michael Lee, AE Dann, Brian P Cox, David B Bennett, Elliott R Brown, Hua Lee, Warren S Grundfest, and Martin O Culjat. Development of an ultrasound imaging system for needle guidance. In *Ultrasonics Symposium (IUS), 2009 IEEE International*, pages 1852–1855. IEEE, 2009

Michael Lee, Rahul S Singh, Martin O Culjat, Scott Stubbs, Shyam Natarajan, Elliott R Brown, Warren S Grundfest, and Hua Lee. Designing multistatic ultrasound imaging systems using software analysis. In *SPIE Medical Imaging*, pages 76290S–76290S. International Society for Optics and Photonics, 2010

Shyam Natarajan, Rahul S Singh, Michael Lee, Brian P Cox, Martin O Culjat, Hua Lee, and Warren S Grundfest. Step-FMCW signaling and target

detection for ultrasound imaging systems with conformal transducer arrays. In *BiOS*, pages 75550M–75550M. International Society for Optics and Photonics, 2010

Shyam Natarajan, Rahul S Singh, Michael Lee, Brian P Cox, Martin O Culjat, Warren S Grundfest, and Hua Lee. Accurate step-FMCW ultrasound ranging and comparison with pulse-echo signaling methods. In *SPIE Medical Imaging*, pages 76290D–76290D. International Society for Optics and Photonics, 2010

Michael Lee, W. S. Grundfest, and Hua Lee. Image reconstruction and resolution enhancement algorithm for FMCW medical ultrasound imaging systems. In *Proceedings of International Telemetering Conference*. International Foundation for Telemetering, 2011

Michael Lee and Daniel Doonan. Resolution analysis and system integration of a dynamically reconfigurable FMCW medical ultrasound imaging system. In *Proceedings of International Telemetering Conference*. International Foundation for Telemetering, 2012

Michael Lee and Daniel Doonan. Estimation and correction of quadrature-receiver phase errors of stepped-frequency FMCW systems for high-resolution imaging. In *Proceedings of International Telemetering Conference*. International Foundation for Telemetering, 2012

Michael Lee and Hua Lee. Modeling imaging performance of multistatic acoustic arrays of non-uniform geometries. *The Journal of the Acoustical Society of America*, 134(5):4170–4170, 2013

Abstract

Image Reconstruction for Multistatic Stepped Frequency-Modulated Continuous Wave (FMCW) Ultrasound Imaging Systems With Reconfigurable Arrays

Michael Lee

The standard architecture of a medical ultrasound transducer is a linear phased array of piezoelectric elements in a compact, hand-held form. Acoustic energy not directly reflected back towards the transducer elements during a transmit-receive cycle amounts to lost information for image reconstruction. To mitigate this loss, a large, flexible transducer array which conforms to contours of the subjects body would result in a greater effective aperture and an increase in received image data. However, in this reconfigurable array design, element distributions are irregular and an organized arrangement can no longer be assumed. Phased array architecture also has limited scalability potential for large 2D arrays.

This research work investigates a multistatic, stepped-FMCW modality as an alternative to array phasing in order to accommodate the flexible and reconfigurable nature of an array. A space-time reconstruction algorithm was developed for the imaging system. We include ultrasound imaging experiments and describe a simulation method for quickly predicting imaging performance for any given

target and array configuration. Lastly, we demonstrate two reconstruction techniques for improving image resolution. The first takes advantage of the statistical significance of pixel contributions prior to the final summation, and the second corrects data errors originating from the stepped-FMCW quadrature receiver.

Contents

List of Figures

List of Tables

Chapter 1

Introduction

1.1 Conventional Medical Ultrasound Imaging

An ultrasound imaging transducer interrogates a region of interest by transmitting acoustic pressure waves into the region. As the waves propagate, reflections occur where there exist changes in acoustic properties, notably at interfaces between two different materials. In medical ultrasound imaging, the largest reflections often occur at the interfaces between organs and between tissue types [7], [41]. The timing of the reflected wave energy received by the transducer therefore contains information about the interface distances from the transducer. Processing the received data is then used to form an image that estimates the physical distributions within the region. The ultrasound transducer consists of an array of piezoelectric transceiver elements [16]. These individual elements are capable of transmitting and receiving acoustical energy and are in direct contact with the

region of interest during data acquisition. The manner in which the elements operate in concert during this process defines the modality of the imaging system.

With few exceptions, commercial medical ultrasound imaging systems operate in a phased-array modality, as overviewed in Fig. 1.1. This technique most often refers to a scanning of the region of interest by transmitting short pulses from each element [13]. By programming delay times into the transmission of the elements, the transmitted pulses are directed at a desired focal point in the region. Received reflected energy is then processed similarly and in reverse fashion. The data for a full image frame is acquired once this process is repeated for each point in the scan [7].

Depending on its application, medical ultrasound imaging systems typically operate with waveforms between 1 and 15 MHz with imaging resolutions between 3 mm and 0.3 mm [58]. Ultrasound has several important advantages over other forms of imaging: It is much less costly than computed tomography (CT) imaging and magnetic resonance imaging (MRI), can be done with portable systems, does not subject the patient to ionizing radiation, and can achieve high frame rates. Poor penetration depth remains one of its main weaknesses (Table 1.1). Although using higher waveform frequencies improves the achievable resolution, it also increases the attenuation of acoustic waves in the medium which lowers SNR [7].

This tradeoff between penetration depth and resolution is a fundamental consideration in ultrasound system applications.

Table 1.1: Comparison of Common Medical Imaging Forms (Szabo, 2004)

Parameter	**Ultrasound**	**X-ray**	**CT**	**MRI**
Properties imaged	Mechanical	Mean tissue absorption	Tissue absorption	Biochemical
Scanner positioning	Small window	Two opposing sides	Circumferential	Circumferential
Spatial resolution	0.3–3 mm	$\sim$ 1 mm	$\sim$ 1 mm	$\sim$ 1 mm
Penetration	3–25 cm	Excellent	Excellent	Excellent
Safety	Very good	Ionizing radiation	Ionizing radiation	Very good
Speed	100 frames/sec	Minutes	$^1/_2$ minute to minutes	10 frames/sec
Cost	Low	Low	Very high	Very high
Portability	Excellent	Good	Poor	Poor

1.2 Synthetic Aperture Imaging in Ultrasound

As arrays become larger in effort to imaging performance, the orchestration of these delays in a phase-array modality becomes a challenge with regard to the electrical connections and frame rate [29]. For this reason, much of the research in ultrasound imaging is devoted to alternate methods of transmit-receive.

(a) Common medical ultrasound environment for fetal imaging. (Credit: Siemens Healthcare Inc., ref. [23])

(b) Ultrasound image of a human fetus in the womb. (Credit: Siemens Healthcare Inc., ref. [24])

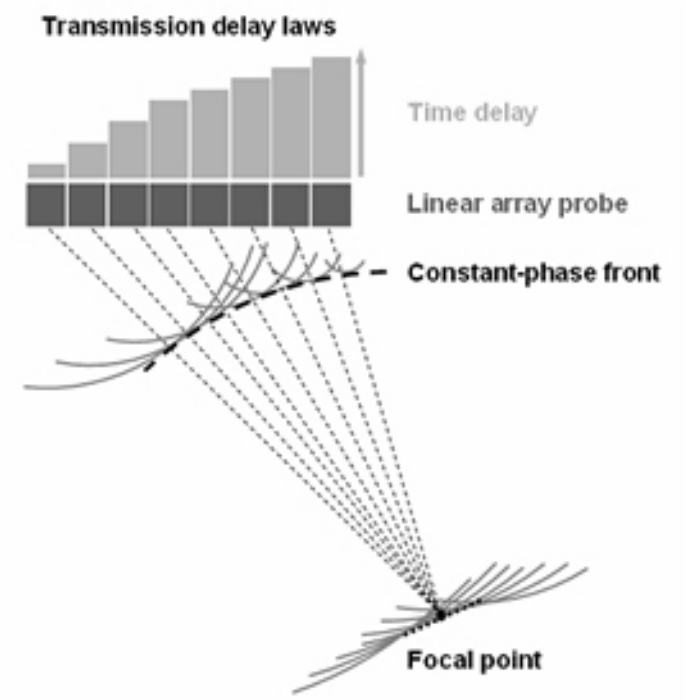

(c) Standard in modern ultrasound, phased-imaging relies on transmitting and receiving wave energy on a point-by-point basis within the region of interest. This is accomplished with a linear array of transceiver elements. (Credit: Neau and Hopkins, 2006 [46].)

Figure 1.1: Commercial ultrasound operation.

One alternative which is gaining attention is known as the synthetic aperture focusing technique (SAFT) [57]. Instead of using time delays to direct energy at a particular point, this technique traverses across each element in the array, having it transmit as the other elements receive. This is known as multistatic operation. After each element has transmitted, a full set of data will have been acquired to reconstruct an image frame. Because this modality relies on channel multiplexing, the electrical connections are simpler than for phased-arrays [10], which suggests promise for large arrays. On the other hand, synthetic aperture techniques often suffer from low signal-to-noise ratio (SNR) on receive [29] and imaging artifacts, making it a prime candidate for modification and further research [59].

Although radar imaging is based on electromagnetic wave propagation, the wave equation for pressure waves shares the same form, permitting the application of radar approaches to ultrasound array processing [26]. A growing imaging modality in radar and in ground-penetrating radar (GPR) in particular is Stepped-Frequency Continuous Wave (SFCW), or Stepped Frequency-Modulated Continuous Wave (Stepped-FMCW). This technique involves transmitting a sequence of tones in lieu of a short pulses. Hence, processing this data can be considered a frequency-domain data-acquisition method [38]. Its advantages over pulsed techniques in the GPR field include greater measurement accuracy, greater dynamic

range, and lower noise [20]. We therefore hypothesize that stepped-FMCW might bring similar benefits in the ultrasound field.

1.3 Motivation and Project Novelty

At its core, this imaging project is predicated on the assumption that for two multistatic ultrasound imaging systems with identical computing and bandwidth resources, the ability to resolve targets within a region of interest will be greater when imaging with (B) than with (A):

(A) Array with M transceiver elements distributed across a rigid transducer of area N held against the body.

(B) Array with M transceiver elements distributed across a flexible transducer of area $> N$ conforming to the contours of the body.

Although there may be operational schemes adapted for particular systems that may challenge the scope of this statement, the reasoning is less debatable: Using a larger array to image a region of interest will create more target reflections from more angles and receive more of those energies back. Additionally, an array that can conform to contours of the body will further these increases. Such an array will be more broadly referred to as "reconfigurable," in that its elements can be easily changed between imaging cycles. The result is a dataset that contains

more information about the target distribution. We will show that with more array aperture span, image reconstruction of a target distribution will have higher SNR and resolution.

However, the fabrication of a large, scalable array increases the difficulty of maintaining the conventional phased-array mode of operation, as discussed previously. If it is accepted that pushing the limits of array size requires simplification of electrical connections and forgoing of complex transmission and receive schemes, a secondary technical question arises: What simpler transmission and receive scheme could be used for a large array, and what would be its image reconstruction algorithm? This thesis investigates this question and proposes one possible solution.

It has been noted that barriers between imaging fields, possibly stemming from specialized terminology and long-held traditions in methodology, have resulted in slowed migration of imaging techniques across fields [59].

The novelty of this project lies in the adaptation of the stepped-FMCW imaging modality with multistatic synthetic aperture array operation for application in a flexible array imaging system. Fig. 1.2 provides a visual overview. The success seen with stepped-FMCW in ground-penetrating radar research motivates investigation in its application ultrasound imaging. With the exploration of both synthetic aperture techniques and stepped-FMCW for flexible ultrasound arrays,

the development of a process by which this imaging sytem can be analyzed for performance will be a valuable new tool for guiding its realization in medicine and non-destructive evaluation (NDE).

Literature searches on multistatic ultrasound imaging yield efforts which were by and large limited to investigation of a single array configuration (such as relating to intravascular imaging or annular arrays [53],[49],[61]) and pulse-echo data acquisition instead of stepped-FMCW [12],[27],[28]. Some ultrasound work has included stepped-FMCW imaging but does not involve multistatic operation [48]. The pairing of the stepped-FMCW modality with multistatic data acquisition is a novel setting for ultrasound imaging, and when combined with the design constraint of an arbitrary array configuration, provides new grounds for image simulation.

1.4 Thesis Organization

Four main chapters form the basis of this dissertation. Chapter 2 of this thesis provides an overview of **coherent imaging in two dimensions**, which leads to the formulations of resolving capability for multistatic stepped-FMCW system. Next, Chapter 3 focuses on **how target ranging is achieved with a stepped-FMCW system**. Since this modality replaces the more traditional pulse echo

(a) Probing the neck using a standard phased-array transducer. (Credit: University of South Carolina, School of Medicine, ref. [2])

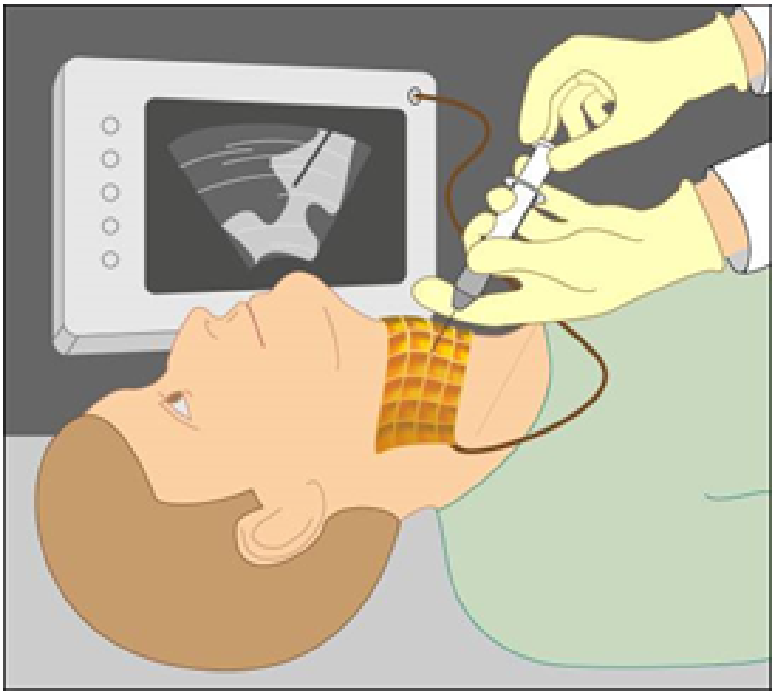

(b) A large flexible array used for neck imaging could improve the performance of needle guidance procedures.(Credit: CASIT at UCLA)

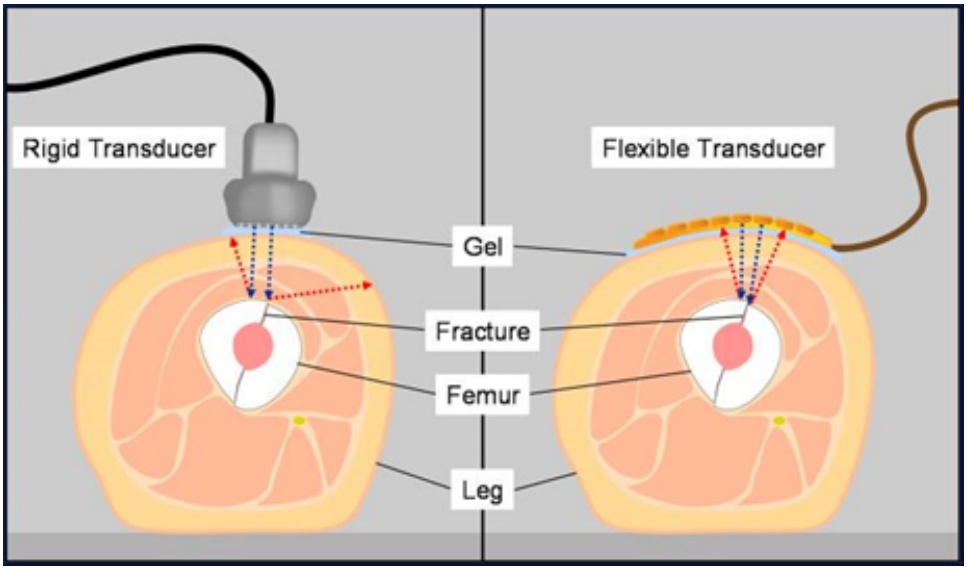

(c) Imaging through a curved surface would benefit from the reconfigurable array geometry and maximize energy transmission and reception. (Credit: CASIT at UCLA)

Figure 1.2: A reconfigurable ultrasound array can conform to bodily contours during the imaging process.

approach, we explain their mathematical equivalence in supplying range information. A brief summary about system architecture is given, which includes laboratory experiment results. This is followed by Chapter 4, which is devoted to the space-time **image reconstruction algorithm** of a multistatic, stepped-FMCW system for reconfigurable arrays. Its counterpart, spatial-frequency reconstruction, is also discussed for completeness. Equivalent reconstructions with both methods are shown by using a single GPR dataset. We then present the space-time reconstruction using which a needle was imaged with a multistatic, reconfigurable ultrasound array. Lastly, a system image simulation method is de-

scribed whose results are aligned with theoretical predictions. Chapter 5 presents **two techniques for improving imaging resolution** by additional modules in the reconstruction algorithm. The first takes advantage of the statistical significance of pixel contributions prior to the final summation, and the second corrects data errors originating from the stepped-FMCW quadrature receiver.

1.5 Perspectives from Related Fields

The direction of this project is heavily influenced by contributions from two fields outside of what is commonly associated with ultrasound: (1) synthetic aperture radar (SAR) [42],[50], (2) multiple-input and multiple-output (MIMO) radar arrays [64],[21],[18],[22]. Sensor networks, particularly underwater acoustic sensor networks (UASNs) [14],[25],[5] share similar localization goals with those of this ultrasound thesis, however, fundamental differences in their environments limit more direct association. To better acquaint the reader with the lineage of this project, some clarifications and comparisons to these research areas are presented.

1.5.1 Synthetic Aperture Radar (SAR)

Synthetic aperture radar forms images, typically of landscapes, by aggregating the information collected by a single radar device as it moves over an area of

interest. Since the lone radar's physical dimensions constitute its true aperture, the data acquired through its movement across space mimics that of a system of many radars in concert. This creates a much larger, "synthetic" aperture which increases the resolution of the reconstructed image. Noting the relationship between image resolution and aperture size, this thesis hypothesizes that similar gains in image quality can be achieved in ultrasound imaging by designing for a large, scalable transducer array.

Since both SAR and medical ultrasound systems share the common signaling modality of pulse echo, insight into alternative SAR signaling modalities also shed light on possibilities in the ultrasound research domain. Most notably, migration from pulsing to continuous wave (CW) operation for SAR saw the same advantages [42] as GPR, including hardware complexity reduction, lower peak power, and lower cost. These features are especially attractive for ultrasound researchers, not only to combat the growing complexity of pulse echo arrays but to preserve medical ultrasound's crown as the lowest cost and most portable imaging option.

Imaging reconstruction techniques for SAR have also guided the direction of this thesis. SAR literature describes two chief image formation methods: frequency-based and time-based. Specifically, time-domain SAR image formation offers "direct adaptability to non-regular sampling schemes," and the ability "to deliver output image on a custom grid" and "focus the SAR data from arbi-

trary bistatic configurations" [50]. In this thesis where ultrasound elements may assume arbitrary positions with non-uniform spacing, space-time reconstruction becomes the clear choice for many of the same reasons seen in SAR research.

1.5.2 Multiple-Input and Multiple-Output (MIMO) Radar

Unlike SAR which captures images by a moving scan, a multistatic system is defined as a system of multiple, independent radars capable of local signal processing that are centralized via a communication link [6],[3],[4],[60]. Adoption of this term by the ultrasound community helps describe the manner in which individual ultrasound array elements transmit and receive signals independently, distinguishing the operation from the phased-array modality.

Considered a type of multistatic radar, MIMO radar systems refer to a static array capable of multiple transmit waveforms, with joint receivers that allow signals to be processed as a whole. Therefore it can said that the multistatic ultrasound array of this project is also MIMO, given its stepped-frequency CW transmission and that the detection of phase delays and transit-receive timing requires orchestration across the entire array. MIMO radars with widely separated antennas (as opposed to co-located antennas) most closely represent the nature of this thesis. Radar performance is improved by their ability to overcome challenges with radar cross-section (RCS) diversity [17]. This is due to multitude of target

perspective angles afforded by a large aperture which supports high-resolution target localization [40],[18]. In contrast to phased-array radars, omnidirectional beamforming common to MIMO removes the need to scan a target region with a narrow beam, reducing cost in time for what is lost in processing gain. Bypassing of the scanning process is crucial for the reconfigurable ultrasound array because it nullifies the need for array-phasing recalculations prior to each imaging cycle. However, omnidirectionality of the ultrasound acoustic element beam may not assumed in practice. Thus with the reconfigurability of the array combined with directional beamspread, this thesis confronts the task of estimating imaging performance in an environment not common to MIMO radar.

Since phased-array and MIMO radars each have their own set of advantages and disadvantages, there have been many efforts to hybridize techniques to balance their strengths. For MIMO systems, antenna arrays can be grouped operationally into subarrays (a subset of antennas) that perform a specialized function within the array as a whole. One example is the phased-MIMO system [22] which refers to multiple phased subarrays working in aggregate in a MIMO structure. Further adaptations include phased-MIMO systems that feature phased subarrays steered by tuning frequency increments [64]. Like MIMO radar, research into subarray operations for multistatic ultrasound arrays have also been conducted. To address some of the SNR concerns associated with multistatic operation, some schemes

transmit and receive acoustic energy with various subarray patterns instead of elementally [27],[28]. This thesis does not explore this avenue and is limited in scope to single-element multistatic operation.

1.5.3 Underwater Acoustic Sensor Networks (UASNs)

Underwater acoustic sensor networks overlap with ultrasound imaging in two distinct ways: The acoustical aspect of its operation and the goal of localizing nodes or targets in the water. A core UASN problem is detection and tracking of underwater node positions for the purpose of relaying information gathered by the nodes [14]. By employing underwater transceivers with known positions (anchors), peripheral nodes in the network can be mapped using a variety of schemes [25],[1]. In some situations, nodes can both transmit and receive signals from the anchors and other nodes. In others applications, nodes can only passively receive, known as *silent positioning* [5].

Drawing an analogy for reconfigurable array ultrasound imaging would have the ocean correspond to bodily tissue and nodes/anchors to transceiver elements. Unfortunately, many of the resources and localization strategies available to UASNs are not available for ultrasound imaging. For example, Global Positioning Systems (GPS), pressure systems for depth estimation, and accelerometers are all common tools in UASNs but have no applicability or an analogous form in an ultrasound

imaging environment. Additionally, because ultrasound imaging is non-invasive, there is no opportunity to track targets by insertion of a communication anchor within the body as UASNs do underwater. However, the ultrasound needle guidance scenario presents one possible exception. In that case, it would be conceivable to fabricate elements onto the shaft of the needle to allow for direct path signaling to the array on the skin's surface.

In UASNs, the capability exists for node-to-node or node-to-anchor communication in 3D space. By tracking time-of-arrival (ToA) and time-difference-of-arrival (TDoA), ranging can be achieved [15]. Though this has some similarity to time-domain radar image reconstruction, it is removed from relevant radar and ultrasound techniques where direct element-to-element path communication is not an objective. For a multistatic ultrasound array, beamspread limitations would deny most (if not all) elements a direct path linkage to another.

Chapter 2

Imaging With Coherent Waves

Because a stepped frequency-modulated continuous wave (FMCW) system transmits and receives continuous waves while tracking phase delays, the propagation of a single coherent wave represents the basic foundation of its operation. It will be used to describe the image reconstruction process as well as characterize the system resolution.

This chapter guides the reader from the simplest case of coherent imaging (single-receiver passive) to multistatic active imaging, the latter of which is fully relevant to this thesis. Each case includes resolution analysis by examination of spatial-frequency content.

Traditionally, the resolution analysis techniques in this section mirror those seen in the field of radar imaging. In radar literature, an aperture is commonly modelled as a rigid structure or a single point, with the assumption that target location distances greatly exceed the dimensions of the aperture itself. In our case,

those assumptions may not be the applicable. So instead of treating an array as a single entity, we treat the elements within the array as *individual* imaging components. This allows the analysis to hold for an arbitrary set of elements, whose aggregate forms the basis of the configurable array imaging system. Reference [33] forms the basis for this chapter.

2.1 Passive Imaging

Passive imaging involves reconstructing a source location by only receiving and recording the signal energy emanating from that source. One of the simplest cases of coherent imaging is a single point receiver operating passively in $\mathbb{R}^2$ as seen in Fig. 2.1(a). Consider a point source s located at (x_s, y_s) that emits (omnidirectionally and in a homogenous medium) a wave of fixed wavelength λ. A point receiver r located at (x_r, y_r) will detect the Green's function $h(x, y)$ evaluated at its location (x_r, y_r):

$$h(x_r, y_r) = \frac{1}{j\lambda r} \exp\left(j\frac{2\pi r}{\lambda}\right), \tag{2.1}$$

where $r = \sqrt{(x_s - x_r)^2 + (y_s - y_r)^2}$ with $r \gg \lambda$. It is important to note that although the Green's function in Eq. (2.1) holds specifically for $\mathbb{R}^2$, its counterpart

in $\mathbb{R}^3$ differs only by the amplitude function with its phase function remaining in the same form [56]:

$$h(x_r, y_r, z_r) = \frac{1}{r} \exp\left(j\frac{2\pi r}{\lambda}\right), \tag{2.2}$$

where $r = \sqrt{(x_s - x_r)^2 + (y_s - y_r)^2 + (z_s - z_r)^2}$. Because it is the phase function that plays the operative role in array imaging problems, transitioning from a two-dimensional imaging model to one of three dimensions does not present a fundamental change in the theoretical landscape.

Bringing our attention back to the two-dimensional case, formulation of the local spatial frequency at the receiver position will later allow for the introduction of resolution.

By definition, the local spatial frequency at (x_r, y_r) in the x-direction is the derivative of the phase of $h(x, y)$ with respect to x, evaluated at (x_r, y_r):

$$\begin{aligned} f_{x,r} &= \left[\frac{\partial}{\partial x}\left(\frac{r}{\lambda}\right)\right]\Bigg|_{x=x_r, y=y_r} \\ &= \left[\frac{\partial}{\partial x}\left(\frac{\sqrt{(x_s - x)^2 + (y_s - y)^2}}{\lambda}\right)\right]\Bigg|_{x=x_r, y=y_r} \\ &= \frac{1}{\lambda}\cos\theta_o, \end{aligned} \tag{2.3}$$

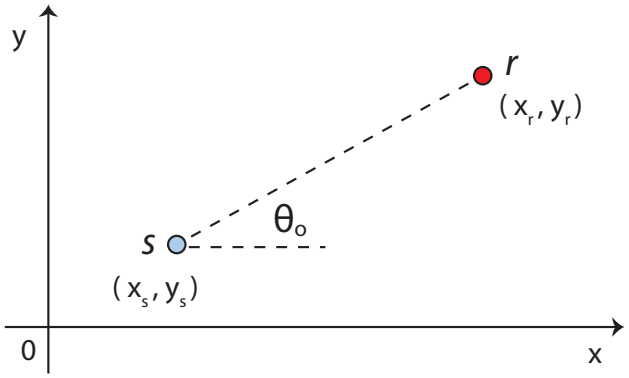

(a) Passive case setup space domain

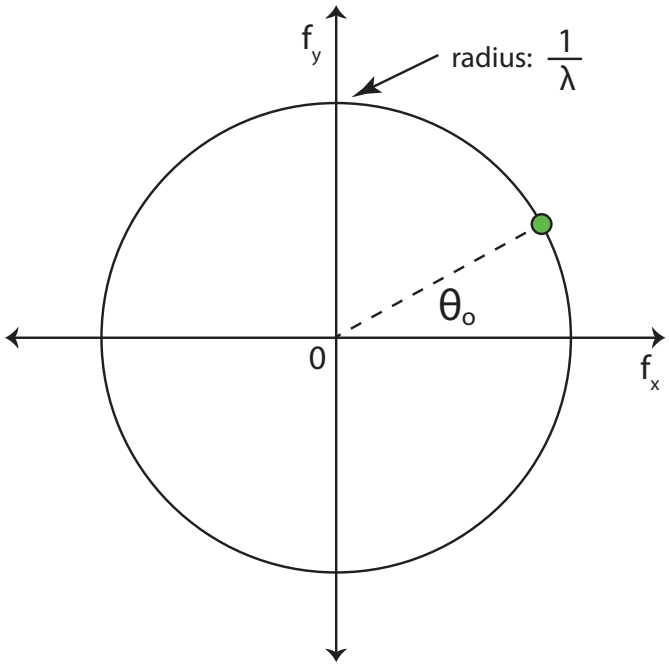

(b) Passive case setup spatial frequency domain

Figure 2.1: Passive Imaging Case

where θ_o is the perspective angle formed between the vector from s to r and the normal axis.

Similarly, the local spatial frequency at (x_r, y_r) in the y-direction is the derivative of the phase of $h(x, y)$ with respect to y, evaluated at (x_r, y_r):

$$\begin{aligned} f_{y,r} &= \left[\frac{\partial}{\partial y}\left(\frac{r}{\lambda}\right)\right]\Bigg|_{x=x_r, y=y_r} \\ &= \left[\frac{\partial}{\partial y}\left(\frac{\sqrt{(x_s-x)^2+(y_s-y)^2}}{\lambda}\right)\right]\Bigg|_{x=x_r, y=y_r} \\ &= \frac{1}{\lambda}\sin\theta_o, \end{aligned} \tag{2.4}$$

where θ_o is the perspective angle formed between the vector from s to r and the x-axis.

Because $f_{x,r}$ and $f_{y,r}$ are the orthogonal components in the spatial frequency domain (f_x, f_y), they can be represented as a vector $\mathbf{f_r}$ on the complex plane:

$$\begin{aligned} \mathbf{f_r} &= \begin{bmatrix} f_{x,r} \\ f_{y,r} \end{bmatrix} = \frac{1}{\lambda}\begin{bmatrix} \cos\theta_o \\ \sin\theta_o \end{bmatrix} \\ &= \frac{1}{\lambda}\exp(j\theta_o), \end{aligned} \tag{2.5}$$

where $\|\mathbf{f_r}\| = \frac{1}{\lambda}$.

In other words, a single source/receiver pair results in one vector in the spatial frequency domain, whose endpoint lies on a circle of radius $\frac{1}{\lambda}$, as depicted in Fig. 2.1(b). The direction of this vector is dictated by the angle θ_o, the angular receiver position as seen by the source.

2.1.1 Effect of Receiver Coverage on Spatial Frequency Content

Again in the case of a point source, the introduction of more than one point receiver will further our understanding of how spatial frequency content leads to the quantification of resolution, particularly cross-range resolution.

Instead of only one receiver, let us now redefine the scenario to include three receivers r_1, r_2, and r_3 with respective perspective angles θ_o, 0, and $-\theta_o$ as illustrated in Fig. 2.2(a). The three receivers together constitute *aperture coverage* in the form of a three-receiver array. Like in the original single-receiver case, the second and third receivers' frequency contribution are also vectors in the spatial frequency domain whose endpoint lies on the circle of radius $\frac{1}{\lambda}$ in accordance with their perspective angles.

The three spatial frequency vector endpoints along the $\frac{1}{\lambda}$-radius circle now span a portion of the circle's circumference, delineating an arc (Fig. 2.2(b)). Projecting the arc along the f_x and f_y directions then gives frequency bandwidths

$$\Delta f_x = \frac{1}{\lambda} - \frac{1}{\lambda}\cos\theta_o \tag{2.6a}$$

and

$$\Delta f_y = \frac{2}{\lambda}\sin\theta_o. \tag{2.6b}$$

Notice that the three receivers need not be colinear in space to result in a frequency arc which is symmetrical about the f_x axis. The operative parameter is their perspective angle. Had r_1 been located at some perspective angle θ_1, r_2 at 0, and r_3 at some different angle $-\theta_2$, an arc would still be established on the same circumference though not symmetric about the the f_x axis. From there, the same notion applies for projecting this arc onto the frequency axes to find bandwidths Δf_x and Δf_y, though not in the exact form of Eq. (2.6).

What Δf_x and Δf_y signify is the system's *resolution*, or the degree to which the position of the emitting source s can be resolved by the receivers in the spatial domain (x, y) [56]. The inverses of Δf_x and Δf_y give the resolutions in their respective directions in the spatial domain:

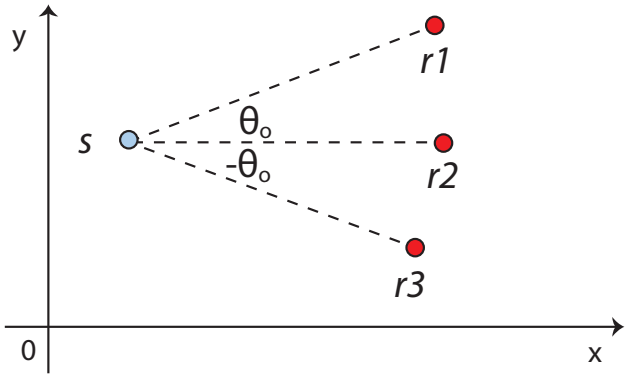

(a) Source and three receivers in space.

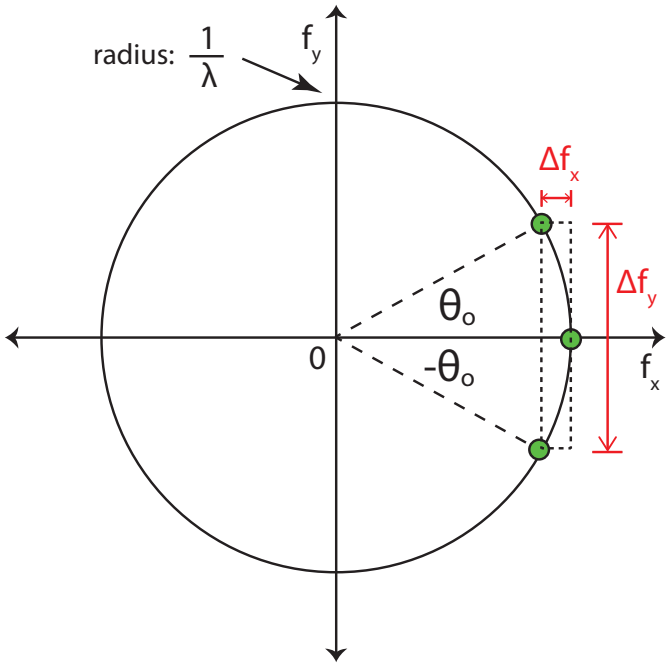

(b) Corresponding spatial frequency signature of three points.

Figure 2.2: Passive imaging scenario with receiver aperture.

$$\Delta x = \frac{1}{\Delta f_x} = \frac{\lambda}{1 - \cos\theta_o} \tag{2.7a}$$

$$\Delta y = \frac{1}{\Delta f_y} = \frac{\lambda}{2\sin\theta_o} \tag{2.7b}$$

The three-receiver array in (x, y) is generally oriented such that it spans the y-direction while imaging a source located some distance away in the x-direction. By this arrangement, the y-direction is considered to be the *cross-range* direction and the x-direction, the *range* direction. The associated resolutions in these directions are also termed accordingly: *cross-range resolution* Δy and *range resolution* Δx.

In our example, both Δf_y andΔf_x have non-zero values but Δf_y tends to dominate for most values of θ_o. In other words, the cross-range resolution improves (i.e. Δf_y increases) dramatically as θ_o increases from 0 to $\frac{\pi}{2}$. Range resolution also improves but to a lesser extent. As we will see in Chapter 3, the introduction of additional wavelengths can improve range resolution considerably.

2.2 Active Imaging

In contrast to passive imaging whereby an array aperture images a source only by receiving the source's signals, active imaging involves transmission of energy as well as reception. For example, to image a target located in the region of interest,

a transceiving element transmits a waveform into the region of interest. Energy is then reflected off a target back toward the transceiver which receives the energy. The received waveform is a function of the target distance and allows the imaging system to reconstruct the target.

Because active imaging does not rely on an emitting source but rather a reflective target, this section is concerned with imaging *targets* instead of sources. Additionally, we will refer to a single transceiving unit as an *element*, two or more of which constitute an imaging array aperture. We will describe how the spatial frequency content of an active imaging scenario differs fundamentally from that of a passive scenario. This leads also to changes in range and cross-range resolutions.

2.2.1 Monostatic Mode

Monostatic imaging refers to the mode of data acquisition in which the same element both transmits illuminating energy and receives the reflected signals. The effect of this imaging scenario on the spatial frequency content of the data can be described using a simple example.

Consider the scenario in Fig. 2.3(a) wherein a point element e located at (x_e, y_e) emits (omnidirectionally and in a homogenous medium) a wave of fixed wavelength λ and attempts to image a point target t located at (x_t, y_t) by receiving the

waveform reflected off of t. The transmission of the wave results in an illumination waveform $I(x, y)$, which at the location of t is

$$I(x_t, y_t) = \frac{1}{j\lambda r} \exp\left(j\frac{2\pi r}{\lambda}\right), \tag{2.8}$$

where $r = \sqrt{(x_e - x_t)^2 + (y_e - y_t)^2}$. The local spatial frequencies at the target location are the derivatives of this waveform, evaluated at (x_t, y_t):

$$\begin{aligned} f_{x,t} &= \left[\frac{\partial}{\partial x}\left(\frac{\sqrt{(x_e - x)^2 + (y_e - y)^2}}{\lambda}\right)\right]\Bigg|_{x=x_t, y=y_t} \\ &= -\frac{1}{\lambda}\cos\theta_o, \end{aligned} \tag{2.9}$$

and

$$\begin{aligned} f_{y,t} &= \left[\frac{\partial}{\partial y}\left(\frac{\sqrt{(x_e - x)^2 + (y_e - y)^2}}{\lambda}\right)\right]\Bigg|_{x=x_t, y=y_t} \\ &= -\frac{1}{\lambda}\sin\theta_o, \end{aligned} \tag{2.10}$$

where θ_o is the perspective angle formed between the vector from t to e and the normal axis.

The process of target illumination can be seen as a modulation of the target point by the frequencies described by Eqs. (2.9) and (2.10). This modulation step is what incorporates the illumination process into the analysis, and allows

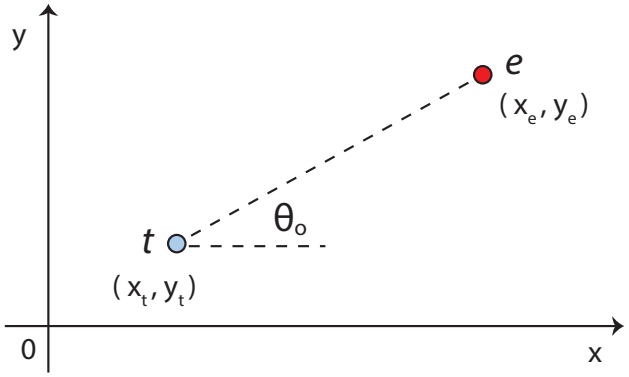

(a) Target and tranceiver element in space.

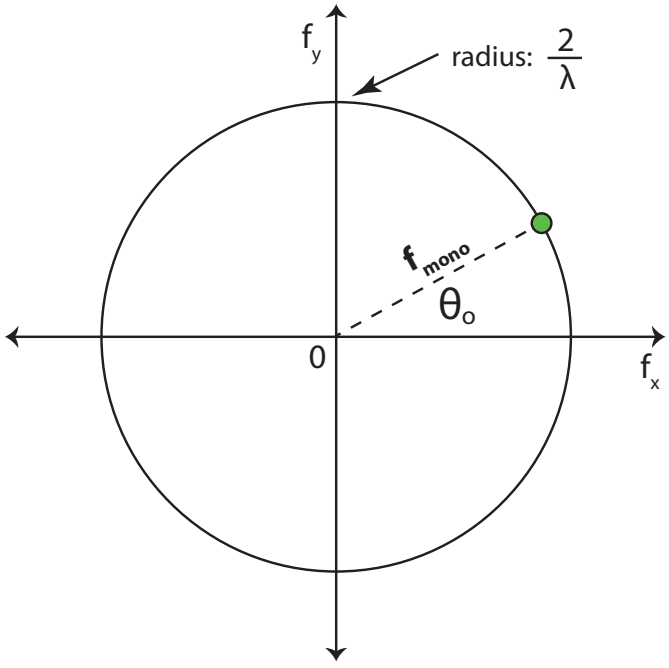

(b) Resultant spatial frequency signature obtained by summing the contributions from Fig. 2.4(a) and Fig. 2.4(b)

Figure 2.3: Monostatic imaging with a single tranceiver element.

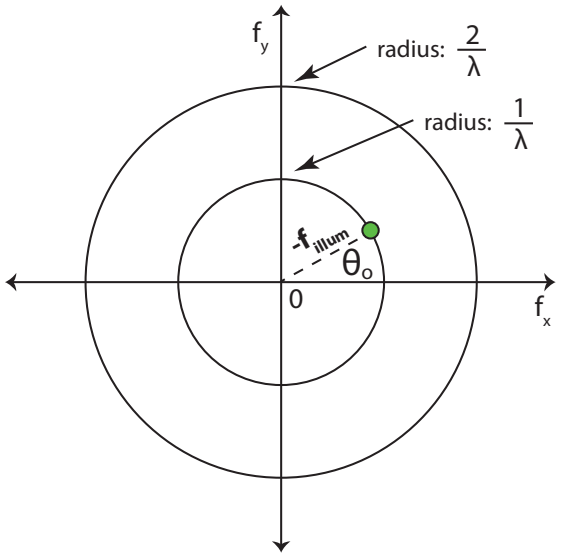

(a) Reversed signature resulting from target illumination.

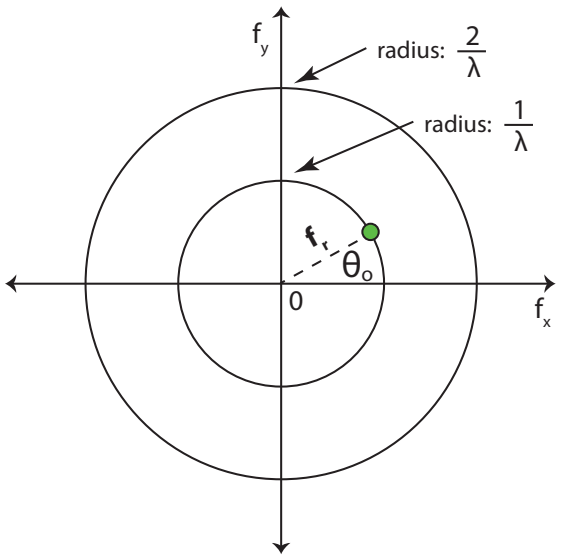

(b) Signature resulting from wave reflection.

Figure 2.4: Monostatic spatial frequency signatures from (a) wave transmission and (b) reception.

for the reflection step to be treated as a *source at the target location* emitting a signal of wavelength λ. By identifying and compensating for this modulation due to transmission, the latter receiving portion of this example can be reduced to a passive imaging model in which the target is modeled as a source.

After e's illumination of t's location, t assumes the role of a pseudo source as it emits (in the form of a reflection) a waveform with directional frequencies matching those governed by Eqs. (2.9) and (2.10). The x and y components of the resulting waveform over (x, y) can be approximated as:

$$\begin{aligned} R_x(x,y) &\approx \frac{1}{j\lambda r}\exp\left(j2\pi f_{x,t}x\right) \\ &\approx \frac{1}{j\lambda r}\exp\left(-j2\pi\frac{\cos\theta_o}{\lambda}x\right) \end{aligned} \tag{2.11}$$

and

$$\begin{aligned} R_y(x,y) &\approx \frac{1}{j\lambda r}\exp\left(j2\pi f_{y,t}y\right) \\ &\approx \frac{1}{j\lambda r}\exp\left(-j2\pi\frac{\sin\theta_o}{\lambda}y\right), \end{aligned} \tag{2.12}$$

where $r = \sqrt{(x-x_t)^2 + (y-y_t)^2}$. The original Green's function is modified such that the local spatial frequencies seen at the target position now act as emitted frequencies from the target position. Introducing this form reaffirms that the

frequency content detected at the receiving element is governed by the relative positions of the element and target.

Recall that a passive receiver and an emitting source give rise to a vector in the spatial frequency domain as seen in Eq. (2.5). Similarly, the illumination of t by e results in the vector $\mathbf{f_{illum}}$:

$$\begin{aligned} \mathbf{f_{illum}} = \begin{bmatrix} f_{x,t} \\ \\ f_{y,t} \end{bmatrix} &= -\frac{1}{\lambda} \begin{bmatrix} \cos\theta_o \\ \\ \sin\theta_o \end{bmatrix} \\ &= -\frac{1}{\lambda} \exp(j\theta_o). \end{aligned} \tag{2.13}$$

Note that this vector's endpoint lies on the circle of radius $\frac{1}{\lambda}$ in the spatial frequency domain, but is located opposite to where it would be in the passive case due to the flipped direction of wave propagation.

To obtain the net spatial frequency content as a result of the monostatic system, we must resist the temptation to simply add $\mathbf{f_{illum}}$ to the the vector associated with passive reception, $\mathbf{f_r}$ from Eq. (2.5). This is because the vector $\mathbf{f_r}$ only has relevance if the illumination vector is cancelled out. Because the illumination process introduces modulations to the (x, y) space that are not due to the target range, ensuring that the received reflected data is entirely due to the target range requires that these modulation effects be first *subtracted* away [31]. If we define

the resultant vector $\mathbf{f_{mono}}$ in the spatial frequency domain that characterizes our monostatic system example, we find that

$$\begin{aligned} \mathbf{f_{mono}} &\neq +\mathbf{f_{illum}} + \mathbf{f_r} = 0 \\ \mathbf{f_{mono}} &= -\mathbf{f_{illum}} + \mathbf{f_r} = 2\mathbf{f_r} \\ &= \frac{2}{\lambda}\exp(j\theta_o), \end{aligned} \tag{2.14}$$

which is illustrated in Fig. 2.4(a), Fig. 2.4(b), and Fig. 2.3(b). Thus, for a purely monostatic configuration, the spatial frequency vector lies on a circle of radius $\frac{2}{\lambda}$, up by a factor of 2 from the passive case.

But like the passive case, the addition of one or more monostatic transceiver elements adds to the angular span of the arc delineated by each perspective angle. To illustrate the spatial frequency bandwidths associated with monostatic imaging, consider the scenario in Fig. 2.5(a) in which a three-element array aperture (resembling the three-receiver example in the passive case, but replacing the source with a target, and the receivers with transceiver elements). Fig. 2.5(b) shows that with the same θ_o, 0, and $-\theta_o$ perspective angles, the established arc covers the same angular span, but is itself larger due to the increase in the circle's radius. Projecting the arc along the f_x and f_y directions gives the spatial frequency bandwidths for the monostatic case:

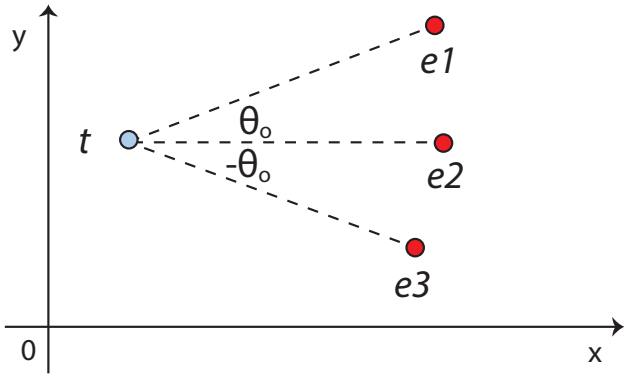

(a) Target and three elements in space.

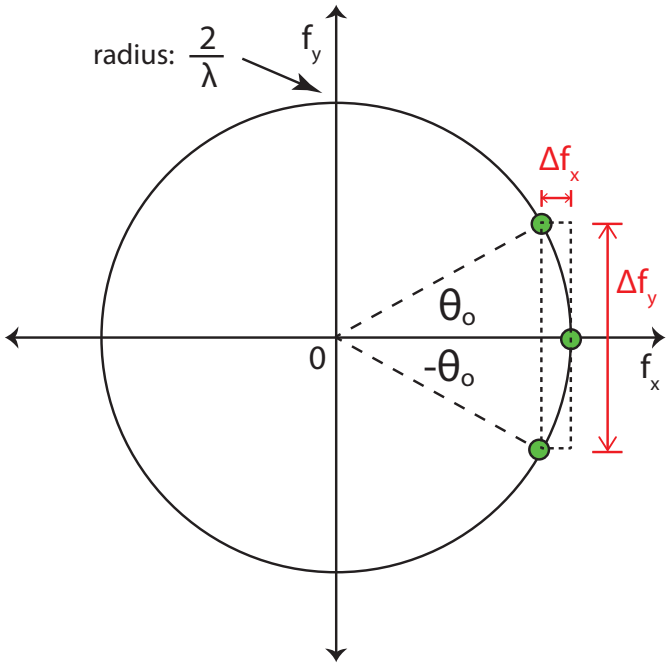

(b) Corresponding spatial frequency signature of three points.

Figure 2.5: Active monostatic imaging scenario with receiver aperture.

$$\Delta f_x = \frac{2}{\lambda} - \frac{2}{\lambda}\cos\theta_o \tag{2.15a}$$

and

$$\Delta f_y = \frac{4}{\lambda}\sin\theta_o. \tag{2.15b}$$

Their inverses give the range and cross-range resolutions:

$$\Delta x = \frac{1}{\Delta f_x} = \frac{\lambda}{2(1-\cos\theta_o)} \tag{2.16a}$$

$$\Delta y = \frac{1}{\Delta f_y} = \frac{\lambda}{4\sin\theta_o} \tag{2.16b}$$

The change from passive imaging to monostatic imaging improves resolution by a factor of 2, assuming that the geometries are held constant. This means that round-trip (monostatic) wave propagation is preferable for locating the target position to a one-way (passive) propagation for locating a source position.

2.2.2 Bistatic Mode

Bistatic imaging refers to the mode of data acquisition in which the transmitting element and the receiving element are not the same element. In an array of elements, this is often the case. As the distance between the transmitting element and the receiving element approaches zero, the data acquired bistatically converges with that acquired with monostatic operation.

Differences in spatial frequency content exist between bistatic and monostatic operation. Consider a basic scenario for bistatic imaging as show in Fig. 2.6(a): A target t is being imaged by two elements, one which transmits a wave of fixed wavelength λ (e_{illum}) and one which receives it (e_r). Let us again define perspective angles θ_o (target to e_{illum}) and $-\theta_1$ (target to e_r) where $\left|\boldsymbol{\theta_o}\right| < \left|\boldsymbol{\theta_1}\right|$.

(Although it is true that an element is capable of both transmitting and receiving wave energy as controlled by a programmed switching routine in an array system, we bring attention to one bistatic transmit/receive scenario involving the two elements e_{illum} and e_r, while bearing in mind that many transmit/receive combinations exist for an array of elements.)

Much of the same flow of concepts apply for bistatic imaging as they do for monostatic imaging, namely that the resultant spatial frequency vector is the sum of a negated illumination vector $\mathbf{f_{illum}}$ and a receive vector $\mathbf{f_r}$. Recall that the monostatic case saw the resultant $\mathbf{f_{mono}}$ vector equal two times $\mathbf{f_r}$ due to

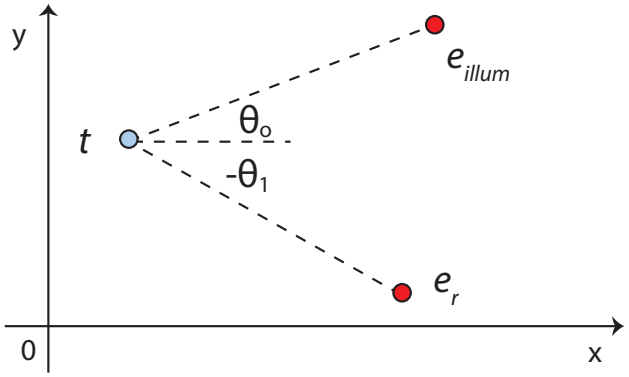

(a) Target and two elements in space.

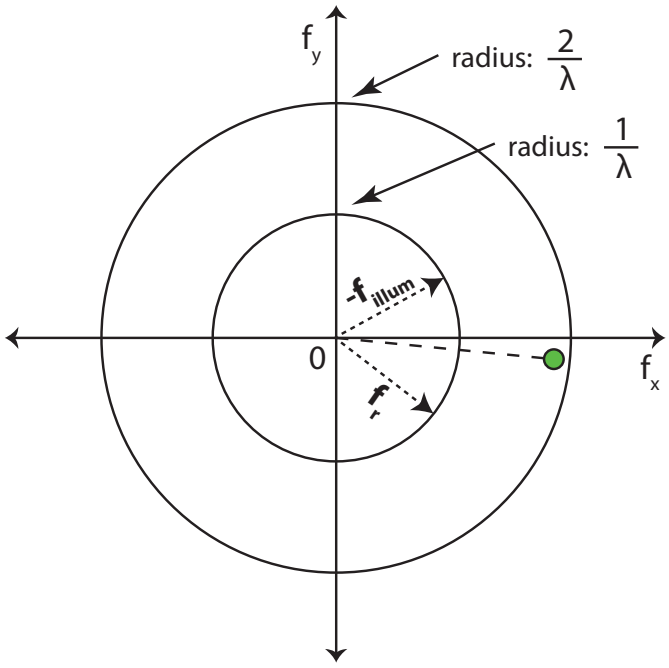

(b) Corresponding spatial frequency signature.

Figure 2.6: Active bistatic imaging scenario with a two-element receiver aperture.

the single position of both transmitter and receiver (Eq. (2.14)). The bistatic resultant vector does not share that same attribute:

$$\begin{aligned} \mathbf{f_{bi}} &= -\mathbf{f_{illum}} + \mathbf{f_r} \\ &= \frac{1}{\lambda}\exp(j\theta_o) + \frac{1}{\lambda}\exp(j(-\theta_1)). \end{aligned} \tag{2.17}$$

The two exponential terms in the sum do not simplify as readily in the bistatic case as they did in Eq. (2.14), but the sum does converge to a magnitude of $\frac{2}{\lambda}$ as the sum $\left|\theta_{\mathbf{o}}\right| + \left|\theta_{\mathbf{1}}\right|$ approaches zero (that is, approaches the monostatic case). If e_{illum} and e_r were located symmetrically about the x-axis such that θ_o = -θ_1, the $\mathbf{f_{bi}}$ would lie at an angle of zero in the spatial frequency domain. Incidentally, a monostatic element imaging a target at a perspective angle $\theta_o = 0$ would also give a resultant spatial frequency vector lying in that same direction. However, the $\mathbf{f_{mono}}$ vector would have a magnitude equal to $\frac{2}{\lambda}$ but the $\mathbf{f_{bi}}$ vector magnitude would be less $\frac{2}{\lambda}$, seen in Fig. 2.6(b).

Notice that despite having two elements participating in the bistatic example, we still end up with one resultant vector (one point) in the spatial frequency domain. Even collecting an additional dataset by reversing the two elements' roles as transmitter and receiver does not (in theory) give any added information about the target location. This is because for both cases, $\mathbf{f_{bi}}$ does not change.

Nonetheless, as we have seen with passive and monostatic operation, having more bistatic element pairs operating during data acquisition will create a span of points in the spatial frequency domain. The greater the bandwidth in the f_x and f_y directions, the better the imaging resolution for a given target location. In order to obtain a large collection of spatial frequency points, more bistatic transmit/receive pairs must be used. In the following subsection, we will discuss how this is done in an array of elements using multiple frequencies with both bistatic and monostatic data.

2.2.3 Multistatic Mode With Multiple Frequencies

By now we accept that improved resolution comes from broadening the spatial frequency band as greatly as possible in an imaging system. We will now direct our attention to how that can be achieved using multistatic mode and multiple coherent frequencies.

The imaging system in this thesis is inherently reliant on active imaging. That is, our goal is to image targets by transmitting and receiving wave energy using an array of elements. To increase the number of spatial frequency points during an data acquisition, we seek to operate in both monostatic and bistatic mode, or *multistatic* mode. Given an array with N elements, there are N monostatic tracks, and $N^2 - N$ bistatic tracks. The $N^2 - N$ bistatic tracks includes all *permutations*

of pairs of transmit/receive elements, so that every pair of elements is counted twice (once when one element transmits and other other receives, and twice when their roles are switched). For a full single-frequency multistatic cycle, a total of N^2 data tracks are acquired by the system in one complete cycle. Although a pair of elements operating bistatically will give the same spatial frequency vector signature regardless of which receives and which transmits, a practical system will still perform both for the purpose of noise reduction.

By operating multistatically with N elements with a single temporal frequency $f_1 = \frac{v}{\lambda_1}$ (where v is the speed of sound in the medium), the spatial frequency domain will see N^2 points—some directly atop another—clustered about an arc of radius $\frac{2}{\lambda_1}$. Although using all multistatic tracks in a relatively large array will widen the spatial frequency band covered, the benefit is predominantly in the f_y (cross-range) direction and not the f_x (range) direction.

Fortunately, a system that operates with *more than one* frequency will increase the span of points in the f_x direction. If the same multistatic data acquisition process is repeated using a second temporal frequency f_2, a new set of N^2 points will be introduced, clustered about an arc of radius $\frac{2f_2}{v}$, or $\frac{2}{\lambda_2}$. As this continues for a set of stepped K temporal frequencies $f_1, f_2, ..., f_K$, the spatial frequency domain will see K sets of N^2 points spanned across an area generally bounded by the radii $\frac{2}{\lambda_1}$ and $\frac{2}{\lambda_k}$. Fig. 2.7 and Fig. 2.8 give visual accounts.

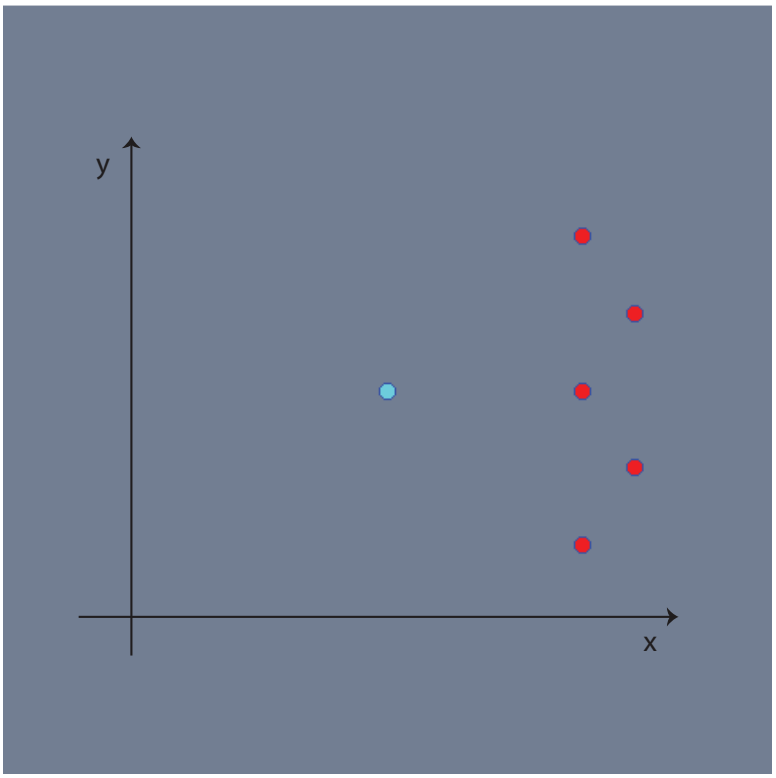

(a) Target point illuminated by five elements in space.

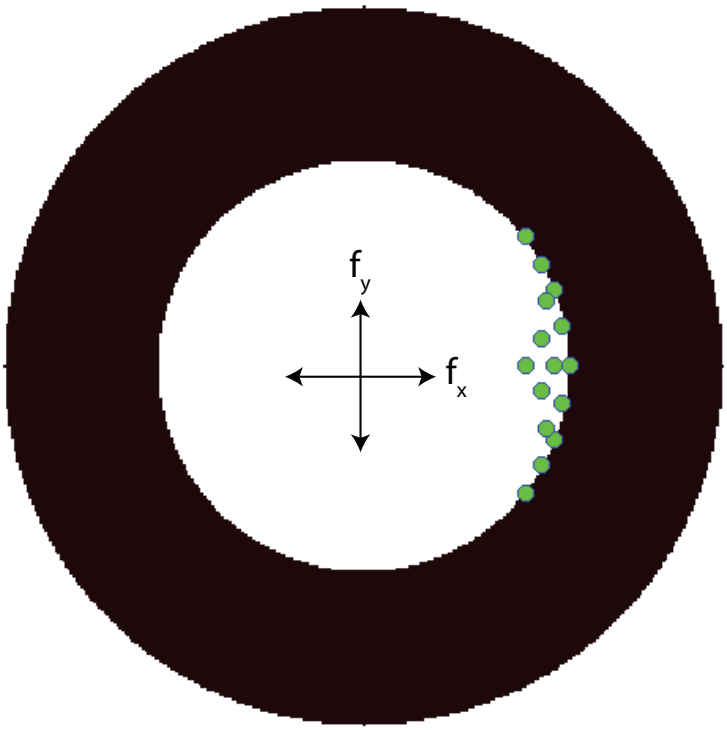

(b) Spatial frequency signature for a single-frequency, $f_1 = \frac{v}{\lambda_1}$, with dots clustered around the radius $\frac{2}{\lambda_1}$.

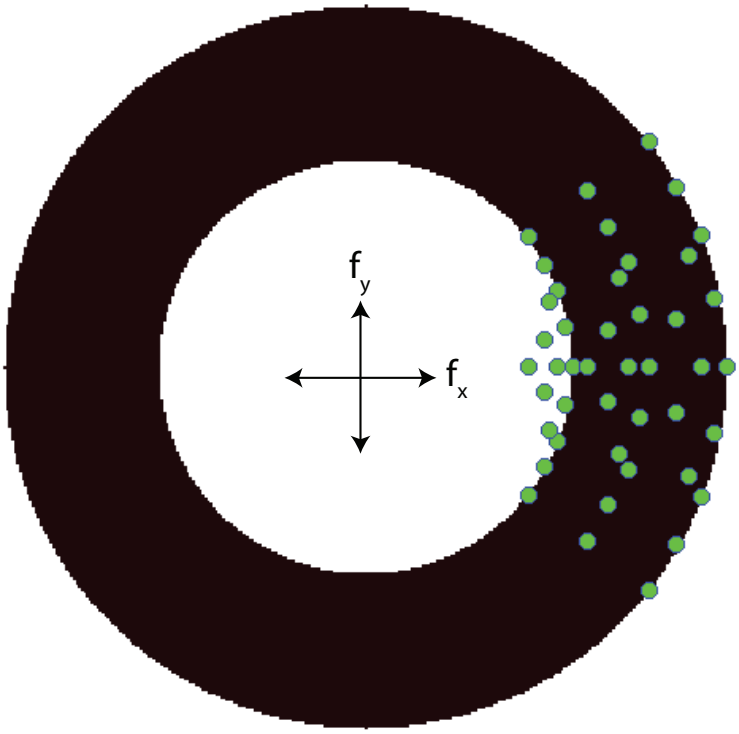

(c) Spatial frequency signature for three evenly-spaced temporal frequencies ranging from $f_1 = \frac{v}{\lambda_1}$ to $f_2 = \frac{v}{\lambda_2}$, with dots clustered between the radii $\frac{2}{\lambda_1}$ and $\frac{2}{\lambda_2}$.

Figure 2.7: Multistatic mode. Spatial frequency plots are shown with a darkened band of inner radius $\frac{2}{\lambda_1}$ and outer radius $\frac{2}{\lambda_2}$. Note that bistatic points fall short of their respective frequency radius.

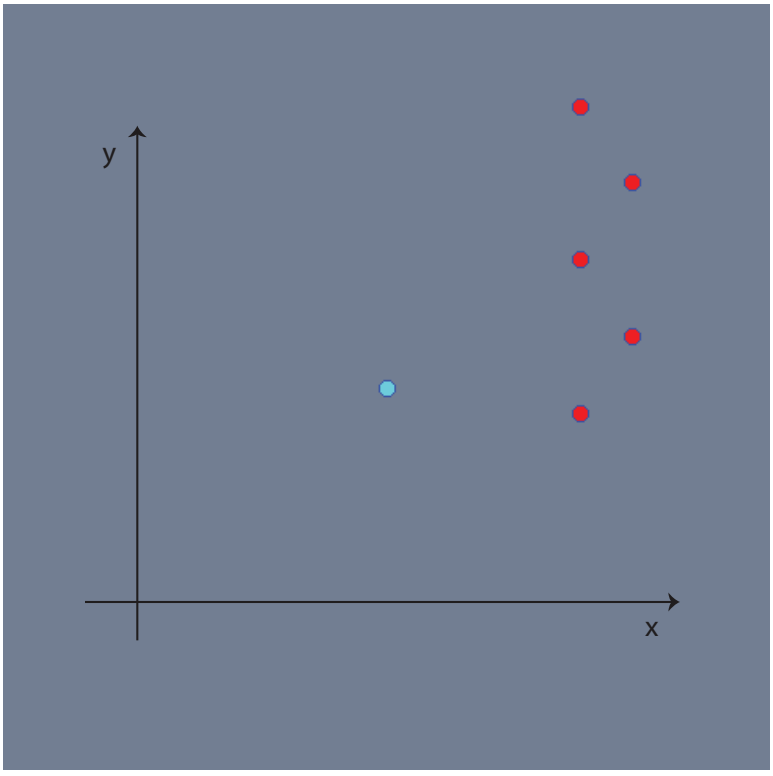

(a) Off-center target point illuminated by five elements in space.

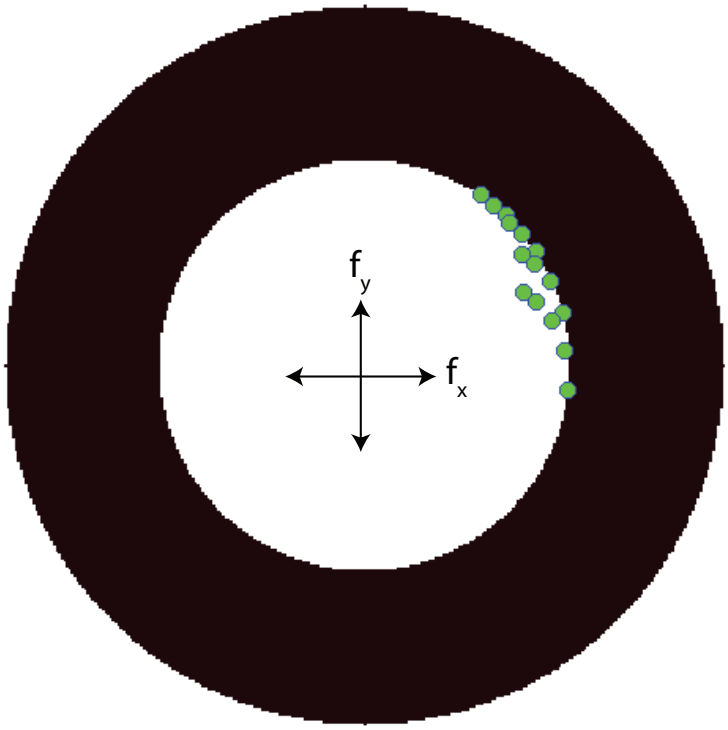

(b) Spatial frequency signature for a single temporal frequency, $f_1 = \frac{v}{\lambda_1}$, with dots clustered around the radius $\frac{2}{\lambda_1}$.

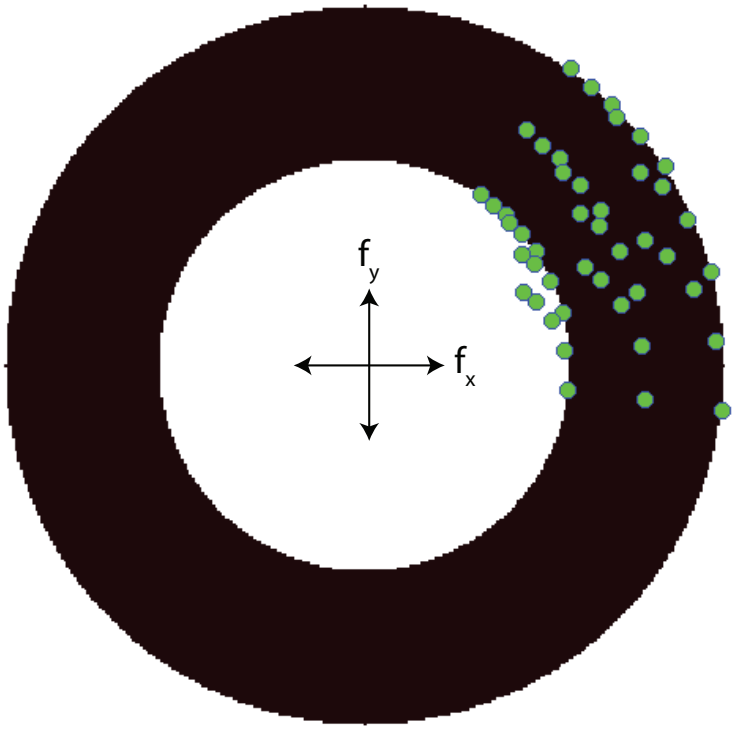

(c) Spatial frequency signature for three evenly-spaced temporal frequencies ranging from $f_1 = \frac{v}{\lambda_1}$ to $f_2 = \frac{v}{\lambda_2}$ with dots clustered between the radii $\frac{2}{\lambda_1}$ and $\frac{2}{\lambda_2}$.

Figure 2.8: Multistatic mode with off-center target. Note that the shifting of the spatial frequency signatures are commensurate to the angular change from Fig. 2.7. Spatial frequency plots are shown with a darkened band of inner radius $\frac{2}{\lambda_1}$ and outer radius $\frac{2}{\lambda_2}$.

To obtain a sense of how the range-direction spatial frequency bandwidth increases with the addition of multiple temporal frequencies, let us refer to Fig. 2.5(a). Instead of a single frequency monstatic case, we now allow for the use a series of temporal frequencies lying within a band B:

$$B = \Delta f_{temp} = f_2 - f_1, \tag{2.18}$$

from which we can define $\lambda_{max} = \frac{v}{f_1}$ and $\lambda_{min} = \frac{v}{f_2}$ where v is the speed of sound in the medium.

Along the f_x direction, all multistatic spatial frequency points are generally bounded between two arcs of radii $\frac{2}{\lambda_{min}}$ and $\frac{2}{\lambda_{max}}$. The span of the coverage in the f_x direction, Δf_x is:

$$\begin{aligned}
\Delta f_x &= f_{x,max} - f_{x,min} \\
&= \frac{2}{\lambda_{min}} - \frac{2}{\lambda_{max}} \cos\theta_o \\
&= \frac{2}{\lambda_{min}} - \frac{2}{\lambda_{max}} + \frac{2}{\lambda_{max}}(1 - \cos\theta_o) \\
&= \frac{2}{v}(f_2 - f_1) + \frac{2}{v} f_1 (1 - \cos\theta_o) \\
&= \frac{2}{v}(B + f_1(1 - \cos\theta_o)).
\end{aligned} \tag{2.19}$$

From this, we can establish the Δx, the range resolution in space:

$$\begin{aligned} \Delta x &= \frac{1}{\Delta f_x} \\ &= \frac{v}{2(B + f_1(1 - \cos\theta_o))}. \end{aligned} \tag{2.20}$$

Note that for small values of θ_o, $\Delta x \approx \frac{v}{2B}$, consistent with SAR theory for range resolution [43].

This forms the basis of *stepped-frequency continuous wave* operating in multistatic mode. The use of many temporal continuous waves drives the increase in range resolution, while multistatic data acquisition maximizes angular aperture coverage, and therefore cross-range resolution.

2.3 Approximation of Total Imaging System Resolution

For an array of N elements imaging a single point target by multistatic operation stepping through K frequencies, the spatial frequency signature of KN^2 points will be scattered across a portion of the (f_x, f_y) domain. Similar analyses in SAR imaging [63] have shown the same relationship using continuous spatial frequency coverage instead of discrete points.

Two remarks are worth emphasizing:

(1) The points spanning (f_x, f_y) are based on *a single* target location for *one* particular distribution of elements. For this reason, a resolution analysis conducted with one set of multistatic spatial frequency points cannot necessarily give a generalized estimate for the system as a whole.

(2) The collection of N^2 multistatic points per frequency assumes that all multistatic element pairs are able to illuminate and receive energy from the target point. In other words, all elements are assumed to have omnidirectional beampattern in the (x, y) plane. In reality, elements have characteristic radiation patterns that constrain the amount of energy able to be transmitted and received from angles off from the normal face of the element. See Chapter 3 for more. This means that in many cases, only a subset of the KN^2 points will emerge, due to only a subset of the multistatic pairs "seeing" the target location.

If the area spanned by the points in the spatial frequency domain extends over a distance α along the f_x direction and β along the f_y direction, the associated point target location in (x, y) would be resolvable to $\Delta x = \frac{1}{\alpha}$ and $\Delta y = \frac{1}{\beta}$. A rectangular area would be preferable for quantifying span in (f_x, f_y); but because this area generally does not assume any particular shape [55], some approximation is required.

For simplicity it may be advantageous to characterize α and β as the dimensions of the smallest rectangle that fully encloses the area. (This has already been seen in prior subsections for determining the span of an arc.) Indeed, for a target location far away from the array aperture, the area becomes more rectangular in shape. Using this convention for approximating α and β implies that overestimation of system performance is preferred over underestimation, which is sensible if we seek a best-case resolution estimate.

A crucial question in this discussion is how the imaging performance differs when the same area and span parameters α and β are achieved in two operational Cases A and B, but with B having fewer spatial frequency points. Visually, Case B may have a sparser distribution of points across the same region possibly due to a number of non-operating multistatic element pairs. Because both cases have identical α and β values, the resolutions in both cases are therefore equal for a given target location. But what Case B suffers in comparison to Case A is ambiguity in target reconstruction. The low spatial frequency sampling in Case B results in repetition artifacts across the reconstructed region of interest. The greater the distances between multistatic points in (f_x, f_y), the closer together target artifacts will be in (x, y). By minimizing these distances through the acquisition of many spatial frequency points, the length between repetitions may be well out of the specified range of the region of interest.

An exhaustive estimation of total imaging system resolution for a multistatic stepped-FMCW system would require every possible array configuration to undergo a pixelwise computation of range and cross-range resolution within the region of interest. A practical attempt would involve only a limited number of configurations of interest with a limited number of specified target location regions.

2.4 Conclusion

In this chapter, we have established the technical foundation for imaging resolution for a stepped-frequency modulated continuous wave (FMCW) multistatic system. A passive imaging case was first analyzed in order to provide a basis for describing monostatic and bistatic imaging modes, which together give rise to multistatic imaging.

By examining the spatial frequency content in coherent imaging cases, we describe how monostatic and bistatic imaging provide a factor of 2 improvement in cross-range resolution over passive imaging, especially when bistatic perspective angles are small.

The result of this analysis also shows that for a given target location and array aperture, a larger span of spatial frequency signature points translates to better

imaging resolution. Achieving this large span is accomplished by (1) using a large number of frequencies—the basis for stepped-FMCW—which primarily improves range resolution, and (2) by using a large array aperture that surrounds a target maximally, which primarily improves cross-range resolution.

Chapter 3

The Stepped-FMCW Modality

This chapter focuses on the fundamental task of multistatic stepped-FMCW imaging system to obtain range data within the region of interest. Range data provides estimates of distances (between the transducer array elements and the reflective targets) which are processed to reconstruct an image of the targets. The manner in which the stepped-FMCW probing signals are emitted is described, as well as its logical basis as a ranging technique along with experiments.

References [38], [45], and [44] form the basis for this chapter.

3.1 Background: Pulse Echo Range Estimation

The most straightforward method of acquiring range data is the *pulse echo* technique which remains the foundation of ultrasound imaging. This refers to the transmission of a short-duration pulse into the region of interest at $t = 0$. Upon receiving back the reflected pulse(s) as a function of time, the depth of the

reflective interface(s) can be found [7]. For a reflector at a distance d_o away from the transducer, and a speed of sound in the medium of v, its echoed pulse in the pulse echo data should appear at τ_o, where

$$\tau_o = \frac{2d_o}{v}. \tag{3.1}$$

The factor of 2 accounts for the round-trip distance of the pulse. The result of a pulse echo experiment can be displayed visually as an *A-mode* (or amplitude-mode) scan, which is a one-dimensional plot of the received reflected energy pulses as a function of distance; the greater the amplitude, the greater the detected presence of a reflector at that distance from the transducer. Arriving at the A-mode image from the pulse echo data requires a simple scaling of the horizontal axis in accordance with Eq. (3.1).

Because a medical ultrasound system cannot tailor each reconstruction with a priori knowledge of the speed of sound in all relevant tissues in the region, typically medical ultrasounds systems reconstruct images by assuming $v \approx 1540\,\mathrm{m\,s^{-1}}$ which is about halfway between the speeds in muscle and water.

When A-mode scans are collected across a confined region of interest, a two-dimensional image can be formed by overlaying processed A-mode scans and displaying the amplitudes as brightness on a screen. This is called a *B-mode* scan (or

brightness-mode scan), and is the foundation for conventional ultrasound imaging. The more closely-spaced the A-scans, the more the corresponding B-scan will appear to represent an appreciable cross-sectional image beneath the transducer. Prior to B-mode image formation, a series of conditioning steps are often applied to the A-mode data including:

1. *Demodulation*, which extracts the envelope of the A-mode peaks and rejects the carrier frequency;

2. *Time-gain control*, which boosts the signal peaks from more distant reflectors which have been more attenuated than peaks from close reflectors;

3. *Compression*, which modifies the dynamic range of the echoes for display; and

4. *Thresholding*, which zeros out amplitudes below a certain value typically to eliminate noise or extranenous signals.

Although phased-array ultrasound systems can direct wave energy at discrete points or at a particular angle from the transducer, the principle of forming a brightness-mode image by sweeping an area for time-delayed reflections still applies. Hence, phased-array imaging is a subcategory of B-mode imaging. Other modes exist in modern ultrasound such as C-mode, M-mode and Doppler mode, but will not be discussed due to the scope of this thesis.

In this thesis, we will use the term *time-delay profile* to represent the received data of a single pulse echo scan. That is, a one-dimensional amplitude plot as a function of time showing the received signal at a transducer (or transducing element) with $t = 0$ representing the time of pulse transmission. We will use the term *range profile* to represent an A-scan, that is, a plot of the information as a function of distance.

An idealized pulse echo system would transmit and receive such narrow pulses that they can be approximated as delta functions. The time-delay profile can then be generalized as a function

$$p_{\text{tdp}}(t) = \sum_{i=1}^{Z} a_i \, \delta(t - \tau_i), \tag{3.2}$$

for Z targets in the region of interest with respective reflections received at $t = \tau_i$ and with amplitude a_i. The associated target distances would be $d_i = \frac{1}{2} v \tau_i$.

3.2 Stepped-FMCW Range Estimation

A-mode and B-mode ultrasound imaging rely on estimating range with the general pulse echo modality. They can be colloquially termed as "time domain schemes" because the time delay of the reflected pulse echoes directly represents the information used for image reconstruction. On the other hand, stepped-

FMCW differs from this convention by extracting phase information from transmitted and received coherent waves. For this reason, stepped-FMCW can be viewed as a "frequency domain scheme." Notwithstanding, its application to ultrasound implies that range information must still be obtained. This section describes in phasor notation how this is accomplished.

By the end of one data acquisition cycle of the stepped-FMCW ultrasound system, each element in the multistatic array will send out a complete set of K coherent signals, stepping through a defined frequency band with frequency increment Δf:

$$f_k = f_0 + k\Delta f \tag{3.3}$$

where f_k is the frequency of the transmitted signal, f_o the starting frequency, and $k = 0, 1, 2, ..., K-1$. Optimal element operation dictates the frequency band used, which is assumed to be uniform across all elements. This is reasonable, given that array elements are typically fabricated together.

Each element in the array sequentially sends K coherent wave signals, upon which all elements switch to receive mode. Thus, each of the N^2 multistatic pair of elements sees K coherent signals between them (as discussed in Subsection 2.2.3) and therefore KN^2 spatial frequency points in total. In this thesis, the optimal

order in which these multistatic pairs and coherent signals are sent and received is not investigated. It is assumed that once a data acquisition cycle is complete, all have been stored in memory. Further, the following analysis will deal with one multistatic pair, from which the reader can extrapolate to understand full multistatic operation.

During a frequency step, the transmitting elements function as a continuous wave (CW) system. This allows the stepped-FMCW modality to be regarded as an transmitting and receiving an organized sequence of CW transmissions, which is in contrast to a short-duration pulse. The transmitted signal with frequency f_k can be written in the form:

$$e_{\text{trans},k}(t) = E \exp\left(j2\pi f_k t\right), \tag{3.4}$$

where E is an arbitrary amplitude. As the transmitted CW reaches and reflects back from a target, the signal detected by the receiving element is a modified form of the transmitted wave. Due to attenuation in the medium and target reflectivity, an amplitude factor A (with value between 0 and 1) is introduced. But more importantly, a phase shift τ_o is present as a result of the round-trip travel time seen in Eq. (3.1).

Unlike a monostatic track where a single Euclidean distance d_o gives the target range, target ranging with a bistatic element pair involves two distinct distances, d_1 and d_2, with which the time-delay can be expressed:

$$\tau_o = \frac{d_1 + d_2}{v}, \tag{3.5}$$

where d_1 is the distance from the transmitting element to the target, and d_2 is the distance between the target and the receiving element.

However, for simplicity, the analysis will continue with the original time-delay equation from Eq. (3.1) suggestive of a monostatic setup. The received reflected signal is then

$$\begin{aligned} e_{\mathrm{rec},k}(t) &= AE \exp\left(j2\pi f_k(t - \tau_o)\right) \\ &= AE \exp\left(j2\pi f_k \left(t - \frac{2d_o}{v}\right)\right). \end{aligned} \tag{3.6}$$

The k^{th} received signal, $e_{\text{rec},k}(t)$, $k = 0, ..., K-1$, is then demodulated by multiplying to the complex conjugate of the transmitted signal:

$$\begin{aligned} e_{\text{demod},k}(t) &= e_{\text{rec},k}(t)\, e^{*}_{\text{trans},k}(t) \\ &= AE^2 \exp(-j2\pi f_k \tau_o) \\ &= AE^2 \exp\left(-j2\pi f_o \frac{2d_o}{v}\right) \exp\left(-j2\pi k \Delta f \frac{2d_o}{v}\right). \end{aligned} \tag{3.7}$$

For a single multistatic element pair, the result is a series of K complex scalars e_{demod}. These scalars together can be considered a discrete function e_{demod} in terms of frequency index k.

$$\begin{aligned} e_{\text{demod}}[k] &= AE^2 \exp\left(-j2\pi f_o \frac{2d_o}{v}\right) \exp\left(-j2\pi k \Delta f \frac{2d_o}{v}\right) \\ &= C \exp\left(-j2\pi k \Delta f \frac{2d_o}{v}\right), \end{aligned} \tag{3.8}$$

where $C = AE^2 \exp\left(-j2\pi f_o \frac{2d_o}{v}\right)$, which has no k dependence.

The significance of the k-dependent factor of Eq. (3.8) lies in its connection to the canonical discrete Fourier transform (DFT) kernel: $\exp\left(-j2\pi \frac{nk}{N}\right)$. Recall that k is the discrete frequency domain variable, n is the discrete time domain variable, and N is the length of the time domain sequence [47]. If the DFT kernel

is juxtaposed with the k-dependent exponential factor of $e_{\text{demod}}[k]$, the exponential terms can be matched for correspondence, specifically if:

$$\begin{aligned} \frac{n}{N} &= \Delta f \, \frac{2d_o}{v} \\ n &= 2(N\Delta f)\frac{d_o}{v}. \end{aligned} \tag{3.9}$$

Because the DFT implies that the discrete sequences in the time and frequency domains are equal in length, we can establish that the number of frequencies used in the stepped-FMCW system, K, is equal to N in the DFT kernel. Hence, if our system bandwidth is $B = K\Delta f$, in accordance with Eq. (2.18), then Eq. (3.9) can be rewritten as

$$n = B \, \frac{2d_o}{v}. \tag{3.10}$$

This reveals a linear relationship between the time-domain index n and the target range, d_o. From this, the DFT can be used to relate a stepped-FMCW (frequency) data set acquired by a multistatic element pair to a corresponding range profile:

$$\begin{aligned} e_{\text{demod}}[k] &= C \exp\left(-j2\pi k \Delta f \frac{2d_o}{v}\right) \\ &= \text{DFT}\Big\{C\,\delta\left(n - \frac{2B}{v}\,d_o\right)\Big\}. \end{aligned} \tag{3.11}$$

This means that a time-domain sequence indexed by n will see a delta at $n = \frac{2B}{v} d_o = B\tau_o$, in accordance with Eq. (3.10). If we reorganize the range distance in terms of the positive index integer n,

$$d_o = \left(\frac{v}{2B}\right) n, \tag{3.12}$$

it becomes clear that the factor $\frac{v}{2B}$ represents the minimum range increment in the range estimation, or *range resolution*:

$$\Delta x = \frac{v}{2B}. \tag{3.13}$$

The result of the range resolution analysis from Eq. (3.13) is in agreement with Eq. (2.20).

Therefore, it is shown that the frequency-based stepped-FMCW data carries within it the target range information. The range information can be found by taking the inverse DFT (IDFT) of the demodulated received CW data.

3.2.1 Equivalence of Stepped-FMCW and Pulse Echo

Processing stepped-FMCW data gives a sampled version of the continuous-time time-delay profile

Proposing stepped-FMCW as a means to estimate target distances requires that its mathematical formulation lead not only to a single target distance, but to a generalized time-delay profile seen in Eq. (3.2). The following describes this migration.

Broadly speaking, the pulse echo time-delay profile is the impulse response of system (target distribution). Instead of a transmitted pulse at $t = 0$ as the input waveform, the stepped-FMCW modality involves transmitting a series of CWs described in Eq. (3.4). Given this relationship, the received signal $e_{\mathrm{rec},k}(t)$ can

alternatively be written as a convolution of $e_{\text{trans},k}(t)$ and the time-delay profile $p_{\text{tdp}}(t)$:

$$\begin{aligned} e_{\text{rec},k}(t) &= e_{\text{trans},k}(t) * p_{\text{tdp}}(t) \\ &= E \exp\left(j2\pi f_k t\right) * \sum_{i=1}^{Z} a_i \, \delta(t - \tau_i) \\ &= \sum_{i=1}^{Z} a_i \, E \exp(j2\pi f_k (t - \tau_i)). \end{aligned} \tag{3.14}$$

After demodulation, K complex scalars result, one from each of the CWs used:

$$\begin{aligned} e_{\text{demod},k}(t) &= e_{\text{rec},k}(t) \, e^*_{\text{trans},k}(t) \\ &= \sum_{i=1}^{Z} a_i \, E^2 \exp(-j2\pi f_o \tau_i) \exp(-j2\pi k \Delta f \tau_i) \\ &= E^2 \sum_{i=1}^{Z} a_i \, b_i \, \exp(-j2\pi k \Delta f \tau_i), \end{aligned} \tag{3.15}$$

where $b_i = \exp(-j2\pi f_o \tau_i)$. Arranging these scalars in a frequency-domain sequence forms $e_{\text{demod}}[k]$, whose IDFT is in the form of a discrete-time time-delay profile $\hat{p}_{\text{tdp}}[n]$ showing Z reflection peaks:

$$\begin{aligned} \hat{p}_{\text{tdp}}[n] &= \text{IDFT}\Big\{ e_{\text{demod}}[k] \Big\} \\ &= E^2 \sum_{i=1}^{Z} a_i \, b_i \, \delta(n - n_i), \end{aligned} \tag{3.16}$$

where $n_i = B\tau_i$. The sequence $\hat{p}_{\text{tdp}}[n]$ can be regarded as a sampled, scaled (by a factor B), and amplified (by a factor $b_i \, E^2$) version of $p_{\text{tdp}}(t)$.

From this result, it is revealed that the stepped-FMCW data sequence $e_{\text{demod}}[k]$ gives a time-delay profile (albeit sampled) that is equivalent to one collected by the pulse echo modality. Based on these analyses, the process of arriving at a time-delay profile in the stepped-FMCW modality can be codified in four general steps:

1. Demodulate the received CW waveforms $e_{\text{rec},k}(t)$ to obtain the sequence $e_{\text{demod}}[k]$.

2. Apply the IDFT to $e_{\text{demod}}[k]$ to arrive at $\hat{p}_{\text{tdp}}[n]$.

3. Normalize $\hat{p}_{\text{tdp}}[n]$ by multiplying it by $\gamma[n] = \frac{1}{E^2} \exp\left(j2\pi \frac{f_o}{B} n\right)$.

4. Scale the resulting sequence by defining the unit increment in n as $\frac{1}{B}$ in order to give

$$p_{\text{tdp}}[n] = \sum_{i=1}^{Z} a_i \, \delta(n - n_i),$$

where $n_i = \tau_i$.

The function $\gamma[n]$ serves to eliminate E^2 and b_i in Eq. (3.16). The product of b_i and the exponential function in $\gamma[n]$ results in unity only when $n = n_i$. For the purposes of avoiding confusion with the meaning of "range" when dealing with bistatic and monostatic tracks, we forgo the additional step required to find the range profile from the time-delay profile while bearing in mind that Eqs. (3.5) and (3.1) apply.

In practice, the DFT and IDFT are implemented with the fast Fourier transform (FFT) and inverse fast Fourier transform (IFFT). Therefore there is no guarantee that the length of $e_{\text{demod}}[k]$ and $p_{\text{tdp}}[n]$ will equal the number of CWs used, K, and will typically exceed it. Incidentally, the multiplicative effect of the exponential function $\exp\left(j2\pi\frac{f_o}{B}n\right)$ in $\gamma[n]$ can be achieved instead by zero-padding in the frequency domain prior to the IFFT operation, representing a frequency shift. Let us define $\hat{e}_{\text{demod}}[k]$ as a sequence of length L where L is a power of 2 as per the FFT algorithm such that $\hat{e}_{\text{demod}}[k]$ consists of zeros in the interval $[1, k_o]$, the original K-length sequence $e_{\text{demod}}[k]$ in the interval $[(k_o + 1), (k_o + 1 + K)]$,

and zeros in the interval $[(k_o + 2 + K), (L)]$. Padding $\hat{e}_{\text{demod}}[k]$ with k_o zeros at the start can be done provided that an integer value for k_o can be identified such that

$$\frac{k_o}{K} = \frac{f_o}{B} \tag{3.17}$$

which leads to

$$k_o = \frac{f_o}{\Delta f}. \tag{3.18}$$

Stepped-FMCW data is a sampled version of the continuous time-delay profile spectrum

Suppose that instead of using Eq. (3.2) to define the continuous time-delay profile as consisting only of impulses, a more general continuous time-delay profile, $p_{\text{tdp,gen}}(t)$, can be defined, with nondescript peaks and amplitudes. Its Fourier transform spectrum is in the form

$$P_{\text{tdp,gen}}(f) = \int p_{\text{tdp,gen}}(t) \exp(-j2\pi ft)\, \mathrm{d}t. \tag{3.19}$$

The received signal then takes the form of

$$\begin{aligned} e_{\mathrm{rec},k}(t) &= p_{\mathrm{tdp,gen}}(t) * e_{\mathrm{trans},k}(t) \\ &= p_{\mathrm{tdp,gen}}(t) * E\exp(j2\pi f_k t) \\ &= E\int p_{\mathrm{tdp,gen}}(\sigma)\exp\left(j2\pi f_k(t-\sigma)\right)\,\mathrm{d}\sigma \\ &= E\exp(j2\pi f_k t)\int p_{\mathrm{tdp,gen}}(\sigma)\exp(-j2\pi f_k\sigma)\,\mathrm{d}\sigma. \end{aligned} \tag{3.20}$$

which again is the convolution of the continuous time-delay profile and the transmitted signal. After removal of the carrier frequency f_o within f_k, Eq. (3.20) becomes

$$\begin{aligned} e_{\mathrm{demod}}[k] &= e_{\mathrm{rec},k}(t)\, e^*_{\mathrm{trans},k}(t) \\ &= E^2\int p_{\mathrm{tdp,gen}}(\sigma)\exp(-j2\pi f_k\sigma)\,\mathrm{d}\sigma \\ &= E^2\, P_{\mathrm{tdp,gen}}(f_k). \end{aligned} \tag{3.21}$$

The result of Eq. (3.21) shows that the sequence of complex scalars $e_{\mathrm{demod}}[k]$ is an amplified collection of samples of the time-delay profile spectrum $P_{\mathrm{tdp,gen}}(f)$, evaluated at each f_k of the K CWs used in the stepped-FMCW data acquisition process.

Waveform Synthesis Simulation Experiments, Pt. I: Pulse Echo Data Acquisition

At this point we have established that the stepped-FMCW ranging modality is mathematically equivalent to conventional pulse echo. More specifically, the stepped-FMCW data sequence for a multistatic element pair are the sampled values of the spectrum for the corresponding continuous pulse echo time-delay profile. As a result of this relationship, conversion between pulse echo data and stepped-FMCW data is valid. Prior stepped-FMCW simulation work could then be merged with pulse echo data to achieve a synthesis between laboratory data and a structured theoretical framework. We describe how an experimentally-acquired ultrasound pulse echo waveform was extracted and then incorporated into a stepped-FMCW imaging simulation. By using a true pulse echo waveform we are able to add the effects of the physical wave propagation in our simulations.

The data synthesis process first required the collection of a characteristic pulse. A 16-element (2×8) conformal ultrasound transducer prototype, shown in Fig. 3.1 was fabricated with lead zirconate titanate (PZT) piezoelectric elements, each bonded to an individual glass substrate. Glass substrates were attached to a copper-cladded flexible printed circuit. A tungsten-loaded epoxy backing layer for mechanical damping was applied to each element, and acoustic matching to soft tissue was optimized by coating the transducer face with a flexible parylene match-

ing layer. Each element of the the array was a square of side length 1.275 mm, with a pitch (element spacing) of 3.2 mm. A custom pulse echo transceiver was designed to transmit pulsed CW waveforms and process received data with a superheterodyne downconverter.

Figure 3.1: A 16-element conformal ultrasound array prototype of which one 1×8 row was tested.

A soft-tissue phantom, seen in Fig. 3.2 was constructed to evaluate the transducer array's ability to image internal objects of varying shapes. The phantom's tissue-mimicking material was formed from a mixture of aragose, evaporated milk, thimerosal, and glass beads. To provide two distinct scattering surfaces, a stainless steel rod (2 mm diameter) and a glass slide (1 mm thickness) served as targets. The face of the slide was fixed perpendicular to the acoustic beam, and the long axis of the rod was oriented in the same plane as the slide.

The transducer array was placed atop the phantom and coupled with it using $\sim$1 mm thick of acoustic scanning gel. Monostatic pulse echo experiments were performed using a 1×8 portion of the array at a 50 MHz sampling frequency, which provided reflections from the metal rod. A time-delay profile generated from the

(a)

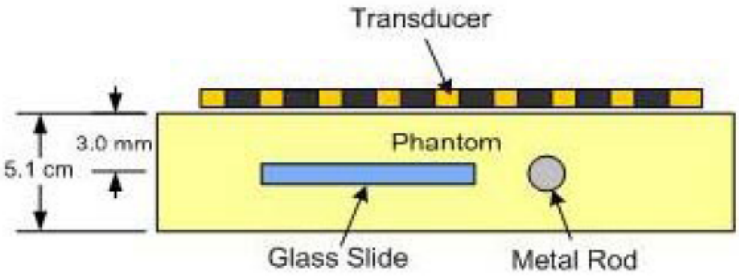

(b)

Figure 3.2: (a) Soft-tissue phantom and (b) Cross-sectional view of phantom with conformal transducer across the top surface.

rod's reflection, shown in Fig. 3.3, was collected, and I and Q channel data points corresponding to the direct path reflection were extracted for synthesis with the stepped-FMCW imaging simulations. The dimensions of the rod suggested that the pulse is well suited to represent a point target for the imaging setup, and characterizes the physical attributes of the imaging environment.

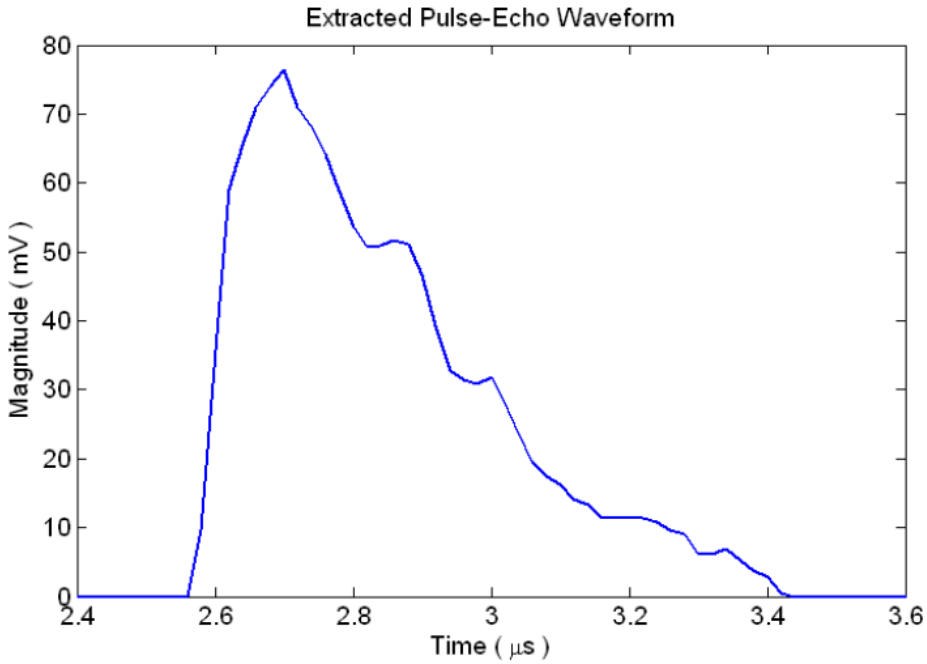

Figure 3.3: Complex-magnitude plot of received pulse echo waveform used for stepped-FMCW simulations.

Waveform Synthesis Simulation Experiments, Pt. II:

Initial Stepped-FMCW Imaging Simulations

Preliminary stepped-FMCW imaging simulations consisted of five idealized point targets surrounded by an array of eight equally-spaced point elements, as illustrated in Fig. 3.4, representing a conformal array imaging inward. Prior to waveform synthesis, the simulations operated in basic form under unitless terms, serving to validate initial imaging formation procedures, and visualize relationships between input parameters (including bandwidth) and resolving capabilty.

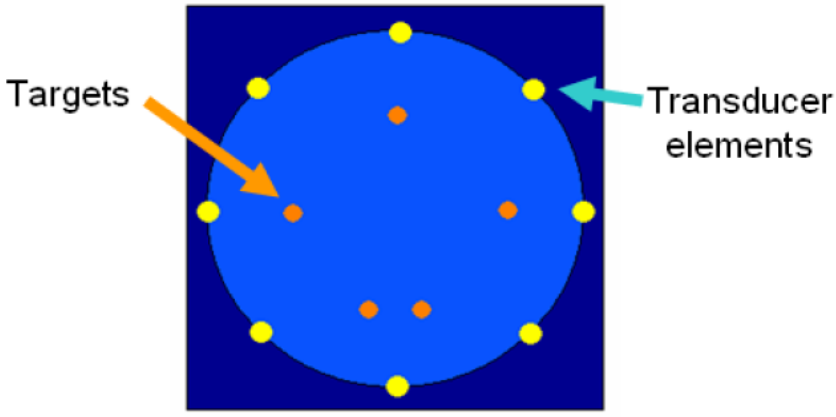

Figure 3.4: Target and transducer element arrangement for prior stepped-FMCW simulations.

For each pair of elements, one acting as a receiver and the other as the transmitter, a theoretical discrete time-delay profile corresponding to the target distribution was determined using unit impulses as target responses. As expected, the number of impulses in each profile equaled the number of targets. Because dimensions and system specifications were not explicitly set, time-delay profiles lacked true adherence to those from a real system. To simulate a finite stepped-FMCW bandwidth, FFTs were performed on the theoretical time-delay profiles in order to remove portions of spectral content. The remaining bandwidth was referenced by the percentage of the total bandwidth (up to sampling frequency). Fig. 3.5 shows reconstructed images from these multistatic simulations formed by mapping the complex band-limited time-delay profiles onto a target area. (For an in-depth discussion on the image reconstruction, see Chapter 4.)

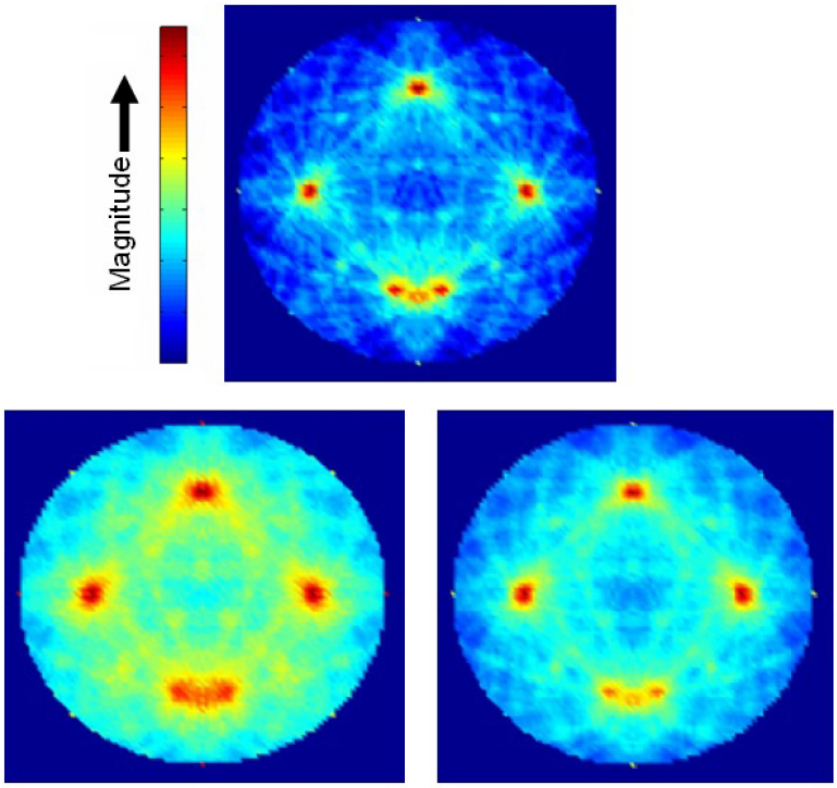

Figure 3.5: Output images of preliminary stepped-FMCW simulations reconstructed using time-delay profiles of varying bandwidths. As a percentage of sampling frequency (moving clockwise from top), they are 100%, 40%, 20%. Background clutter is due spectral filtering and the non-specific nature of the reconstruction algorithm.

Waveform Synthesis Simulation Experiments, Pt. III:

Time-Delay Profile Modification Using Pulse Echo Reflection

Because the extracted pulse echo was a sequence in time with an explicit sampling frequency, spectral components, and temporal pulse width, importing it to the stepped-FMCW simulation dimensionalizes the output image according

to the pulse echo experiment's environment. The process by which the extracted pulse echo was used to modify each of the theoretical multistatic time-delay profiles was accomplished with the following five steps:

1. Find the spectrum of the idealized time-delay profile,
   $P_{\text{theo}}[k] = \text{FFT}\Big\{ \textit{Theoretical time-delay profile} \Big\}$.

2. Shift the pulse echo time-delay profile to begin at $t = 0$. Find its spectrum
   $P_{\text{pulse}}[k] = \text{FFT}\Big\{ \textit{Extracted pulse echo} \Big\}$.

3. Zero out appropriate spectral samples from $P_{\text{pulse}}[k]$ to give $\hat{P}_{\text{pulse}}[k]$ in order to achieve desired stepped-FMCW frequency band.

4. Convolve the pulse echo time-delay profile with the theoretical time-delay profile by finding the product $P_{\text{synth}}[k] = P_{\text{theo}}[k]\hat{P}_{\text{pulse}}[k]$.

5. Take the IFFT of the $P_{\text{synth}}[k]$ to give the synthesized time-delay profile. (Fig. 3.6 shows a sample result.)

Waveform Synthesis Simulation Experiments, Pt. IV:

Results of Pulse Echo Synthesis with Stepped-FMCW Simulations

Simulations were performed with the element and target configurations seen in Fig. 3.4. The circular, eight-element conformal array with a diameter of 3 cm

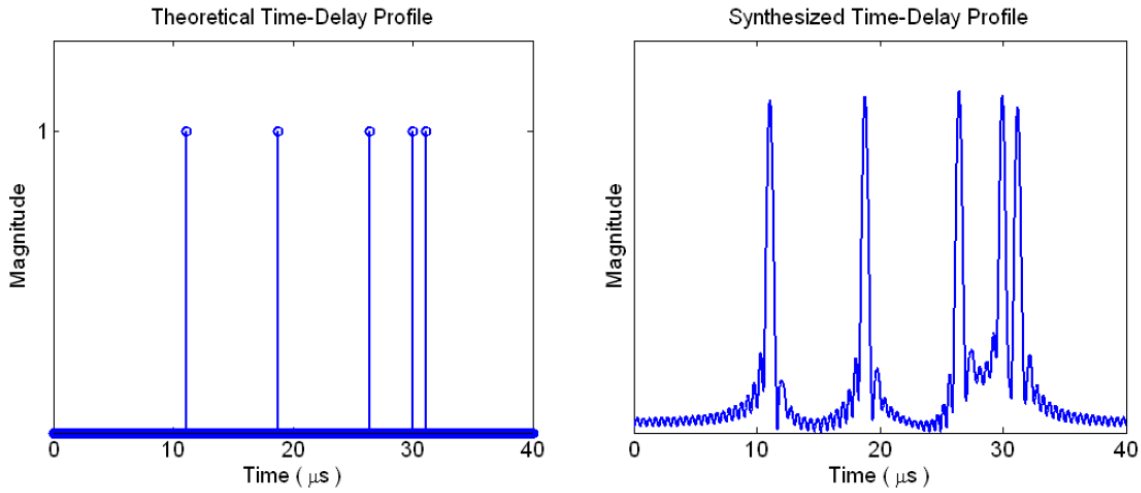

Figure 3.6: Sample time-delay profiles for a bistatic element pair in the stepped-FMCW simulation. The synthesized profile was found by convolving the theoretical profile with a bandlimited version of the extracted pulse echo.

was simulated to image five thin rod cross-sections in a soft-tissue phantom. To accommodate the dimensions of this setup, a maximum round-trip time of 40 µs was selected, establishing the stepped-FMCW $\Delta f = 25\,\text{kHz}$, its inverse. The upper bound of the FFT spectrum corresponded to the sampling frequency of the extracted pulse echo time-delay profile, 50 MHz. Two frequency bands were examined: (1)15.0 MHz to 15.5 MHz and (2) 13.0 MHz to 18.0 MHz. Note that these frequency ranges do not exceed the Nyquist frequency so that the frequency samples were confined to the positive sideband. A 2048-point IFFT was performed on the $P_{\text{synth}}[k]$ of each multistatic pair. The resulting time-delay profiles were then used to reconstruct an image by mapping them to a 267×267 matrix according to the propagation speed in the phantom, set to $1500\,\text{m}\,\text{s}^{-1}$.

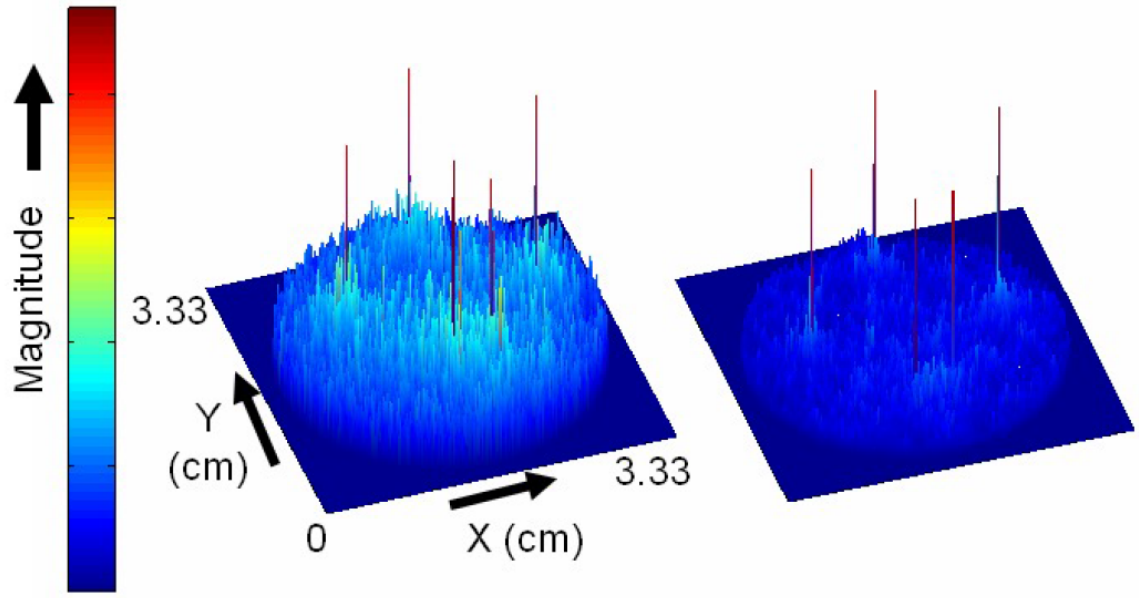

(a)

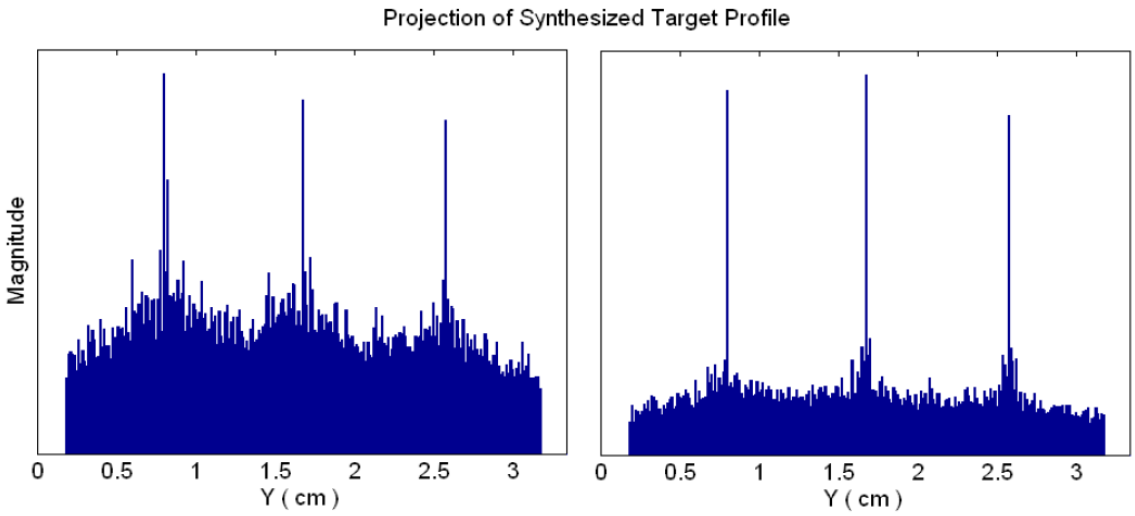

(b)

Figure 3.7: (a) Synthesized reconstructed images of a stepped-FMCW simulation using the experimentally acquired pulse echo waveform. Operating bands are 15.0 MHz to 15.5 MHz (left) and 13.0 MHz to 18.0 MHz (right). (b) Respective magnitude projections of the images onto the y-axis further reveals bandwidth effects.

The five targets in each of the resulting complex-magnitude images seen in Fig. 3.7 showed clear prominence over background clutter, and the change of bandwidth from $B = 0.5\,\text{MHz}$ to $B = 5\,\text{MHz}$ appreciably improved target clarity. Because the full circumferential aperture coverage removes distinction between the range and cross-range directions, the target position resolutions appear to benefit maximally from both. In terms of the spatial frequency span discussed in Chapter 2, the resulting coverage from each target position would roughly take the form of a flat donut with radial thickness $\frac{2B}{v}$. Its total span would be equal to

$$\Delta f_{\text{total}} = \Delta f_x = \Delta f_y = \frac{4}{\lambda_{\min}} = 4\,\frac{f_K}{v} \tag{3.22}$$

in all directions, or the diameter corresponding to the highest temporal frequency of the stepped-FMCW band, f_K. If we assume that this is the case for all five target positions, then the resolution is $24.2\,\mu\text{m}$ for the $15.0\,\text{MHz}$ to $15.5\,\text{MHz}$ bandwidth case, and $20.8\,\mu\text{m}$ for the $13.0\,\text{MHz}$ to $18.0\,\text{MHz}$ bandwidth case. As expected, the reconstruction shown in Fig. 3.7(b) suggests that the target resolution is well below the pixel spacing, $124.8\,\mu\text{m}$. Had Eq. (3.13) been naively used to estimate resolution solely based on stepped-FMCW operating bandwidth, the $15.0\,\text{MHz}$ to $15.5\,\text{MHz}$ case would predict a $1500\,\mu\text{m}$ target resolution. Therefore it is clear that the spatial frequency coverage due to the full aperture span domi-

nates the extent of the span in this case, and the analysis discussed in Chapter 2 is vital for understanding the resolution of novel array configurations.

3.2.2 Stepped-FMCW Ultrasonic Ranging Experiments

Laboratory experiments were conducted to compare the pulse echo and stepped-FMCW modalities specifically in ultrasonic ranging, and is documented in [44] by S. Natarjan et al., 2010. Presenting this work here will familiarize the reader with the physical aspect of stepped-FMCW implementation. Although phasor notation is a useful analytical tool, system design is concerned with purely real signals of finite duration. Hence, the stepped-FMCW data acquisition process can be reframed as follows.

Physical Stepped-FMCW Ranging Experiments, Pt. I: Methods

Beginning with the stepped CW frequencies from Eq. (3.3), we again have

$$f_k = f_0 + k\Delta f,$$

where f_k is the frequency of the transmitted signal, f_o the starting frequency, and $k = 0, 1, 2, ..., K-1$.

The transmitted signal is then

$$x_{\text{trans},k}(t) = \begin{cases} E\cos(2\pi f_k t), & \text{for } 0 \leq t \leq \Gamma \\ 0, & \text{otherwise} \end{cases} \tag{3.23}$$

where E is a constant amplitude and Γ is the CW signal duration. The received reflected signal sees a modified amplitude factor A and a phase shift ϕ:

$$x_{\text{rec},k}(t) = AE\cos(2\pi f_k t + \phi). \tag{3.24}$$

For each k, the received waveform is subsequently mixed with the transmitted CW signal for demodulation. This entails multiplying the received waveform by both the transmitted in-phase CW, $E\cos(2\pi f_k t)$, and a 90°-phase-offset CW, $E\sin(2\pi f_k t)$, yielding

$$y_{\text{I}}(t) = AE\cos(2\pi f_k t + \phi)E\cos(2\pi f_k t) \tag{3.25a}$$

$$y_{\text{Q}}(t) = AE\cos(2\pi f_k t + \phi)E\sin(2\pi f_k t). \tag{3.25b}$$

Following the demodulation step with a low-pass filter removes intermediate frequencies, which downconverts the signal to baseband:

$$y_{\mathrm{I,LP}}(t) = \frac{AE^2}{2}\cos(\phi) \tag{3.26a}$$

$$y_{\mathrm{Q,LP}}(t) = \frac{AE^2}{2}\sin(\phi). \tag{3.26b}$$

Together $y_{\mathrm{I,LP}}(t)$ and $y_{\mathrm{Q,LP}}(t)$ converge in time to constant values that depend on ϕ. These real values are known as I (in-phase) and Q (quadrature). Taking into account all CW frequencies used, the sequence of complex scalars can be constructed:

$$e_{\mathrm{demod}}[k] = I_k + jQ_k = M_k \exp(\phi), \tag{3.27}$$

where $M_k = \sqrt{I_k^2 + Q_k^2}$.

The custom transceiver system build for these experiments was designed to perform both pulse echo and stepped-FMCW signaling. Fig. 3.8 shows a block diagram. The transmitter was an arbitrary waveform generator capable of achieving 175 MSamples/s with an SNR of 70 dB at 20 MHz. Samples of the desired transmitted waveforms were designed on a PC and then transferred to a microcontroller. FIFO (first in, first out) buffers and a digital-to-analog converter (DAC) permitted CW signal operation at up to 166 MHz. Though the experiments called for only monostatic array operation, the inclusion of a multiplexor (MUX) allows for

array switching multistatic data acquisition. A transducer consisted of a single PZT piezoelectric element with a resonant frequency of 14 MHz and a bandwidth of 2 MHz.

The custom-fabricated transducer was fixed to a high-precision apparatus, shown in Fig. 3.9, which controlled its position to 0.5 mm resolution relative to a plastic tank filled with deionized water. Underwater ranging experiments were conducted by transmitting pulse echo and stepped-FMCW signals and receiving direct reflections off a face of the tank. Upon receiving the reflected signals, demodulation was performed to extract the I and Q signals.

Pulse echo ranging was carried out with a pulse width of 1 µm at 14 MHz. Stepped-FMCW ranging was accomplished within the range 13.50 MHz to 15.48 MHz and with a $\Delta f = 60$ kHz. However, though this would suggest that $K = 85$, the peaks and valleys within the designated bandwidth limited the functional frequencies to 34 in total. The IFFT was then performed in the same fashion, but instead of a full consecutive sequence of 85 non-zero complex scalars in the frequency domain band, the band contained only 34 values in their appropriate frequency bins.

Physical Stepped-FMCW Ranging Experiments, Pt. II: Results

Peaks in the reconstructed stepped-FMCW range profiles closely track those of the pulse echo profiles at various tested reflector distances, seen in Fig. 3.11. The

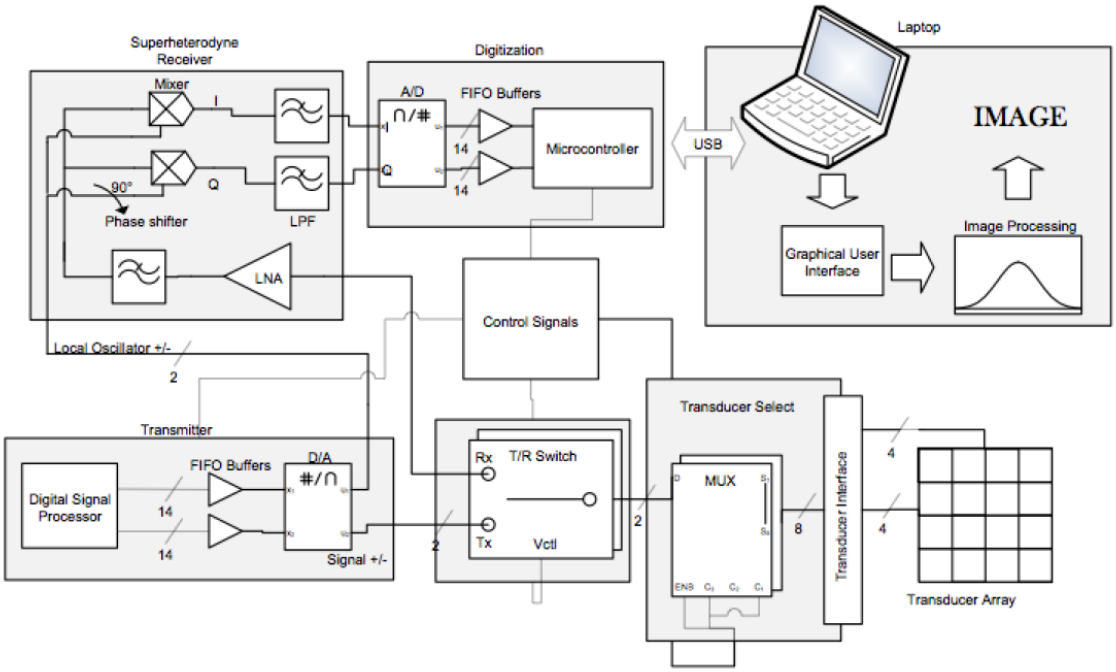

Figure 3.8: Overview of custom transceiver system.

highest peak in the profiles successfully track target distance within the 0.5 mm resolution of the positioning device. Results suggest that both modalities are similarly effective for ultrasonic ranging, agreeing with mathematical formulations described earlier.

Resolution was found to be approximately 500 µm. Using Eq. (3.13) would give a range resolution estimate of

$$\Delta x = \frac{v}{2B} \approx \frac{1500\,\mathrm{m\,s^{-1}}}{2(2\,\mathrm{MHz})} = 375\,\mu\mathrm{m}.$$

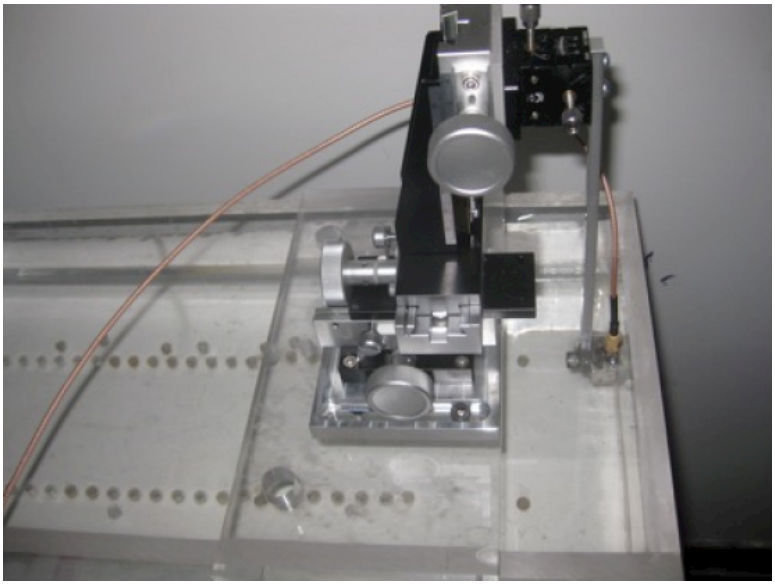

Figure 3.9: Transducer positioning mechanism used for water tank ranging experiments.

The discrepancy between observed range resolution and measured range resolution was likely due in large part to the piezoelectric element's inconsistent frequency response across its bandwidth. This is not taken into account by the calculation which assumes that all stepped CWs within the bandwidth provide equally strong data. But because the frequency response function peaks at the nominal resonant frequency value, 14 MHz, the stepped-FMCW bandwidth could not be fully exploited. Fig. 3.10 shows the frequency response. Hence, the stepped-FMCW modality can be expected to give results even closer to the theoretical resolution with the use of a commercial-grade transducer.

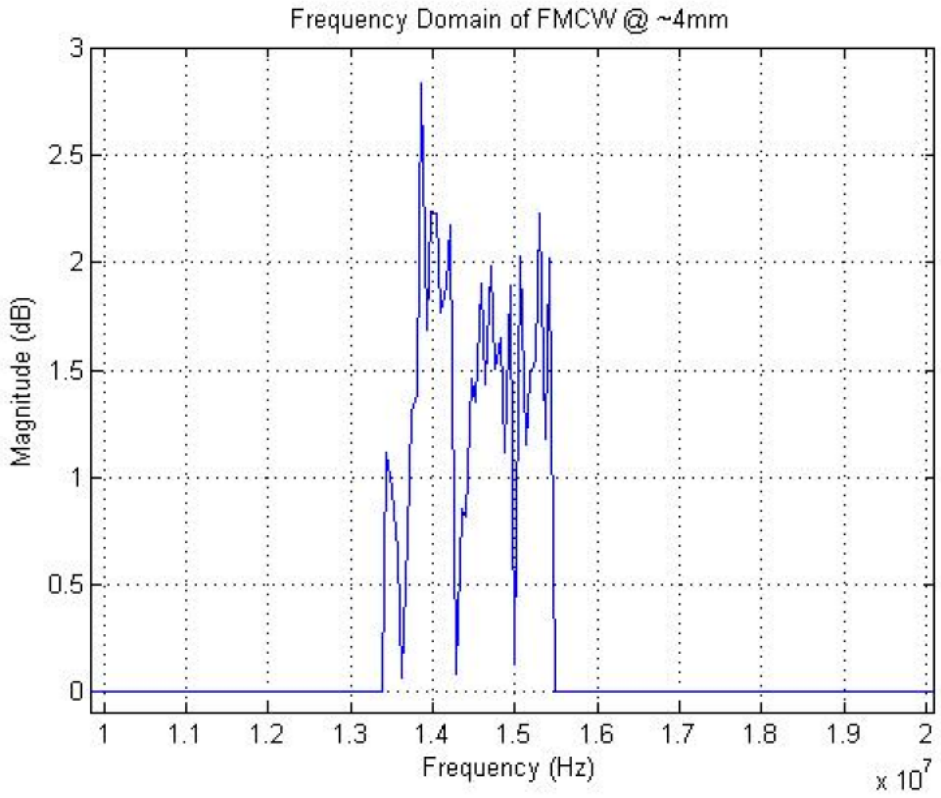

Figure 3.10: Frequency components of the stepped-FMCW spectrum prior to IFFT.

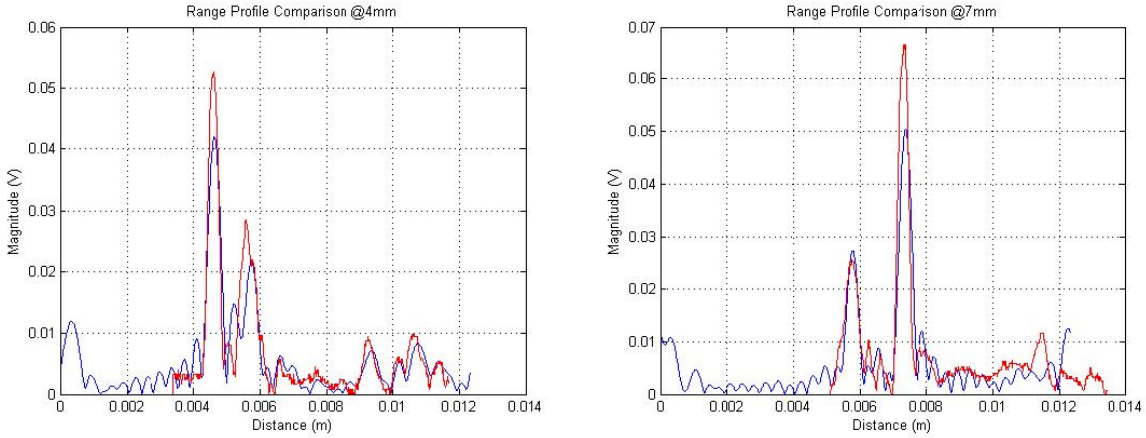

Figure 3.11: Range profile for a reflector distance of 4 mm (left) and 7 mm (right). Pulse echo results are shown in red and stepped-FMCW in blue.

3.3 Cramér-Rao Lower Bound for Range Resolution

To show the dependence of range resolution on system bandwidth from an alternate perspective, the Cramér-Rao Lower Bound (CRLB) can be analyzed in the context of range estimation [11], [30].

Supposing $\hat{r}$ to be an unbiased estimator of r, then

$$\mathrm{Var}(\hat{r}) \geq \mathrm{CRLB}(\hat{r}) = \frac{1}{I(r,\hat{r})}, \tag{3.28}$$

where $I(r,\hat{r})$ is the Fisher Information. This relationship reveals that the product between precision and information content is bounded by a constant.

For a range profile $s(r-\hat{r})$, the range delay $\hat{r}$ from a transmitted pulse $s(r)$ is estimated. The associated Fisher Information is

$$I(r,\hat{r}) = \frac{1}{\sigma^2}\int_{-\infty}^{+\infty}\left|\frac{\partial}{\partial\hat{\hat{r}}}s(r-\hat{r})\right|^2 \mathrm{d}r, \tag{3.29}$$

where σ^2 is the variance of the Gaussian additive noise probability density function (PDF).

Using Parseval's theorem, we can establish that

$$\begin{aligned}\int_{-\infty}^{+\infty} \left| \frac{\partial}{\partial \hat{\hat{r}}} s(r-\hat{r}) \right|^2 \mathrm{d}r &= \int_{-\infty}^{+\infty} \left| j2\pi f_r \exp\left(-j2\pi f_r \hat{r}\right) S(f_r) \right|^2 \mathrm{d}f_r \\ &= 4\pi^2 \int_{-\infty}^{+\infty} f_r^2 \left|S(f_r)\right|^2 \mathrm{d}f_r\end{aligned}$$

which can be expressed as

$$\begin{aligned}&= 4\pi^2 \left[\int_{-\infty}^{+\infty} \left|S(f_r)\right|^2 \mathrm{d}f_r\right] \int_{-\infty}^{+\infty} f_r^2 \frac{\left|S(f_r)\right|^2}{\left[\int_{-\infty}^{+\infty} \left|S(f_r)\right|^2 \mathrm{d}f_r\right]} \mathrm{d}f_r \\ &= 4\pi^2 (\text{Energy}) \int_{-\infty}^{+\infty} f_r^2 \, p(f_r) \, \mathrm{d}f_r \\ &= 4\pi^2 (\text{Energy}) B_{\text{RMS}}^2,\end{aligned} \tag{3.30}$$

where B_{RMS} is some root-mean-square bandwidth, and $p(f_r)$ is the probability density function of f_r.

Substituting this expression back into Eq. (3.29) gives

$$\begin{aligned}I(r,\hat{r}) &= 4\pi^2 \left(\frac{\text{Energy}}{\sigma^2}\right) B_{\text{RMS}}^2 \\ &= 4\pi^2 (\text{SNR}) B_{\text{RMS}}^2,\end{aligned} \tag{3.31}$$

which in turn gives the CRLB:

$$\mathrm{Var}(\hat{r}) \geq \frac{1}{4\pi^2(\mathrm{SNR})B_{\mathrm{RMS}}^2}. \tag{3.32}$$

Taking the square root then gives the standard deviation:

$$\sigma(\hat{r}) \geq \frac{1}{2\pi\sqrt{(\mathrm{SNR})}B_{\mathrm{RMS}}}. \tag{3.33}$$

The value of $\sigma(\hat{r})$ describes the same notion as range resolution, as their units are consistent. This inverse relationship with bandwidth agrees with the prior range resolution expression seen in Eq. (3.13) [19], [54]. Although this result is based on a 1-D ranging case, a 2-D scenario would involve two spatial directions represented by functions $\sigma_x(\hat{r})$ and $\sigma_y(\hat{r})$ along with their respective bandwidths and SNRs. The resolution analysis in Chapter 2 is approached similarly, giving rise to the range and cross-range resolution conventions.

The limitation on resolution in the CRLB sense can be seen as an analog to relationships in other fields, including Heisenberg's uncertainty principle and Rayleigh criterion.

3.4 Conclusion

In this chapter, we have established that the spectrum band of a pulse echo time-delay profile are the frequencies used in the stepped-FMCW band. The process of generating time-delay profiles from stepped-FMCW data is also discussed. From this, we describe a method for using available pulse echo data to dimensionalize a stepped-FMCW simulation to the same imaging environment. This is of particular value if stepped-FMCW data acquisition is not an immediate option. Circular aperture simulations confirm that arrays need not be linear for ultrasonic multistatic ranging and imaging. Image reconstruction is briefly explained although the following chapter offers a more complete picture.

Laboratory ranging experiments were conducted in water to compare the pulse echo and stepped-FMCW modality. A reflective wall varying between 4 mm and 30 mm away from a monostatic transducer was used as the ranging target. An overview of the system architecture is provided. Results show that stepped-FMCW is as successful as pulse echo for giving accurate range profiles in the ultrasonic environment.

Chapter 4

Image Reconstruction for a Stepped-FMCW Reconfigurable Array Imaging System

Because we expect a system user to be dynamically changing the array configuration, a suitable imaging algorithm would see minimal new calculations for each shift in element positioning, as well as a reconstruction process that is as independent as possible from the array structure. Current ultrasound imaging technologies such as phased arrays, capitalize on the rigid form of the element positions to streamline the probing and reconstruction algorithms. Therefore, a phased array approach is not suitable for a reconfigurable array system. Instead we investigate an backward propagation method for estimating a target distribution, specifically a space-time reconstruction that can readily accommodate an arbitrary element configuration.

In this chapter, we assume that the imaging system is capable of multistatic operation of an array of elements. That is, the programmed operation can synchronize the switching between transmit and receive of each element. Additionally, it is assumed that the system is able to detect the relative positioning of the elements.

References [39], [37], [52], [9], and [8] form the basis of this chapter.

4.1 Backward Propagation

Backward propagation is the concept of undoing the effect of wave propagation in the acquired dataset. This allows received data to be transformed into an estimate of the target or source distribution, in the form of a reconstructed image. We will first review the passive, continuous case and then establish its extension to multistatic and stepped-frequency.

For passive coherent wave propagation, consider a source distribution $s(x, y)$ in $\mathbb{R}^2$ that emits with wavelength λ. The result is a wavefield $g(x, y, \lambda)$ given

by a convolution over (x, y) of $s(x, y)$ with the Green's function for coherent propagation, $h(x, y, \lambda)$, similar to Eq. (2.1).

$$\begin{aligned} g(x, y, \lambda) &= s(x, y) * h(x, y, \lambda) \\ &= \int_{Y'} \int_{X'} s(x', y') \, \frac{1}{j\lambda r} \, \exp\left(j \frac{2\pi r}{\lambda}\right) \, \mathrm{d}x' \, \mathrm{d}y', \end{aligned} \tag{4.1}$$

where $r = \sqrt{(x - x')^2 + (y - y')^2}$.

The backward propagation algorithm reconstructs the source distribution $s(x, y)$ by convolving the wavefield data with the *conjugate* of the forward-propagating Green's function:

$$\begin{aligned} s(x, y) &= g(x, y, \lambda) * h^*(x, y, \lambda) \\ &= \int_{\Lambda} \int_{Y'} \int_{X'} g(x', y', \lambda) \, \frac{-1}{j\lambda r} \, \exp\left(-j \frac{2\pi r}{\lambda}\right) \, \mathrm{d}x' \, \mathrm{d}y' \, \mathrm{d}\lambda. \end{aligned} \tag{4.2}$$

It is worth noting that SAR reconstruction exploits a special case of the backward propagation algorithm. Since the basic monostatic SAR system operates in the far-field, the Fraunhofer approximation applies. Two-dimensional reconstruction can them be achieved by a direct 2-D FFT of the received wavefield data (along the temporal frequency and spatial dimensions) due to the Fourier trans-

form pair of the data and target distribution. In that sense, the reconstruction is optimal by virtue of the orthogonality of the monostatic data samples. However, this thesis does not discriminate between near-field and far-field cases and therefore presents the reconstruction algorithm in the above form.

4.1.1 Passive Backward Propagation with Finite Frequencies and Transceiver Elements

Since stepped-FMCW system specifications are typically in terms of frequency instead of wavelength, the variable λ can be replaced by $\frac{v}{f}$, where v is the speed of sound in the propagation medium and f is the frequency of the illumination CW in the medium. Eq. (4.1) can then be rewritten as

$$g(x, y, f) = \int_{Y'} \int_{X'} s(x', y') \, \frac{f}{jvr} \, \exp\left(j \frac{2\pi f r}{v}\right) \, \mathrm{d}x' \, \mathrm{d}y' \tag{4.3}$$

Likewise, the backward propagated source distribution becomes:

$$s(x, y) = \int_{F} \int_{Y'} \int_{X'} g(x', y', f) \, \frac{-f}{jvr} \, \exp\left(-j \frac{2\pi f r}{v}\right) \, \mathrm{d}x' \, \mathrm{d}y' \, \mathrm{d}f, \tag{4.4}$$

where $r = \sqrt{(x - x')^2 + (y - y')^2}$.

The presence of elements at specific locations (x_m, y_m) means also that the wavefield is being sampled at those locations. Combining this with a finite number of frequency steps f_k, the *detected* wavefield $\hat{g}(x, y)$ can be expressed as

$$\begin{aligned}\hat{g}(x,y,f) &= (u_1(x,y,f) + g(x,y,f)) \sum_m \sum_k \delta(x - x_m, y - y_m, f - f_k) \\ &= \sum_m \sum_k (u_1(x_m, y_m, f_k) + g(x_m, y_m, f_k))\, \delta(x - x_m, y - y_m, f - f_k) \\ &= \sum_m \sum_k \hat{g}_m[k]\, \delta(x - x_m, y - y_m, f - f_k),\end{aligned} \tag{4.5}$$

where $\hat{g}_m[k]$ is the sampled wavefield, $(u_1(x_m, y_m, f_k) + g(x_m, y_m, f_k))$. The function u_1 serves to account for practical deviations from the ideal wavefield, such as

wave attenuation and noise. We can then use the result to rewrite the backward propagated source estimate, or the reconstructed image:

$$\begin{aligned}
\hat{s}(x,y) &= \hat{g}(x,y,f) * h^*(x,y,f) \\
&= \int_F \int_{Y'} \int_{X'} \sum_m \sum_k \hat{g}_m[k]\, \delta(x-x_m, y-y_m, f-f_k)\, \frac{-f}{jvr}\, \exp\left(-j\frac{2\pi f r}{v}\right) \mathrm{d}x'\, \mathrm{d}y'\, \mathrm{d}f \\
&= \sum_m \sum_k \int_F \hat{g}_m[k]\, \delta(f-f_k)\, \frac{-f}{jvr}\, \exp\left(-j\frac{2\pi f r}{v}\right) \mathrm{d}f \\
&= \sum_m \sum_k \hat{g}_m[k]\, \frac{-f_k}{jvr}\, \exp\left(-j\frac{2\pi f_k r}{v}\right),
\end{aligned} \tag{4.6}$$

where $r = \sqrt{(x-x_m)^2 + (y-y_m)^2}$.

Because $f_k = f_o + k\Delta f$ for $0 \leq k \leq (K-1)$, a substitution can be done to directly reveal the dependence on k. The summation over k can then be seen as a K-point DFT, by virtue of the minus sign in the exponential:

$$\begin{aligned}
\hat{s}(x,y) &= \sum_m \sum_k \hat{g}_m[k] \, \frac{-f_k}{jvr} \, \exp\left(-j\frac{2\pi(f_o + k\Delta f)r}{v}\right) \\
&= \sum_m \sum_k \left\{ \frac{-f_k}{jvr} \exp\left(-j\frac{2\pi f_o r}{v}\right) \, \hat{g}_m[k] \right\} \exp\left(-j\frac{2\pi(k\Delta f)r}{v}\right) \\
&= \sum_m \mathrm{DFT}\left\{ \frac{-f_k}{jvr} \exp\left(-j\frac{2\pi f_o r}{v}\right) \, \hat{g}_m[k] \right\} \\
&= \sum_m \hat{p}_{\mathrm{tdp},m}[n],
\end{aligned} \tag{4.7}$$

where $\hat{p}_{\mathrm{tdp},m}[n]$ is the sampled estimate of the theoretical time-delay profile. This image formation process is known as *space-time* reconstruction. A different way of evaluating the summations in Eq. (4.6) is by *spatial-frequency* reconstruction, which will be discussed at a later point.

In a manner similar to Eq. (3.9), it can be shown that the DFT result is a K-point sequence $\hat{p}_{\mathrm{tdp},m}[n]$ indexed by n when

$$n = K\Delta f \frac{r}{v} = \frac{Br}{v} = B\tau_o.$$

Because r is the range from a passive system (one-way propagation), we may avoid confusion by simply turning our attention to τ_o instead, which is the overall time delay whether for a one-way propagation (passive) or round-trip (monostatic and bistatic). Due to the linear relationship between n and τ_o, $\hat{p}_{\mathrm{tdp},m}[n]$ constitutes the time-delay profile, albeit raw without post-processing procedures. The formation of the time-delay profile is dictated by the exponential function of the DFT, meaning that scaling factors in the magnitude is only of secondary consideration. Therefore, it is certainly possible to approximate the reconstruction as the DFT of the received data alone.

$$\hat{p}_{\mathrm{tdp},m}[n] \approx \mathrm{DFT}\Big\{\hat{g}_m[k]\Big\}.$$

We have now described the role of the time-delay profile in the image reconstruction $\hat{s}(x, y)$ for a passive stepped-FMCW system. Eq. (4.7) concludes that a final summation over m is necessary to arrive at the image. This entails a superimposition of the sequence values of $\hat{p}_{\mathrm{tdp},m}[n]$ over the space (x, y), relative to the element position (x_m, y_m). If we define this result as the function

$\hat{p}_{\text{tdp\_mapped},m}(x,y)$, a modified version of Eq. (4.7) can be expressed that more closely characterizes the practical aspect of the reconstruction:

$$\hat{s}(x,y) = \sum_m u_{2,m}(x,y)\, \hat{p}_{\text{tdp\_mapped},m}(x,y), \tag{4.8}$$

where the function $u_{2,m}(x,y)$ is a mask over (x,y) that is applied during post-processing. It accounts for spatial anisotropy of the time-delay profile data, such as those due to beampatterns. A well-defined acoustic beam from an element would mean that during reconstruction, its time-delay profile values need not be superimposed at some set of (x,y) locations because of limitations in angular illumination. By applying this mask, directionality can be specified as well as the inclusion of other post-processing algorithms including normalization, time-gain control, and thresholding.

4.1.2 Maximum Likelihood Estimator

To legitimize the path to the reconstruction result, we first establish a relationship between the true target distribution and a single time-delay profile mapping:

$$v_m(x,y) = \hat{p}_{\text{tdp\_mapped},m}(x,y) - \hat{s}(x,y), \tag{4.9}$$

where the additive noise term $v_m(x, y)$ spans (x, y) and has a Gaussian probability density function (PDF) with zero mean:

$$p(\, v_m(x, y)\,) = c_m(x, y)\, \exp\left(-\frac{v_m^2(x, y)}{2\sigma_m^2(x, y)}\right), \tag{4.10}$$

where $\sigma_m^2(x, y)$ is the variance of the PDF and $c_m(x, y)$ is a real constant. The joint probability across M subimages is then

$$p_{\text{joint}}(\, v_m(x, y)\,) = \prod_{m=1}^{M} c_m(x, y)\, \exp\left(-\frac{v_m^2(x, y)}{2\sigma_m^2(x, y)}\right), \tag{4.11}$$

which leads to the likelihood function of the process:

$$\begin{aligned} L(\, v_m(x, y)\,) &= \ln(\, p_{\text{joint}}(\, v_m(x, y))\,) \\ &= \sum_{m=1}^{M} \ln(c_m(x, y)) - \sum_{m=1}^{M} \frac{v_m^2(x, y)}{2\sigma_m^2(x, y)} \\ &= \sum_{m=1}^{M} \ln(c_m(x, y)) - \sum_{m=1}^{M} \frac{(\hat{p}_{\text{tdp\_mapped},m}(x, y) - \hat{s}(x, y))^2}{2\sigma_m^2(x, y)}. \end{aligned} \tag{4.12}$$

Notice that maximizing the likelihood function entails minimizing $v_m^2(x,y)$, implying a least-squares-error between $\hat{p}_{\text{tdp\_mapped},m}(x,y)$ and $\hat{s}(x,y)$ [51]. To maximize the likelihood function, we take its derivative and set it to zero:

$$\begin{aligned}\frac{\partial}{\partial s}L(\,v_m(x,y)) &= -\sum_{m=1}^{M} -2\,\frac{\hat{p}_{\text{tdp\_mapped},m}(x,y)-\hat{s}(x,y)}{2\sigma_m^2(x,y)} \\ &= \sum_{m=1}^{M}\frac{\hat{p}_{\text{tdp\_mapped},m}(x,y)-\hat{s}(x,y)}{\sigma_m^2(x,y)} \\ &= 0.\end{aligned} \tag{4.13}$$

Assuming that the variance does not change with m such that $\sigma_m^2(x,y) = \sigma^2(x,y)$, the resulting expression for the maximum likelihood estimator for $\hat{s}(x,y)$ is

$$\hat{s}_{\text{ML}}(x,y) = \frac{1}{M}\sum_{m=1}^{M}\hat{p}_{\text{tdp\_mapped},m}(x,y). \tag{4.14}$$

If the masking function u_2 is ignored, this is precisely a scaled version of the image reconstruction process from Eq. (4.8).

4.2 Reconstruction Algorithm for Active Multistatic Imaging

Given a dataset consisting of received passive coherent frequency data points (indexed by k) for each element (indexed by m), Eq. (4.6) establishes the mathematical form for arriving at the target reconstruction. However, active multistatic operation necessitates a broadening of the meaning of m to an index of all multistatic element pairs, instead of solely the elements themselves.

The order in which the two summations over m and k are carried out splits the reconstruction process into two distinct methods: (1) Spatial-frequency reconstruction, and (2) Space-time reconstruction. Although both techniques will be discussed in this section for completeness, space-time reconstruction is emphasized because it is most logical for a reconfigurable array imaging system.

As we are now discussing images consisting of discrete pixels over (x, y), we can refer to the reconstructed image as a matrix $\hat{s}[\hat{i}, \hat{j}]$ where $1 \leq \hat{i} \leq I$ and $1 \leq \hat{j} \leq J$. Row position is denoted by $\hat{i}$ and column position by $\hat{j}$, with the origin at the upper-left corner of the image. A parameter Δx_{pix} is the true length represented by a square pixel.

4.2.1 Spatial-frequency Image Reconstruction (Monostatic)

Reconstructing an image by way of spatial-frequency refers to the generation of K subimages of the same dimension as $\hat{s}[\hat{i},\hat{j}]$, each representing the contribution from a single frequency within the stepped-FMCW band. These single-frequency subimages are then superimposed to form the final reconstructed image.

Borrowing from Eq. (4.6), we can express the monostatic spatial-frequency reconstruction in $\mathbb{R}^2$ as:

$$\begin{aligned}\hat{s}[\hat{i},\hat{j}] &= \hat{g}[\hat{i},\hat{j}] * h^*[\hat{i},\hat{j}] \\ &= \sum_k \left\{ \sum_m \hat{g}_m[k] \, \frac{-f_k}{jvr} \, \exp\left(-j\frac{2\pi f_k r}{v}\right) \right\} \\ &= \sum_k \left\{ \, \hat{s}_k[\hat{i},\hat{j}] \, \right\},\end{aligned} \tag{4.15}$$

where the total propagation range is $r = 2\,\Delta x_{\text{pix}} \sqrt{(\hat{i}-\hat{i}_m)^2 + (\hat{j}-\hat{j}_m)^2}$, and $\hat{s}_k[\hat{i},\hat{j}]$ is the k^{th} frequency subimage. The m^{th} monostatic element is located at $[\hat{i}_m,\hat{j}_m]$. A single-frequency subimage is formed by a convolution between the received I/Q data with the backpropagation kernel.

Reconstruction of bistatic data using the spatial-frequency approach is beyond the scope of this thesis.

Spatial-Frequency Reconstruction of Ground-Penetrating Radar Data

To illustrate this process, data from a ground-penetrating radar (GPR) operating in a monstatic stepped-FMCW modality was used reconstruct a subsurface cross-sectional image using the spatial-frequency approach. Reference [36] describes this experiment. The experiment was conducted to image metal reinforcement bars embedded beneath a concrete walkway, shown in Fig. 4.1. Despite the use of electromagnetic waves instead of ultrasonic compression waves, the reconstruction process remains the same. Additionally, in lieu of an array of transceivers, a single-element synthetic aperture scheme was used to acquire data at $M = 200$ evenly-spaced positions across a 4.26 m ground length, in a direction perpendicular to the orientation of the subsurface reinforcement bars. Therefore, the synthetic aperture acted as a 200-element linear array with element spacing of $\Delta x_e = 2.13\,\text{cm}$.

For each monostatic position, the data consisted of $K = 128$ stepped frequencies through an operating band between 0.976 GHz and 2.00 GHz with a $\Delta k = 800\,\text{MHz}$. The dimensions of the image matrix $\hat{s}[\hat{i}, \hat{j}]$ were chosen such that $I = 18$ and $J = 200$. In real terms, this corresponded to an imaging area of length 4.26 m and a depth of 0.2 m with an image pixel length Δx_{pix} equal to Δx_e.

Fig. 4.2 shows the reconstruction result, which assumes isotropic beampattern by nature of the procedure. Each coherent subimage $\hat{s}_k[\hat{i}, \hat{j}]$ was constructed row-

wise. To obtain the $\hat{i}^{th}$ row of $\hat{s}_k[\hat{i},\hat{j}]$, a convolution of the following two sequences was performed:

1. A 200-point sequence $\alpha_{\hat{i}}[k]$ consisting of the consecutively received data $\hat{g}$ for all 200 positions but for only a single f_k.

2. A 1024-point sequence

$$\beta_{\hat{i}}[n] = \frac{-f_k}{jvr} \exp\left(-j\,2\pi\,\frac{f_k r}{v}\right), \tag{4.16}$$

where $r = 2\,\Delta x_{\text{pix}}\sqrt{\hat{i}^2 + (n-512)}$.

The convolution was implemented by multiplying their respective 1024-point FFT results, and then taking a 1024-point IFFT of the result. This results in a 1024-point sequence, and the portion from the 513^{rd} to the 712^{th} indices gives the $\hat{i}^{th}$ row of $\hat{s}_k[\hat{i},\hat{j}]$.

Because efficient spatial-frequency reconstruction relies on the linear and evenly-spaced element positions, it is not a suitable choice for a reconfigurable array whose element distribution is arbitrary. The spatial-frequency method can, however, easily accommodate arbitrary spacing of the frequencies f_k because superimposing a set coherent subimages does not present any particular constraints.

Figure 4.1: Imaged walkway area and reinforcement bars prior to concrete overlay.

(a) The first stepped-FMCW coherent subimage, $k = 1$.

(b) Superimposed coherent subimages, from $k = 1$ to $k = 42$.

(c) Superimposed coherent subimages, from $k = 1$ to $k = 84$.

(d) Final reconstruction with 128 superimposed coherent subimages, from $k = 1$ to $k = 128$.

Figure 4.2: Spatial-frequency reconstruction of reinforcement bars in concrete. The images represent a length of 4.36 m and depth of 0.2 m.

4.2.2 Multistatic Space-Time Image Reconstruction

Where spatial-frequency reconstruction is most applicable in uniform element spacing, space-time reconstruction is conversely most applicable when there is a uniform stepped-FMCW frequency spacing, Δf, independent of element positioning. Because a reconfigurable array system must reconstruct images from arbitrary element positions, the space-time method is the focus of this thesis. In contrast to the coherent subimage summation, the final space-time reconstruction step involves a summation of mapped time-delay profiles over $[\hat{i}, \hat{j}]$:

$$\begin{aligned}
\hat{s}[\hat{i},\hat{j}] &= \hat{g}[\hat{i},\hat{j}] * h^*[\hat{i},\hat{j}] \\
&= \sum_m \sum_k \left\{ \frac{-f_k}{jvr} \exp\left(-j\frac{2\pi f_o r}{v}\right) \hat{g}_m[k] \right\} \exp\left(-j\frac{2\pi(k\Delta f)r}{v}\right) \\
&= \sum_m \mathrm{DFT}\left\{ \frac{-f_k}{jvr} \exp\left(-j\frac{2\pi f_o r}{v}\right) \hat{g}_m[k] \right\} \\
&= \sum_m \left\{ \hat{p}_{\mathrm{tdp},m}[n] \right\},
\end{aligned} \tag{4.17}$$

where r is the round-trip propagation range. A space-time subimage $\hat{s}_m[\hat{i},\hat{j}]$ can then be formed by mapping the sequence $\hat{p}_{\mathrm{tdp},m}[n]$ over $[\hat{i},\hat{j}]$ relative to the m^{th} multistatic position(s):

$$\hat{s}[\hat{i},\hat{j}] = \sum_{m} \Big\{ \mu_m[\hat{i},\hat{j}]\, \hat{s}_m[\hat{i},\hat{j}] \Big\}. \tag{4.18}$$

Similar to $u_{2,m}$ in Eq. (4.8), a function $\mu_m(\hat{i},\hat{j})$ that accounts for beampattern may be multiplied to $\hat{s}_m[\hat{i},\hat{j}]$ prior to summing.

Mapping of Time-Delay Profiles to Form Space-Time Subimage $\hat{s}_m[\hat{i},\hat{j}]$

In $\mathbb{R}^2$, moving from Eq. (4.17) to Eq. (4.18) requires that the time-delay profile $\hat{p}_{\mathrm{tdp},m}[n]$ be converted into the subimage $\hat{s}_m[\hat{i},\hat{j}]$.

For a monostatic data track, each pixel in $\hat{s}_m[\hat{i},\hat{j}]$ represents a round-trip wave propagation distance $r_{\mathrm{mono}}[\hat{i},\hat{j}]$ from the element position $[\hat{i}_{\mathrm{mono}},\hat{j}_{\mathrm{mono}}]$:

$$r_{\mathrm{mono}}[\hat{i},\hat{j}] = 2\,\Delta x_{\mathrm{pix}} \sqrt{(\hat{i}_{\mathrm{mono}}-\hat{i})^2 + (\hat{j}_{\mathrm{mono}}-\hat{j})^2}. \tag{4.19}$$

For a bistatic data track, the round-trip wave propagation distance is the sum of two distances: one from the transmitting element at $[\hat{i}_{\mathrm{trans}},\hat{j}_{\mathrm{trans}}]$ to the

pixel location, and the other from the pixel location to the receiving element at $[\hat{i}_{\text{rec}}, \hat{j}_{\text{rec}}]$:

$$r_{\text{bi}}[\hat{i}, \hat{j}] = \Delta x_{\text{pix}} \left(\sqrt{(\hat{i}_{\text{trans}} - \hat{i})^2 + (\hat{j}_{\text{trans}} - \hat{j})^2} \; + \; \sqrt{(\hat{i}_{\text{rec}} - \hat{i})^2 + (\hat{j}_{\text{rec}} - \hat{j})^2} \right). \tag{4.20}$$

The corresponding time delays for either monostatic or bistatic cases are:

$$\tau[\hat{i}, \hat{j}] = \frac{r[\hat{i}, \hat{j}]}{v}. \tag{4.21}$$

If in practice there is a known set of reconfigurable element positions, a lookup table can be computed in advance. This means that all values of $\tau_m[\hat{i}, \hat{j}]$ can be determined and stored prior to data acquisition which reduces the processing time for reconstruction.

For each pixel in $\hat{s}_m[\hat{i},\hat{j}]$, the value $\tau_{i,j}$ then corresponds to some index $n_{i,j}$ in $\hat{p}_{\text{tdp},m}[n]$, where

$$\begin{aligned} n_{\hat{i},\hat{j}} &= \text{ceiling}\Big\{(\text{DFT size})\,\frac{\text{time delay at } [\hat{i},\hat{j}]}{\text{total possible time delay expressed with } \hat{p}_{\text{tdp}}}\Big\} \\ &= \text{ceiling}\Big\{(\text{DFT size})\,\frac{\tau_{\hat{i},\hat{j}}}{\frac{1}{\Delta f}}\Big\} \\ &= \text{ceiling}\Big\{(\text{DFT size})\,(\Delta f)\,(\tau_{\hat{i},\hat{j}})\Big\}. \end{aligned} \tag{4.22}$$

Since the smallest value that $n_{i,j}$ can take on is 1, the special case where $\tau_{\hat{i},\hat{j}} = 0$ must be addressed separately. The space-time subimage can then be formed pixelwise:

$$\hat{s}_m[\hat{i},\hat{j}] = \hat{p}_{\text{tdp},m}[n_{\hat{i},\hat{j}}]. \tag{4.23}$$

For a monostatic time-delay profile with a single visible peak, the resulting space-time subimage will show a circular arc of high magnitude, centered about the element location. A similar time-delay profile from a bistatic track will show an elliptical arc with the transmitting and receiving elements at the foci locations. (Other forms of target localization, such as for underwater acoustic networks [15] and bistatic SAR [62], are also described in the same way.) This is evident in Fig. 4.3, which shows a simulated space-time reconstruction assuming isotropic

beampatterns. Attenuation compensation was not included. A single reflective target (in blue) was imaged by two elements (in red) over a 5 mm × 5 mm area. The operating stepped-FMCW bandwidth was 10 MHz. The reconstruction was performed with 4 time-delay profiles, one for each multistatic track. The bistatic contribution is of higher magnitude due to two overlapping contributions (transmit/receive and receive/transmit).

The addition of a simple binary beampattern mask, as described in Eq. (4.18) was then applied to this simulation. The results are shown in Fig. 4.4. A 60°directed acoustic beamspread was defined for both elements such that pixels outside its boundaries are ignored by the reconstruction. Bistatic contributions require that there exists a zone of mutual illumination.

Space-Time Reconstruction of Ground-Penetrating Radar Data

To illustrate space-time reconstruction, the same monostatic GPR data from [36] was reconstructed with the space-time method. To maintain consistency with the assumed isotropic beampattern spatial-frequency reconstruction, the space-time reconstruction was performed with all values in $\mu_m(\hat{i}, \hat{j})$ set to ones. For each of the 200 monostatic element positions, a time-delay profile was generated by taking a 2048-point FFT. Fig. 4.5 shows the results.

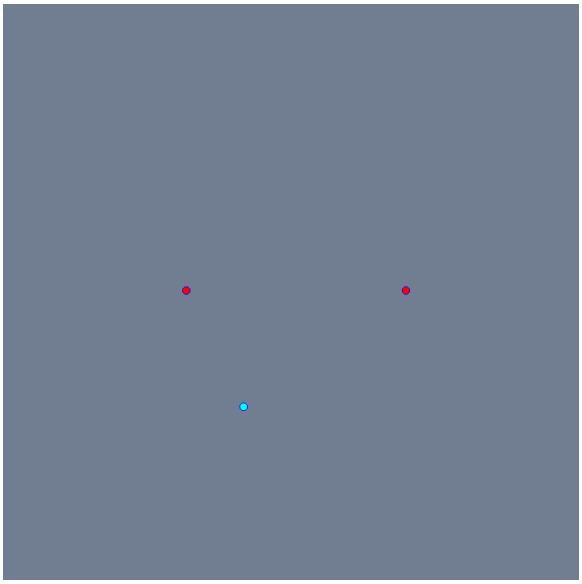

(a) Target and element arrangement over a 5 mm × 5 mm area.

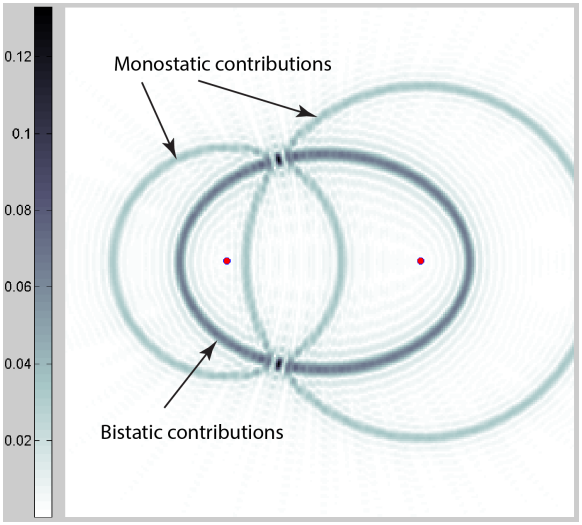

(b) Reconstruction using two bistatic tracks and two monostatic tracks.

Figure 4.3: Space-time reconstruction of two multistatic elements (red) imaging a single target (blue).

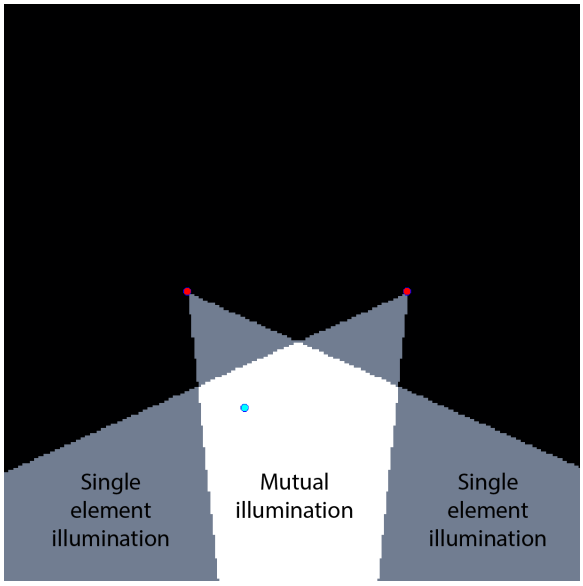

(a) Target and element arrangement showing a 30°beamspread constraint on the elements.

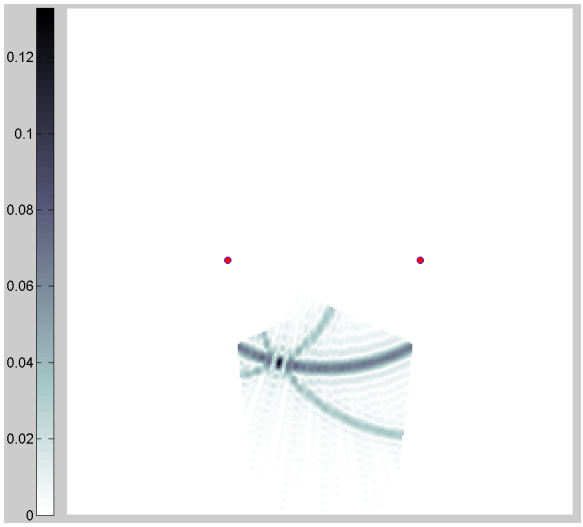

(b) Reconstruction showing a limited applicable area as a result of binary beamspread.

Figure 4.4: Space-time reconstruction of two multistatic elements with limited beamspread.

(a) Subimage generated from the first (left-most) element contribution, $m = 1$.

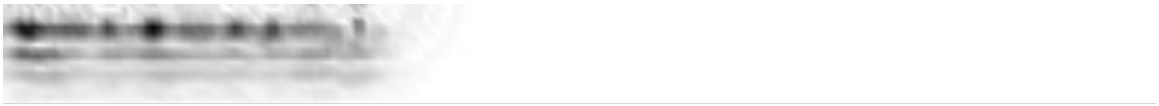

(b) Superimposed subimages generated from contributions from 42 elements, $m = 1$ to $m = 42$.

(c) Superimposed subimages generated from contributions from 132 elements, $m = 1$ to $m = 132$.

(d) Final reconstruction with 200 superimposed element subimages, from $m = 1$ to $m = 200$.

Figure 4.5: Space-time reconstruction of reinforcement bars in concrete. The images represent a length of 4.36 m and depth of 0.2 m.

GPR Reconstruction Comparison By Structural Similarity (SSIM)

For the same dataset, the space-time reconstruction gives a result nearly identical to that of the spatial-frequency reconstruction. This confirms that both image formations methods arrive at the same result. Because the GRP experiment was conducted with both a uniformly-spaced linear synthetic array and uniformly-space frequency data, this reconstruction comparison was possible.

To analyze the similarity between the two reconstructions, the structural similarity (SSIM) index [66] [65] was used. This was investigated by Wang et. al. as a way of quantifying the similarity between two images as perceived by the human visual system. In its default usage, the SSIM algorithm takes as inputs two test images with a dynamic range of [0,255] and outputs a single value ranging from 0 to 1. This value is known as the mean structural similarity (MSSIM), which is 0 for when the two images are completely dissimilar and 1 when they are identical. Unlike common image assessment metrics such as mean-squared error (MSE) and peak signal-to-noise ratio (PSNR), MSSIM takes into account perceived visual acuity by detecting local patterns and structures [66].

With default SSIM settings, the comparison result for the space-time and spatial frequency GRP data reconstructions was MSSIM = 0.8774. We would not expect a result of unity because the two methods have different sources of error in their implementations. In particular, because the space-time reconstruction uses

a nearest next integer routine as seen in Eq. (4.22), rounding error may account for much of the dissimilarity. Using a 2048-point FFT size to interpolate the time-delay profile and reduce rounding error helped immensely in the quality of the reconstruction. The space-time reconstruction performed with only a 128-point FFT resulted in MSSIM = 0.2539. Increasing the FFT size to 4096 gave MSSIM = 0.9075.

4.2.3 Needle Imaging Experiment with Space-Time Reconstruction

In the case of pulse echo A-scans, time-delay profiles are generated without conversion from $\hat{g}_m[k]$. This makes it entirely possible to perform space-time reconstruction with both the stepped-FMCW and pulse echo modalities. The following experiment was conducted to compare space-time multistatic ultrasound reconstruction with a commercial phased array ultrasound system [52].

In the space-time reconstruction half of the experiment, a 25-gauge biopsy needle was placed vertically in a 2.0 cm diameter cylindrical cup filled with acoustic scanning gel. An 8-element conformal array was wrapped partially around the side of the cup for a 160°coverage. This orientation allowed the array to image the needle as if it were a point-reflector owing to its small thickness. A set of 64

multistatic pulse echo tracks were obtained for reconstruction. Fig. 4.6(a) shows space-time reconstruction which assumed an isotropic beampattern.

The needle location was clearly visible despite noticeable circular and elliptical reconstruction artifacts. Had an array with more elements been used with the addition of a binary beampattern mask, the high signal needle region would be expected to further diminish the visibility of the background artifacts.

An imaging test was performed on the same needle using a commercial ultrasound system, the Acuson 128 XP/10. The transducer used was a rigid 4.0 cm array with 128 phased elements operating at 7 MHz. Both the face of the transducer and the needle were placed in a water tank, about 1.0 cm apart. Like the conformal array setup, the needle was positioned perpendicular to the plane of the array. The imaging results are shown in Fig. 4.6(b).

Although the needle position was readily identifiable in the Acuson image, reverberation shadowing of the ultrasound waves resulted in a strip of high signal extending up to a centimeter from the expected location. These results highlight the potential for a multistatic space-time scheme to rival the imaging capability of a commercial system.

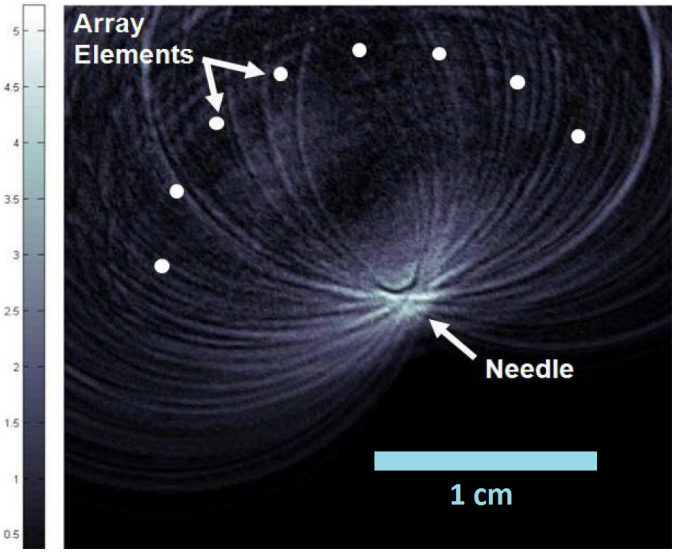

(a) Space-time reconstruction of the needle in acoustic gel. A conformal, 8-element multistatic array was used to obtain A-scans.

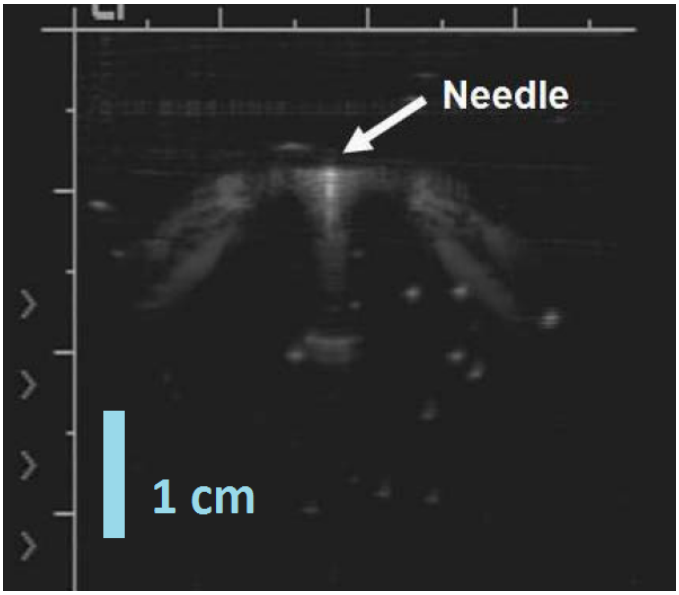

(b) Phased array imaging of the needle in water. An Acuson 128 XP/10, a commercially available imaging system, was used.

Figure 4.6: Ultrasound imaging of a 25-gauge needle.

4.2.4 Space-Time Reconstruction Simulations for Stepped-FMCW Reconfigurable Array Systems

The design and realization of a physical system is a resource-intensive process that requires first the establishment of desired imaging capability. This is highly dependent on the application even within the field of medical ultrasonography. For example, an abdominal scan requires a higher imaging depth than a thyroid scan. A major tool for designing new imaging systems is simulation software that can predict performance based on several known system specifications. Specifically, we devote our efforts to building a basic simulation technique for a stepped-FMCW system with reconfigurable arrays.

Up to this point we have established two main processes: (1) Obtaining time-delay profiles from multistatic stepped-FMCW data, and (2) Reconstructing an image from the time-delay profiles. From these concepts, a system performance simulator can be constructed. These simulation techniques serve to give a quick upper-limit estimate of $\hat{s}[\hat{i}, \hat{j}]$ given the following inputs:

1. Dimensions of the reconstruction, I and J, in pixels,

2. True length represented by each pixel, Δx_{pix},

3. Single-pixel locations in $[\hat{i}, \hat{j}]$ of all elements,

4. The angle of the face of each element, Ψ,

5. The degree of binary beamspread, Θ, on both sides of the element's normal direction,

6. Single-pixel locations in $[\hat{i}, \hat{j}]$ of all targets,

7. Frequency spacing, Δf,

8. Starting and ending frequencies (or alternatively, the number of frequency steps, K)

9. Speed of wave propagation, v.

First, the theoretical time-delay profiles are calculated for all multistatic tracks. A theoretical time-delay profile is declared as a sequence of zeros with the value 1 at bins corresponding to the round trip time delay of each target position. Each profile is then simulated as having been acquired from a stepped-FMCW system by filtering its spectrum according to the specified operating band. A windowing function may be applied as desired by the user, but has not been in this thesis.

To incorporate beamspread for each element z, its beampattern mask is first determined by calculating a matrix $\hat{A}_z[\hat{i}, \hat{j}]$ that contains the angular offset (relative to Ψ) of each pixel from the element face. The corresponding beamspread matrix $\hat{B}_z[\hat{i}, \hat{j}]$ is then defined as containing zeros but having the value 1 at the

pixel locations where $\hat{A}_z[\hat{i},\hat{j}]$ is at most Θ. In the interest of simplicity, we have chosen the binary beamspread angle as an approximation of the main beam in a full beampattern function. This means that we limit the element's illumination span to Θ on both sides of the normal direction of its face, Ψ. The same beamspread likewise dictates the maximum angular span for signal reception. (An isotropic beamspread reconstruction is accomplished by setting the $\Theta = \pi$.) Beampattern customization with additional lobes and attenuation levels may be specified by programming $\hat{B}_z[\hat{i},\hat{j}]$ to contain a range of values in the interval [0,1] for explicit value ranges of $\hat{A}_{z,\hat{i},\hat{j}}$.

The beampattern mask for a multistatic pair, $\mu_m[\hat{i},\hat{j}]$ is implemented in the simulation as described by Eq. (4.18) such that

$$\mu_{m,\hat{i},\hat{j}} = \hat{B}_{\text{trans},\hat{i},\hat{j}}\,\hat{B}_{\text{rec},\hat{i},\hat{j}}. \tag{4.24}$$

The bandlimited profiles are then reconstructed by the space-time method previously described. It is important to emphasize that in designing a stepped-FMCW simulation or system, a fundamental relationship exists between the frequency spacing, Δf, and the extent of time-delay profile axis:

$$\frac{1}{\Delta f} = \Big\{ \text{Total time delay represented on the profile axis} \Big\}. \tag{4.25}$$

To take it one step further, a working stepped-FMCW system will expect to only process time-delay profiles up to half the length of the sequence. (However, for a simulation, this is inconsequential to the results.) Since we arrive at $\hat{p}_{\mathrm{tdp},m}[n]$ via a DFT, values of $\hat{p}_{\mathrm{tdp},m}[n]$ beyond the half the DFT length signify "negative time delays" in the same way as a canonical DFT would signify negative frequency values. Therefore a stepped-FMCW system design with parameter Γ, defined as the longest *processable* round-trip propagation time delay, must satisfy

$$\Gamma \leq \frac{1}{2\Delta f}. \tag{4.26}$$

Simulation Experiment: Resolving Point Targets at Varying Locations Within the Region of Interest

To observe the effects on image resolution due to a combination of (1) angular aperture span, (2) binary beamspread, and (3) operational bandwidth, simulations were performed. The model consisted of a 13-element non-uniform, curved array operating multistatically. The beamspread, Θ, was 40°. A region of interest with dimensions $5\,\mathrm{mm} \times 5\,\mathrm{mm}$ was defined for a 250×250 image matrix.

Three sets of 36 simulated reconstructions were performed. Each set was identical except for a change in the stepped-FMCW frequency bandwidth. The three bands used were: (1) 13.0 MHz to 15.0 MHz, (2) 9.0 MHz to 15.0 MHz, and

(3) 5.0 MHz to 15.0 MHz. The frequency step size, Δf was held constant at 98.933 kHz.

Each reconstruction resolved a single set of 3 closely-spaced point targets at one of 36 locations. Relative to the chosen array configuration, these locations were selected in order to vary the aperture's span over the targets and the number of within-view elements. Fig. 4.7 shows the aperture and a complete landscape of the 36 target cluster test points. The centermost point in the three-target cluster was the reference point for determining the maximum aperture span angle, Θ_A. This is the angle formed at the target which encompasses the two in-view elements are that farthest from each other. From the discussion in Chapter 2, we would expect that increasing Θ_A and the number of in-view elements would generally improve the resolution of the target reconstruction. Fig. 4.8, Fig. 4.9, and Fig. 4.10 show samples of the reconstructions for Test Points #12 and #29.

To quantify the quality of each reconstruction, two images were compared:

1. A magnitude scaled version of the reconstruction such that the dynamic range was [0, 255].

2. An ideal image consisting of zeros except for at the designated target locations, where the values were set to 255.

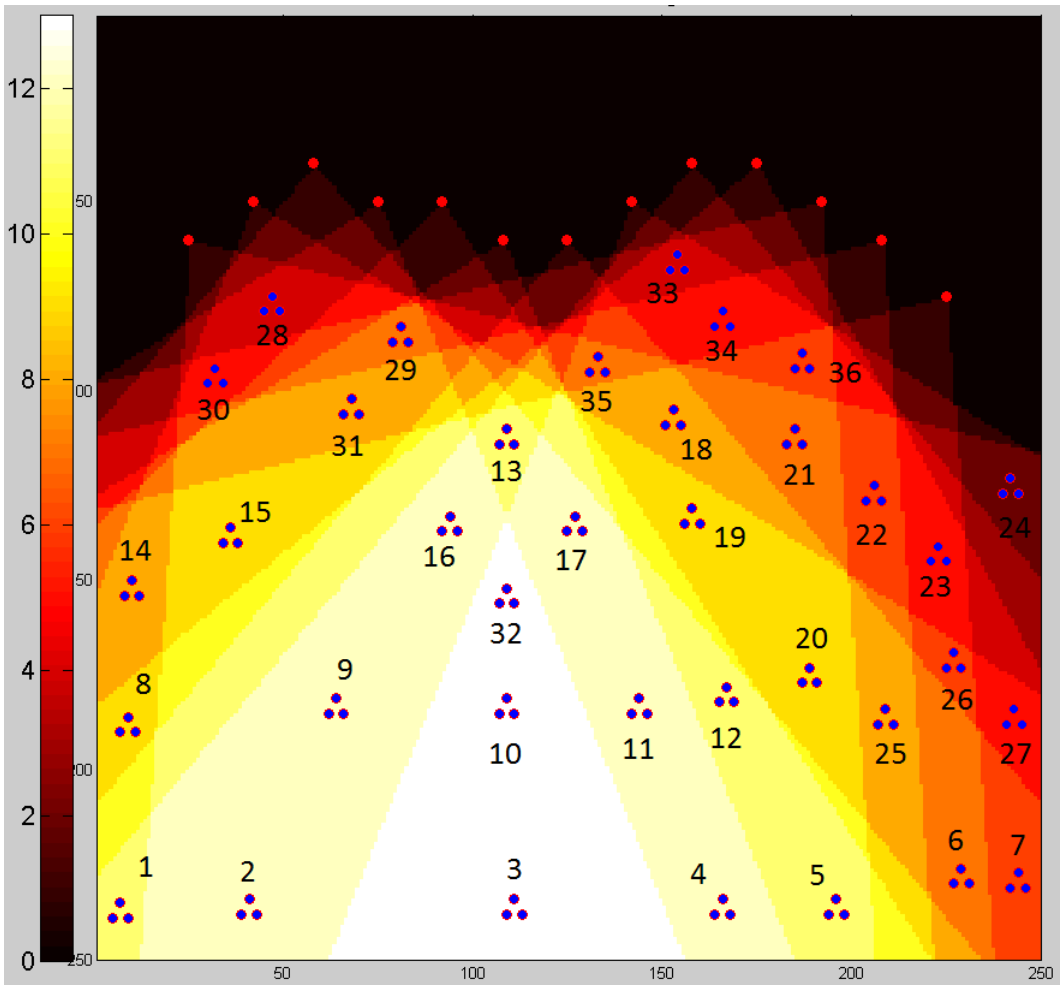

Figure 4.7: Array element arrangement (in red) with all target locations (in blue) and respective Test Point reference numbers.

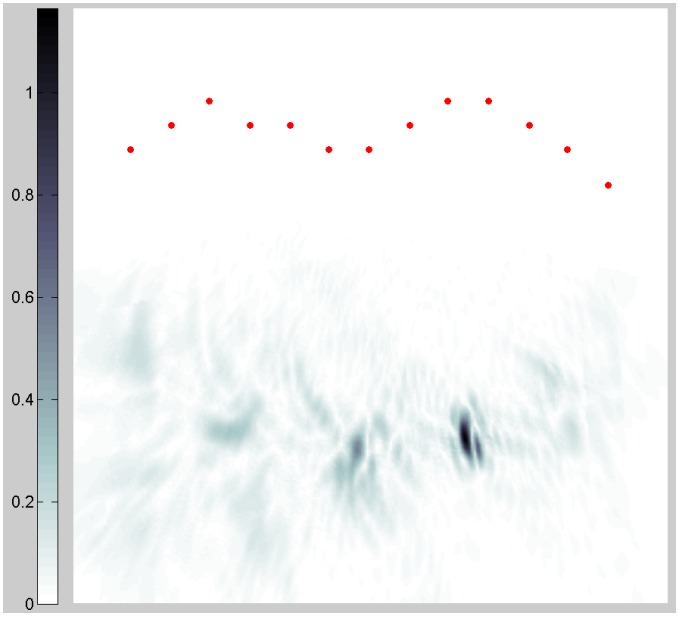

(a) Test Point #12

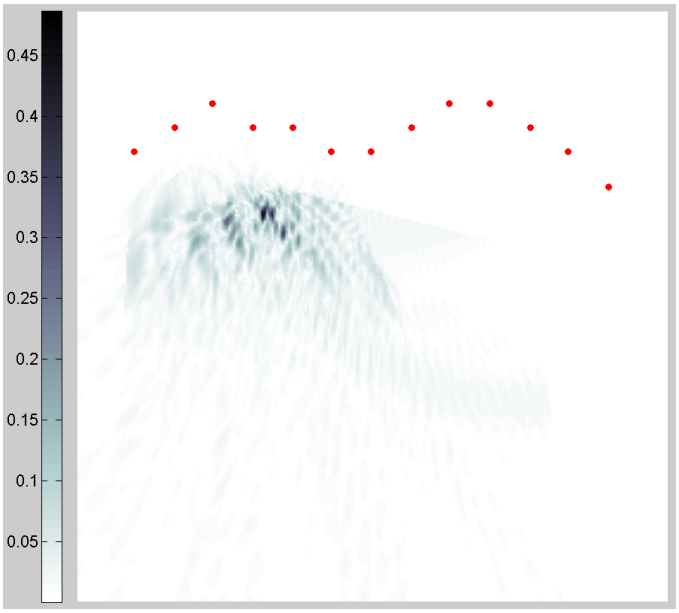

(b) Test Point #29

Figure 4.8: Reconstruction at 2 MHz operating bandwidth.

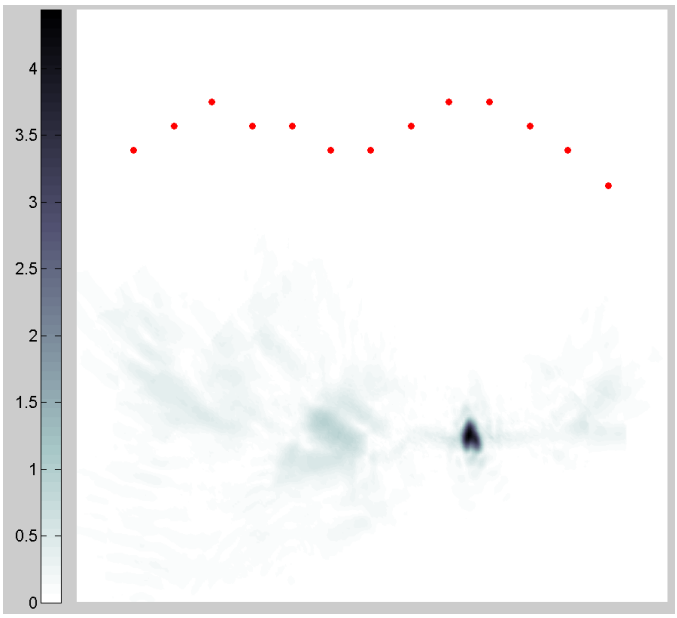

(a) Test Point #12

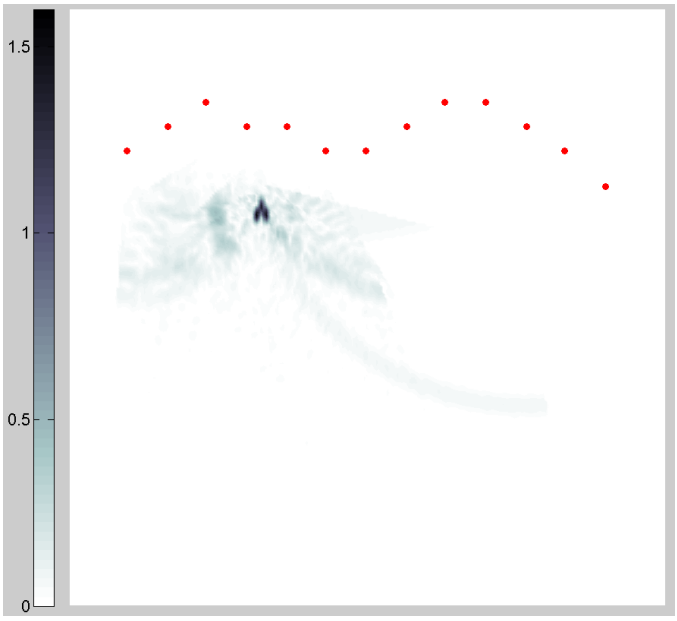

(b) Test Point #29

Figure 4.9: Reconstruction at 6 MHz operating bandwidth.

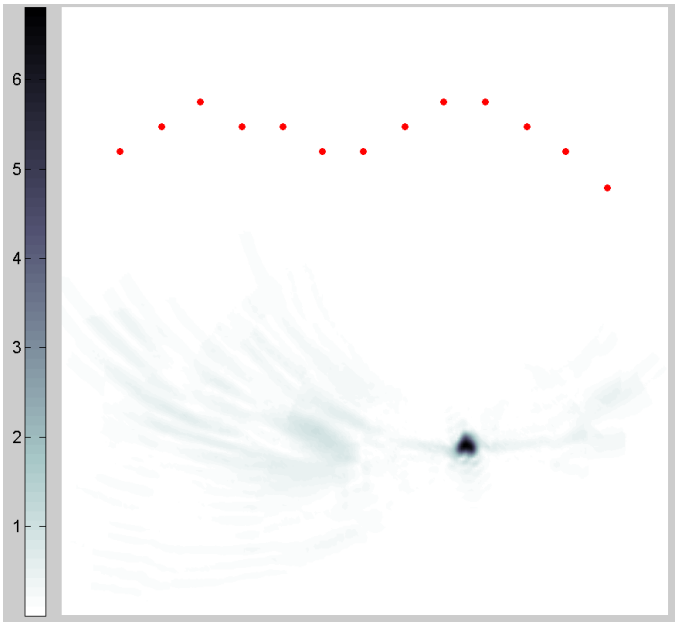

(a) Test Point #12

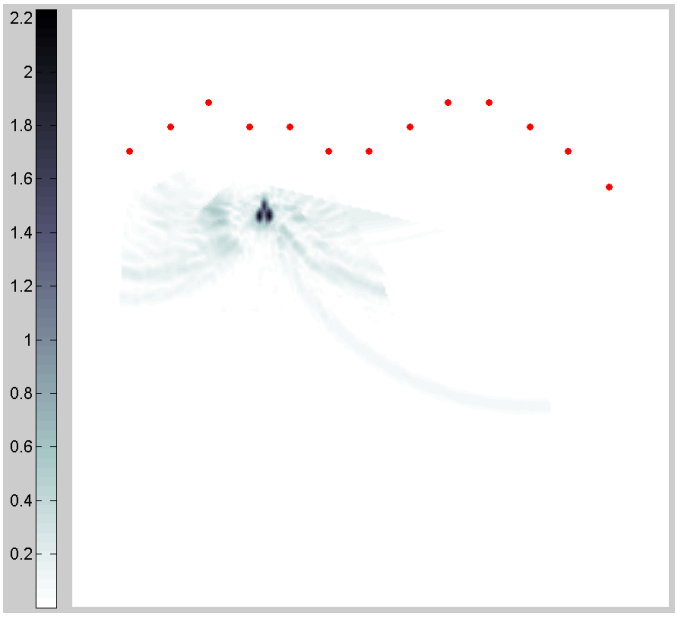

(b) Test Point #29

Figure 4.10: Reconstruction at 10 MHz operating bandwidth.

Two comparison metrics were used: mean-squared error (MSE) and mean structural similarity (MSSIM). We assume that the MSSIM is proportional to resolution achieved and the MSE, inversely proportional. The comprehensive results for each reconstruction is shown in Fig. 4.14 and Fig. 4.15. To visualize these results, each set of 36 MSE and MSSIM values were plotted on a 3D graph, as a function of the number of in-view elements and Θ_A. Fig. 4.11, Fig. 4.12, and Fig. 4.13 show the plots for the 3 frequency bandwidths. Each colored line segments represents one of the 36 target cluster locations.

The MSE decreased as the number of in-view elements increased and when Θ_A is increased. This is expected. On the other hand, the MSSIM results did not as clearly show the same trend. Some of the MSSIM results were noticeably counter-intuitive. For example, Test Point #3 had a 10 MSSIM of 0.828, and Test Point #32, 0.789. This would suggest that Test Point #32 was in less advantageous location for resolution, though the theory would predict the opposite. (Test Point #32 has a greater Θ_A with the same number of in-view elements.) However, the MSE showed the expected trend: 44.10 for #3, and 38.30 for #32.

Based on these results, it appears that the MSE metric reflects the theory of coherent imaging more closely than does MSSIM. One possible explanation for the mixed results of MSSIM is its emphasis on structure. It is plausible that a particular distribution of background artifacts could be misinterpreted as structurally

significant for the image as a whole. Because of the SSIM algorithm's internal weighting on structure, minor dissimilarities to the ideal image may give rise to unexpected cost.

Simulation runtime averaged 11.7 minutes per set of 36 reconstructions using a Samsung PC with a 2.80 GHz Intel processor and 4 GB of RAM.

4.3 Conclusion

This chapter establishes the forward propagation model for the stepped-FMCW multistatic system and from there, describes the process of back-propagating received data to reconstruct an image.

Based on the backward propagation model, we describe how the reconstructed image can be estimated by a sum of the space-time subimages by way of maximum likelihood.

In describing the reconstruction process, we highlight the equivalence of the space-time and spatial-frequency methods of implementing the theory. This is supported experimentally by using both methods to reconstruct stepped-FMCW ground-penetrating radar data and arriving at the same final image (within some margin of error).

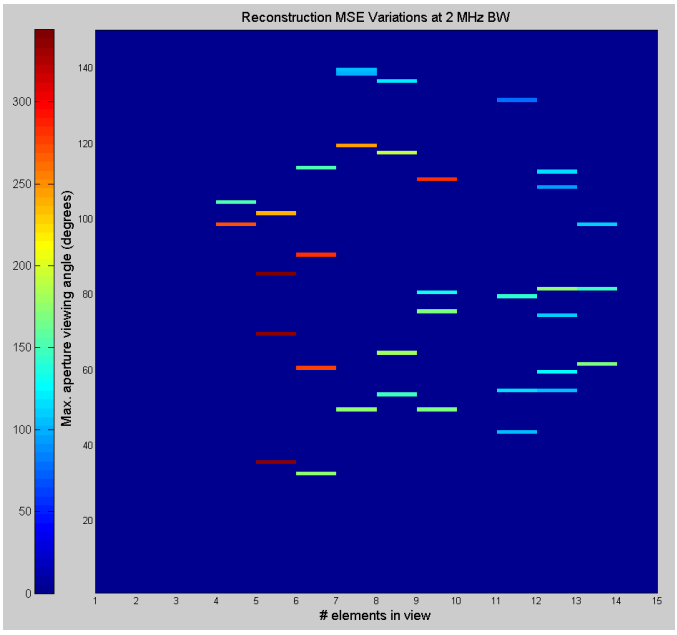

(a) Mean-squared error (MSE)

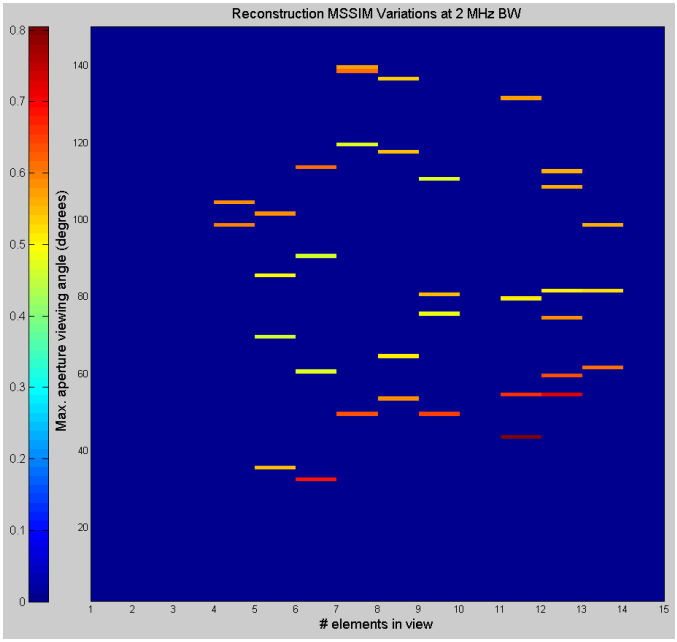

(b) Mean structural similarity (MSSIM)

Figure 4.11: Reconstruction performance at 2 MHz operating bandwidth.

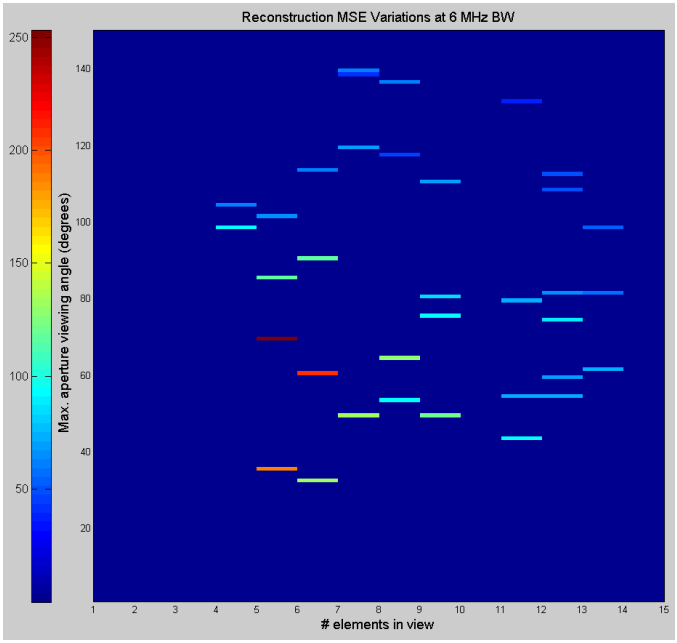

(a) Mean-squared error (MSE)

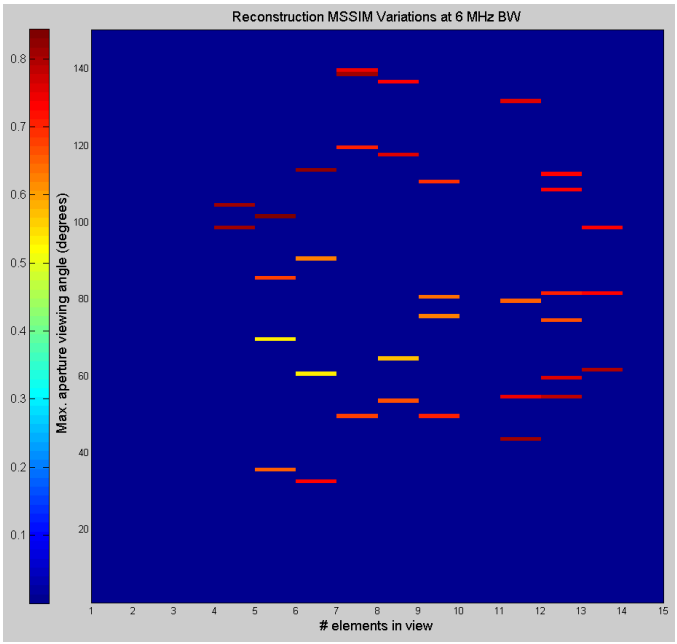

(b) Mean structural similarity (MSSIM)

Figure 4.12: Reconstruction performance at 6 MHz operating bandwidth.

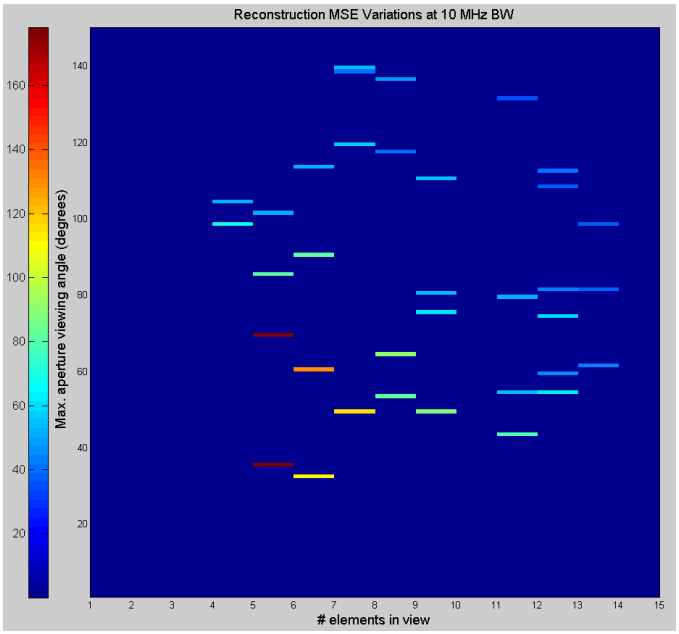

(a) Mean-squared error (MSE)

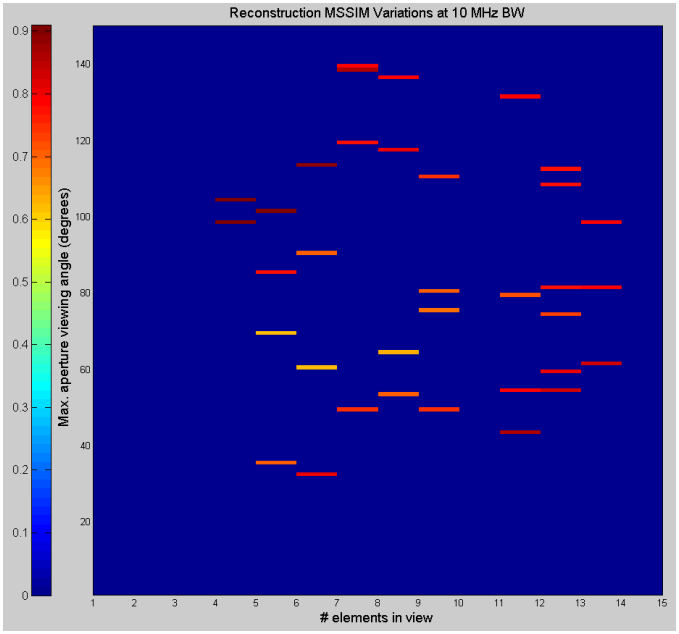

(b) Mean structural similarity (MSSIM)

Figure 4.13: Reconstruction performance at 10 MHz operating bandwidth.

Test point	# elements in view	Max. aperture viewing angle (degrees)	MSE of reconstruction		
			2 MHz BW	6 MHz BW	10 MHz BW
1	11	42.8	103.40	94.40	79.04
2	12	54.0	102.91	73.81	61.94
3	13	61.3	170.30	73.57	44.10
4	12	58.8	125.71	69.73	45.70
5	11	54.4	114.81	74.06	53.16
6	7	49.0	174.97	130.84	114.63
7	6	32.3	172.79	134.44	109.10
8	9	48.9	168.95	122.05	87.45
9	12	73.7	111.74	87.30	60.61
10	13	81.4	147.66	59.22	38.79
11	12	80.9	172.43	66.03	42.22
12	11	78.7	142.15	73.13	50.57
13	11	130.6	78.99	36.22	33.54
14	8	52.9	149.95	93.34	81.20
15	9	79.6	129.93	83.92	54.86
16	12	108.0	95.92	49.10	38.30
17	12	112.2	117.34	50.00	41.36
18	8	135.9	123.10	60.17	49.00
19	9	110.4	281.35	70.08	53.27
20	9	74.8	170.02	92.13	60.09
21	7	119.2	245.08	70.06	56.31
22	6	89.8	282.28	117.18	82.80
23	5	68.9	333.90	253.27	178.23
24	2	20.2	1427.80	494.48	330.44
25	8	63.8	181.34	130.09	90.49
26	6	60.0	274.30	206.15	130.43
27	5	35.0	338.38	189.09	175.80
28	4	98.4	271.54	91.31	67.78
29	7	138.4	99.01	43.48	39.73
30	5	85.0	344.14	117.73	82.27
31	8	116.9	192.35	47.36	41.00
32	13	97.5	108.33	52.14	38.30
33	4	104.0	153.68	62.05	51.18
34	5	101.2	241.09	64.12	50.96
35	7	139.3	103.48	60.64	54.18
36	6	112.9	153.78	59.72	50.61
		Average:	211.25	101.46	75.54

Figure 4.14: Mean-squared error (MSE) values for image reconstruction analysis.

Test point	# elements in view	Max. aperture viewing angle (degrees)	MSSIM of reconstruction		
			2 MHz BW	6 MHz BW	10 MHz BW
1	11	42.8	0.805	0.815	0.860
2	12	54.0	0.726	0.789	0.828
3	13	61.3	0.607	0.793	0.828
4	12	58.8	0.639	0.760	0.801
5	11	54.4	0.657	0.744	0.787
6	7	49.0	0.638	0.676	0.740
7	6	32.3	0.688	0.733	0.803
8	9	48.9	0.649	0.699	0.747
9	12	73.7	0.583	0.664	0.727
10	13	81.4	0.528	0.730	0.789
11	12	80.9	0.508	0.706	0.768
12	11	78.7	0.514	0.655	0.717
13	11	130.6	0.578	0.751	0.783
14	8	52.9	0.591	0.667	0.701
15	9	79.6	0.547	0.636	0.703
16	12	108.0	0.559	0.725	0.774
17	12	112.2	0.559	0.730	0.778
18	8	135.9	0.540	0.726	0.793
19	9	110.4	0.474	0.695	0.751
20	9	74.8	0.485	0.620	0.690
21	7	119.2	0.471	0.705	0.769
22	6	89.8	0.465	0.621	0.703
23	5	68.9	0.461	0.530	0.621
24	2	20.2	0.450	0.644	0.782
25	8	63.8	0.507	0.570	0.638
26	6	60.0	0.473	0.533	0.611
27	5	35.0	0.548	0.649	0.703
28	4	98.4	0.600	0.812	0.899
29	7	138.4	0.611	0.805	0.854
30	5	85.0	0.503	0.678	0.768
31	8	116.9	0.550	0.761	0.804
32	13	97.5	0.560	0.734	0.789
33	4	104.0	0.590	0.817	0.904
34	5	101.2	0.585	0.843	0.909
35	7	139.3	0.573	0.741	0.791
36	6	112.9	0.615	0.827	0.889
		Average:	0.568	0.711	0.772

Figure 4.15: Mean structural similarity (MSSIM) values for image reconstruction analysis.

The focus of the chapter then shifts to space-time reconstruction, which is most suitable for arbitrary array configurations. We explain how the multistatic time-delay profiles are mapped to form subimages, and give a visual account of how monostatic and bistatic subimages differ. The topic of structural similarity is introduced, with mean structural similarity (MSSIM) as an index for quantifying how similar two images are to the human visual system.

A laboratory experiment is described in which a space-time reconstruction of a needle was performed after acquiring pulse echo ultrasound data with an 8-element conformal array. The needle imaging result was comparable in quality to a commercial system despite some differences in operation and specifications. This experiment highlighted the combination of space-time reconstruction, multistatic operation, and ultrasonic imaging.

The final section of the chapter is devoted to imaging system simulation as a basic design resource. We describe how stepped-FMCW operation is simulated to give time-delay profiles which are then reconstructed with the space-time method. In particular, we show a simulation experiment in which a target cluster is reconstructed at various locations in order to observe the effect of aperture span angle and number of in-view elements. The analysis with mean-squared error (MSE) confirms the theory, but MSSIM is less convincing. Structural emphasis inherent in the MSSIM calculation may have amplified artifact costs beyond MSE levels.

For example, any patterned ringing in the reconstructed image arising from Gibbs phenomenon (introduced by finite FFT sums for the stepped-FMCW frequencies) may have been assigned structural significance with the MSSIM algorithm while being treated indiscriminately with MSE.

Chapter 5

Resolution Enhancement Techniques

The combination of space-time reconstruction and the stepped-FMCW modality in this project allows for additional ways to improve resolution and suppress imaging artifacts. Two methods are described in this chapter. They each involve extra steps in the reconstruction algorithm discussed previously and can be implemented independently of one another. They are: (1) Enhancement by space-time subimage variance, and (2) Enhancement by the estimation and removal of quadrature phase errors.

References [34] and [32] form the basis of this chapter.

5.1 Resolution Enhancement By Subimage Variance

Recall that the final step in forming the reconstructed space-time image, $\hat{s}[\hat{i},\hat{j}]$, requires taking the sum of subimages across all multistatic data tracks:

$$\hat{s}[\hat{i},\hat{j}] = \sum_{m} \Big\{ \mu_m[\hat{i},\hat{j}]\, \hat{s}_m[\hat{i},\hat{j}] \Big\},$$

where $\hat{s}_m[\hat{i},\hat{j}]$ is the m^{th} space-time subimage formed by mapping the m^{th} time-delay profile $\hat{p}_{\mathrm{tdp},m}[n]$ over $[\hat{i},\hat{j}]$. As before, $\mu_m[\hat{i},\hat{j}]$ is a masking function that can encapsulate a number of post-processing steps.

An important aspect of the backward propagation kernel seen in Eq. (4.2) is that at a point target location, cancellation will occur completely with that of the forward-propagating Green's function. This leaves real and positive scalars at the target locations which have magnitudes greater than those in neighboring pixels. Therefore, as we have seen, the reconstructed pixel location of a scatterer tends to sees a larger mean value for $\hat{s}_{m,\hat{i},\hat{j}}$ across m than other pixels.

An added observation is that the variance of $\hat{s}_{m,\hat{i},\hat{j}}$ across m will be lower at target locations than at non-target locations since each subimage contributes a consistently positive and real value at target locations. In the reconstruction procedure described so far, the final summing of a pixel's contributions from each

multistatic track precludes the exploitation of the contribution variance. Now we include a step in the procedure to store these values separately, and by doing so, enable the algorithm to calculate the contribution variance at each pixel:

$$\mathrm{var}[\hat{i},\hat{j}] = \frac{1}{M_o}\sum_{m_o=1}^{M_o}\left(\,\hat{s}_{m_o}[\hat{i},\hat{j}] - \mathrm{mean}\left\{\hat{s}_{m_o}[\hat{i},\hat{j}]\right\}\right)^2, \tag{5.1}$$

where M_o is the number of multistatic contributions for the pixel $[\hat{i},\hat{j}]$.

Let us now define a modified variance function with scaled and inverted pixel values such that the dynamic range is $[0, 255]$:

$$\widehat{\mathrm{var}}_{[0,255]}[\hat{i},\hat{j}] = c_o\,(\,255 - \mathrm{var}_{[0,255]}[\hat{i},\hat{j}]\,), \tag{5.2}$$

where c_o is an arbitrary, real weighting coefficient. Then, a composite reconstructed image can be defined that incorporates both the original reconstruction and variance information:

$$\hat{s}_{\mathrm{comp}}[\hat{i},\hat{j}] = \hat{s}_{[0,255]}[\hat{i},\hat{j}]\,\widehat{\mathrm{var}}_{[0,255]}[\hat{i},\hat{j}], \tag{5.3}$$

where $\hat{s}_{[0,255]}[\hat{i},\hat{j}]$ is simply the original reconstruction with dynamic range $[0, 255]$.

Low variance and high total signal are expected to be expressed at target location pixels. By inverting the variance values, a pixelwise multiplication can be done that places emphasis on these conditions in the composite image.

5.1.1 Simulation Experiment: Forming a Composite Image to Include Variance Information

Using the same platform from Chapter 4 for consistency, we again simulate stepped-FMCW space-time reconstruction in the manner depicted by Fig. 4.7. This time, we use mean-squared error (MSE) to compare the ideal target distribution to $\hat{s}_{\text{comp},[0,255]}[\hat{i},\hat{j}]$, the composite image with dynamic range [0,255]. The weighting coefficient c_o was set to 1.

A comprehensive summary of results is shown in Fig. 5.4. With respect to the MSE metric, the results were mixed and did not show consistently lower error values for the composite image set compared to the original reconstruction set in Chapter 4. Visually however, the composite images consistently showed resolution improvement near the target cluster. This is expected since the variance plots confirm sharp changes from low variance at the target locations to high variance in the neighboring pixels, with generally minimal variance farther away.

Fig. 5.1, Fig. 5.2, and Fig. 5.3 show the reconstructions, composite images, and associated variance plots for Test Points #18, #32, and #36 at 10 MHz. Note that for all three cases, the three point targets are each more identifiable in the composite image. This is despite the higher composite MSE in Test Points #18 and #36.

Overall, these results suggest that using variance information to construct a composite image may certainly improve resolution near the target area, but may do so at the expense of introducing noise farther away from. Because large sample sizes are preferred for statistical analyses, a larger number of multistatic tracks can also be expected to improve the value of this technique.

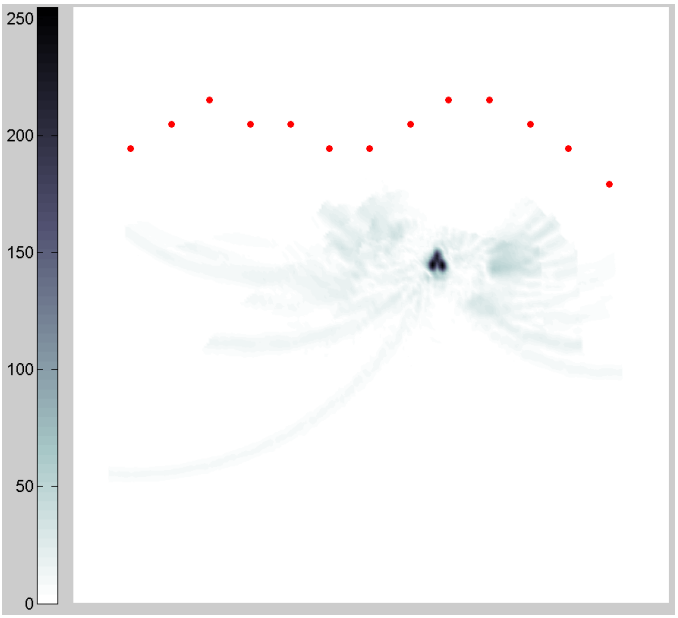

(a) Original reconstruction (MSE = 49.00).

5.2 Resolution Enhancement By Estimation and Removal of Quadrature Phase Errors

As discussed in Chapter 3, a stepped-FMCW imaging systems uses a quadrature receiver to extract phase information needed for image reconstruction. Theo-

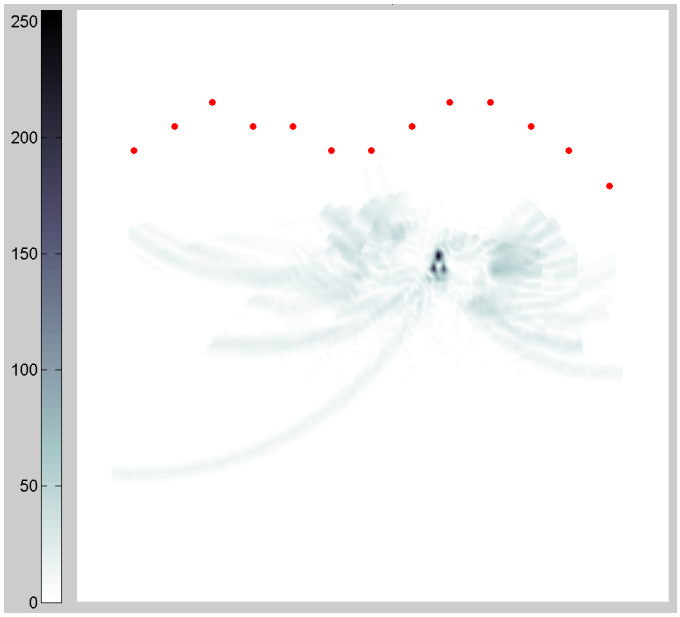

(b) Composite image (MSE = 51.38).

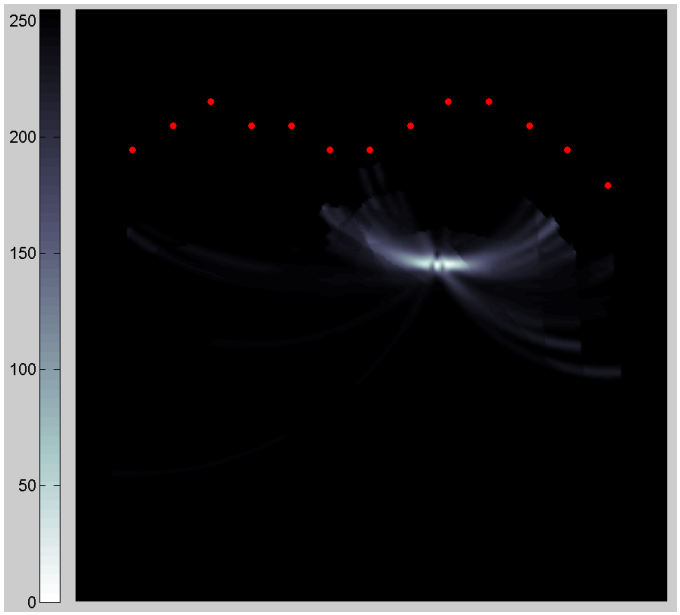

(c) Inverted variance plot (dark = low variance).

Figure 5.1: Test Point #18 at 10 MHz bandwidth.

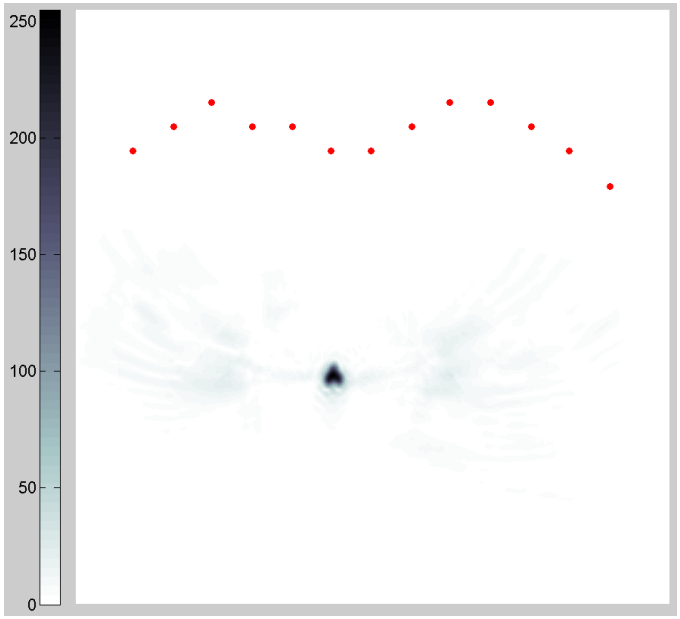

(a) Original reconstruction (MSE = 38.30).

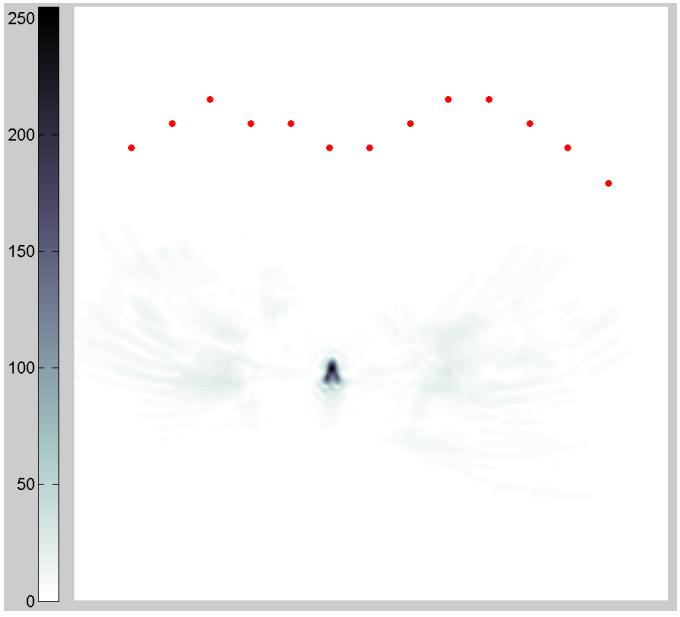

(b) Composite image (MSE = 31.18).

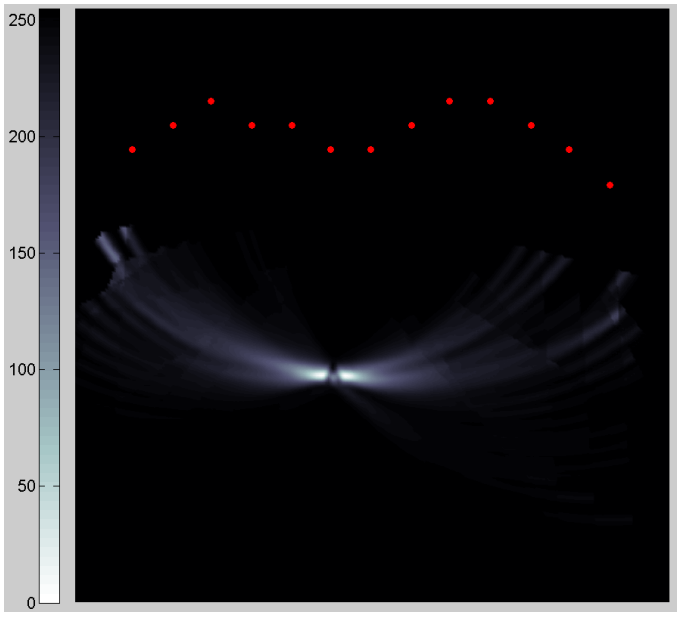

(c) Inverted variance plot (dark = low variance).

Figure 5.2: Test Point #32 at 10 MHz bandwidth.

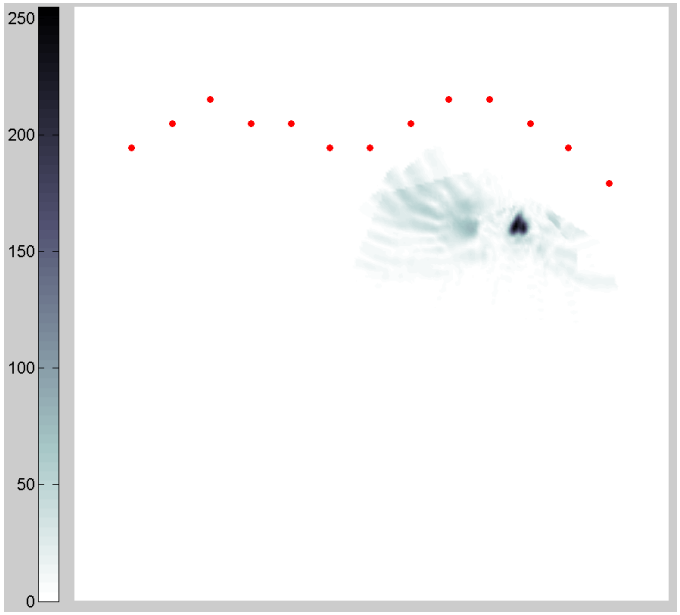

(a) Original reconstruction (MSE = 50.61).

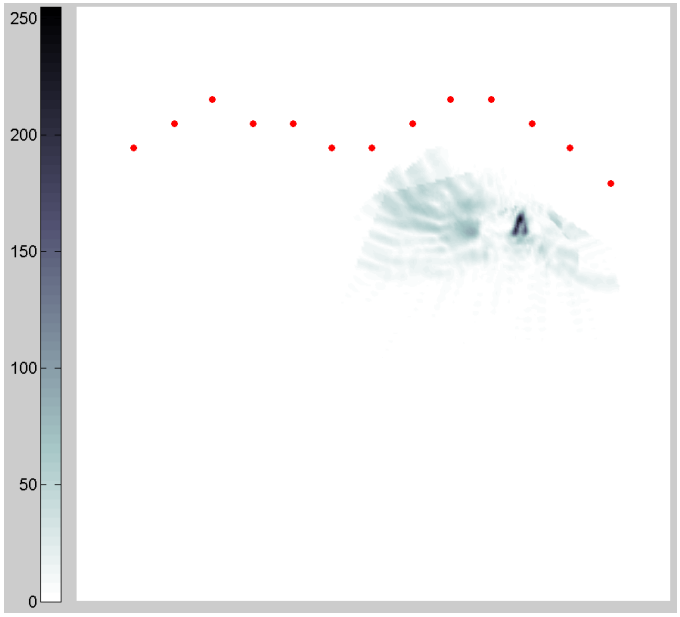

(b) Composite image (MSE = 53.55).

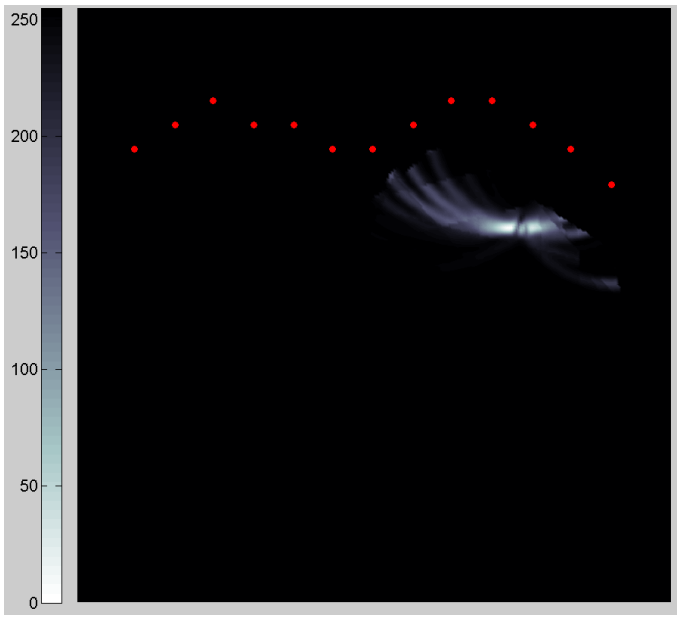

(c) Inverted variance plot (dark = low variance).

Figure 5.3: Test Point #36 at 10 MHz bandwidth.

Test point	# elements in view	Max. aperture viewing angle (degrees)	MSE of reconstruction (using variance)		
			2 MHz BW	6 MHz BW	10 MHz BW
1	11	42.8	80.22	66.56	51.10
2	12	54.0	86.72	63.60	53.40
3	13	61.3	253.43	64.57	36.22
4	12	58.8	140.25	58.35	38.34
5	11	54.4	117.68	61.46	47.25
6	7	49.0	171.38	128.04	110.52
7	6	32.3	144.33	113.50	83.36
8	9	48.9	147.89	114.00	87.08
9	12	73.7	100.16	75.37	54.57
10	13	81.4	315.37	51.42	32.95
11	12	80.9	487.19	59.45	38.05
12	11	78.7	229.06	77.43	49.22
13	11	130.6	213.98	42.09	37.31
14	8	52.9	144.59	97.30	83.65
15	9	79.6	163.16	106.30	75.49
16	12	108.0	176.86	46.19	35.31
17	12	112.2	350.81	43.87	31.59
18	8	135.9	304.71	93.11	51.38
19	9	110.4	545.91	91.95	58.68
20	9	74.8	269.28	98.54	69.33
21	7	119.2	389.40	96.39	67.86
22	6	89.8	499.79	169.73	103.99
23	5	68.9	398.92	345.84	252.73
24	2	20.2	1359.65	467.89	318.75
25	8	63.8	196.73	132.95	95.34
26	6	60.0	317.39	263.80	171.30
27	5	35.0	341.83	208.30	187.11
28	4	98.4	266.66	92.21	63.20
29	7	138.4	198.18	74.22	54.91
30	5	85.0	603.71	173.72	113.71
31	8	116.9	578.28	74.46	52.71
32	13	97.5	219.36	43.39	31.18
33	4	104.0	191.07	82.23	56.95
34	5	101.2	332.82	67.12	48.56
35	7	139.3	140.06	142.76	72.55
36	6	112.9	239.18	76.80	53.55
		Average:	297.667	112.915	79.700

Figure 5.4: Mean-squared error (MSE) values for image reconstruction analysis of composite image with pixel variance information.

retically, the coherent orthogonal reference waveforms of the quadrature receivers are maintained at a constant 90°offset during data acquisition. In practice, the electronic component responsible for creating an orthogonal sine waveform from a cosine reference waveform is susceptible to phase errors due to clock drift and synchronization limitations. With the presence of such phase errors, the resulting time-delay profiles are degraded.

From the commonality of the single-sideband (SSB) contents of the separate I and Q data sequence channels, a procedure is presented for the estimation and correction of the phase offset errors which arise from the quadrature receivers. Successful removal of these errors in time-delay profiles can be expected to sharpen target reflector peaks and diminish extraneous lobes, thereby improving image resolution during reconstruction.

Recall that the k^{th} demodulated and low-passed I and Q channels can be expressed as:

$$I_k = \frac{A_k E_k^2}{2} \cos(\phi_k) \tag{5.4a}$$

$$Q_k = -\frac{A_k E_k^2}{2} \sin(\phi_k). \tag{5.4b}$$

which results in the data sequence

$$e_{\text{demod}}[k] = I_k - jQ_k = \frac{A_k E_k^2}{2} \exp(j\phi_k). \tag{5.5}$$

5.2.1 Quadrature Receiver Phase Error

As a result of hardware limitations in maintaining a 90°offset, a phase error $\Delta\phi_k$ is introduced to the reference signals used for demodulation:

$$\hat{r}_{\text{I},k}(t) = E_k \cos\left(2\pi f_k t + \frac{\Delta\phi_k}{2}\right) \tag{5.6a}$$

$$\hat{r}_{\text{Q},k}(t) = E_k \sin\left(2\pi f_k t - \frac{\Delta\phi_k}{2}\right). \tag{5.6b}$$

To analyze the effect of the phase error, $\Delta\phi_k$ is assumed to be evenly distributed between the pair of reference signals. However, this does not imply a loss of generality because it is the *relative* angular offset that is the operative parameter, and it can be shown that uneven phase error distributions does not effect the estimation and correction process.

Demodulation by mixing the reference signals with the received waveform, $x_{\mathrm{rec},k}(t) = A_k E_k \cos(2\pi f_k t + \phi_k)$, gives:

$$\begin{aligned}
\hat{m}_{\mathrm{I},k}(t) &= x_{\mathrm{rec},k}(t)\, \hat{r}_{\mathrm{I},k}(t) && \text{(5.7a)}\\
&= A_k E_k \cos\left(2\pi f_k t + \phi_k\right)\, E_k \cos\left(2\pi f_k t + \frac{\Delta\phi_k}{2}\right)\\
&= \frac{A_k E_k^2}{2} \cos\left(4\pi f_k t + \phi_k + \frac{\Delta\phi_k}{2}\right) + \frac{A_k E_k^2}{2} \cos\left(\phi_k - \frac{\Delta\phi_k}{2}\right)\\
\hat{m}_{\mathrm{Q},k}(t) &= x_{\mathrm{rec},k}(t)\, \hat{r}_{\mathrm{Q},k}(t) && \text{(5.7b)}\\
&= A_k E_k \cos\left(2\pi f_k t + \phi_k\right)\, E_k \sin\left(2\pi f_k t - \frac{\Delta\phi_k}{2}\right)\\
&= \frac{A_k E_k^2}{2} \sin\left(4\pi f_k t + \phi_k - \frac{\Delta\phi_k}{2}\right) - \frac{A_k E_k^2}{2} \sin\left(\phi_k + \frac{\Delta\phi_k}{2}\right).
\end{aligned}$$

After low-passing, the corrupted quadrature outputs become:

$$\hat{I}_k = \frac{A_k E_k^2}{2} \cos\left(\phi_k - \frac{\Delta\phi_k}{2}\right) \quad \text{(5.8a)}$$

$$\hat{Q}_k = -\frac{A_k E_k^2}{2} \sin\left(\phi_k + \frac{\Delta\phi_k}{2}\right). \quad \text{(5.8b)}$$

The corrupted complex frequency data can then be expressed as:

$$
\begin{aligned}
\hat{e}_{\text{demod}}[k] &= \hat{I}_k - j\hat{Q}_k \\
&= \frac{A_k E_k^2}{2} \cos\left(\phi_k - \frac{\Delta\phi_k}{2}\right) + j\,\frac{A_k E_k^2}{2} \sin\left(\phi_k + \frac{\Delta\phi_k}{2}\right) \\
&= \frac{A_k E_k^2}{4} \left\{\exp\left(j\,\left(\phi_k - \frac{\Delta\phi_k}{2}\right)\right) + \exp\left(-j\,\left(\phi_k - \frac{\Delta\phi_k}{2}\right)\right)\right\} \\
&\quad + \frac{A_k E_k^2}{4} \left\{\exp\left(j\,\left(\phi_k + \frac{\Delta\phi_k}{2}\right)\right) - \exp\left(-j\,\left(\phi_k + \frac{\Delta\phi_k}{2}\right)\right)\right\} \\
&= \frac{A_k E_k^2}{4} \exp\left(j\phi_k\right) \left\{\exp\left(j\frac{\Delta\phi_k}{2}\right) + \exp\left(-j\frac{\Delta\phi_k}{2}\right)\right\} \\
&\quad + \frac{A_k E_k^2}{4} \exp\left(-j\phi_k\right) \left\{\exp\left(j\frac{\Delta\phi_k}{2}\right) - \exp\left(-j\frac{\Delta\phi_k}{2}\right)\right\} \\
&= \frac{A_k E_k^2}{2} \exp\left(j\phi_k\right) \cos\left(\frac{\Delta\phi_k}{2}\right) + j\frac{A_k E_k^2}{2} \exp\left(-j\phi_k\right) \sin\left(\frac{\Delta\phi_k}{2}\right) \\
&= \cos\left(\frac{\Delta\phi_k}{2}\right)\, e_{\text{demod}}[k] + j \sin\left(\frac{\Delta\phi_k}{2}\right)\, e^*_{\text{demod}}[k].
\end{aligned}
\tag{5.9}
$$

Due to the phase error $\Delta\phi_k$, the received stepped-FMCW data now has two terms instead of one. The first term is the original sequence without error, $e_{\text{demod}}[k]$ modulated by a degradation factor $\cos\left(\frac{\Delta\phi_k}{2}\right)$. The second term is the conjugate of $e_{\text{demod}}[k]$ modulated by $\sin\left(\frac{\Delta\phi_k}{2}\right)$.

5.2.2 Phase Error Estimation

The unwanted modulation factor $\cos\left(\frac{\Delta\phi_k}{2}\right)$ in the first term, $\cos\left(\frac{\Delta\phi_k}{2}\right)\ e_{\text{demod}}[k]$, degrades the first half of the time-delay profile corresponding to the "positive time" interval. On the other hand, the added term with $e^*_{\text{demod}}[k]$ superimposes onto the range profile a time-reversed version of the conjugated time-delay profile. So unlike the first term, the second term, $\sin\left(\frac{\Delta\phi_k}{2}\right)\ e^*_{\text{demod}}[k]$ produces an artifact in the "negative-time" region of the time-delay profile though for small phase errors, the magnitude of $\sin\left(\frac{\Delta\phi_k}{2}\right)$ is small. Since a time-delay profile in a practical imaging system will only see meaningful peaks in the first half of the time-delay profile (i.e. in the "positive-time" range), the effect of term $\sin\left(\frac{\Delta\phi_k}{2}\right)\ e^*_{\text{demod}}[k]$ may be readily observable, manifested by mirrored peaks in the latter half.

Recall Eq. (5.8) and note that a simple expansion gives:

$$\hat{I}_k = \frac{A_k E_k^2}{2}\cos\left(\phi_k - \frac{\Delta\phi_k}{2}\right) \tag{5.10a}$$

$$= \frac{A_k E_k^2}{4}\exp(\,j\phi_k\,)\exp\left(-j\frac{\Delta\phi_k}{2}\right) + \frac{A_k E_k^2}{4}\exp(\,-j\phi_k\,)\exp\left(j\frac{\Delta\phi_k}{2}\right)$$

$$\hat{Q}_k = -\frac{A_k E_k^2}{2}\sin\left(\phi_k + \frac{\Delta\phi_k}{2}\right) \tag{5.10b}$$

$$= -\frac{A_k E_k^2}{4j}\exp(\,j\phi_k\,)\exp\left(j\frac{\Delta\phi_k}{2}\right) + \frac{A_k E_k^2}{4j}\exp(\,-j\phi_k\,)\exp\left(-j\frac{\Delta\phi_k}{2}\right).$$

We can now extract the single-sideband components of $\hat{I}_k$ and $\hat{Q}_k$, corresponding to the positive-time portion of the time-delay profiles:

$$\hat{I}_{k,\mathrm{SSB}} = \frac{A_k E_k^2}{4} \exp(\, j\phi_k \,) \exp\left(-j\frac{\Delta\phi_k}{2} \right) \tag{5.11a}$$

$$\hat{Q}_{k,\mathrm{SSB}} = -\frac{A_k E_k^2}{4j} \exp(\, j\phi_k \,) \exp\left(j\frac{\Delta\phi_k}{2} \right), \tag{5.11b}$$

which can both be approximated by half-band filtering the original signals $\hat{I}_k$ and $\hat{Q}_k$.

The phase error can then be estimated from the ratio of the the SSB components:

$$-\frac{\hat{Q}_{k,\mathrm{SSB}}}{\hat{I}_{k,\mathrm{SSB}}} = \exp(\, j\Delta\phi_k \,). \tag{5.12}$$

5.2.3 Phase Error Correction

Yet another way to rewrite Eq. (5.10) is in the following form:

$$\begin{aligned}\hat{I}_k &= \frac{A_k E_k^2}{2}\cos\left(\phi_k - \frac{\Delta\phi_k}{2}\right) \qquad (5.13a)\\ &= \frac{A_k E_k^2}{2}\cos(\phi_k)\cos\left(\frac{\Delta\phi_k}{2}\right) + \frac{A_k E_k^2}{2}\sin(\phi_k)\sin\left(\frac{\Delta\phi_k}{2}\right)\\ &= I_k\cos\left(\frac{\Delta\phi_k}{2}\right) - Q_k\sin\left(\frac{\Delta\phi_k}{2}\right)\\ \hat{Q}_k &= -\frac{A_k E_k^2}{2}\sin\left(\phi_k + \frac{\Delta\phi_k}{2}\right) \qquad (5.13b)\\ &= -\frac{A_k E_k^2}{2}\cos(\phi_k)\sin\left(\frac{\Delta\phi_k}{2}\right) - \frac{A_k E_k^2}{2}\sin(\phi_k)\cos\left(\frac{\Delta\phi_k}{2}\right)\\ &= -I_k\sin\left(\frac{\Delta\phi_k}{2}\right) + Q_k\cos\left(\frac{\Delta\phi_k}{2}\right).\end{aligned}$$

More succinctly, the relationship can be written in matrix form:

$$\begin{bmatrix}\hat{I}_k\\ \hat{Q}_k\end{bmatrix} = \begin{bmatrix}\cos\left(\frac{\Delta\phi_k}{2}\right) & -\sin\left(\frac{\Delta\phi_k}{2}\right)\\ -\sin\left(\frac{\Delta\phi_k}{2}\right) & \cos\left(\frac{\Delta\phi_k}{2}\right)\end{bmatrix}\begin{bmatrix}I_k\\ Q_k\end{bmatrix}. \qquad (5.14)$$

The phase error correction can then be achieved by a 2×2 matrix multiplication that inverts the effect of $\Delta\phi_k$:

$$\begin{bmatrix}I_k\\ Q_k\end{bmatrix} = \frac{1}{\cos(\Delta\phi_k)}\begin{bmatrix}\cos\left(\frac{\Delta\phi_k}{2}\right) & \sin\left(\frac{\Delta\phi_k}{2}\right)\\ \sin\left(\frac{\Delta\phi_k}{2}\right) & \cos\left(\frac{\Delta\phi_k}{2}\right)\end{bmatrix}\begin{bmatrix}\hat{I}_k\\ \hat{Q}_k\end{bmatrix}. \qquad (5.15)$$

For each stepped frequency, the process is performed once to estimate the non-corrupted data values, I_k and Q_k. Because of additive noise from the data acquisition process, the ratio in Eq. (5.12) may not give the desired phase-only result. In such situations, this error estimation and corrections procedure can be performed iteratively until values in the negative-time bins of the time-delay profile are stabilized.

5.2.4 Simulation Experiment I: Removing the Effects of Additive Receiver Noise in Time-Delay Profiles

A simulation was performed to observe the effects of phase errors as well as the described correction procedure. A time-delay profile was created to represent a single multistatic track associated with two point scatterers. The profile was a bandlimited, 1024-point sequence with two target peaks at $n = 200$ and $n = 300$. Fig 5.5(a) shows the time-delay profile without quadrature phase errors.

Random phase noise was then added to the profile's spectrum at each frequency bin within the operating stepped-FMCW band. This simulates the mismatched, non-orthogonal of the axes of the I_k and Q_k channels. The phase errors were programmed on a normal distribution with a mean of 15° and a standard deviation of 5° . Note the appearance of mirrored peaks in the negative-time portion of the time-delay profile in Fig. 5.5(b).

The phase error estimation process was achieved by first finding the SSB components of the noisy I/Q channels across all within-band frequencies. The pointwise ratio between the channels revealed a noise estimate $\Delta\phi_k$. A 2×2 correction matrix multiplication was performed at each frequency, and each resulting value gave the new I/Q channel values used to form the corrected time-delay profile seen in Fig. 5.5(c). After one iteration, the mirrored peaks have been suppressed considerably, and the peaks in the positive-time half of the profile increased in magnitude, as highlighted by Fig. 5.5(d). Since these peaks represent true target reflections, improving their prominence is critical for image quality during the space-time mapping process and subimage superimposition.

5.2.5 Simulation Experiment II: Removing the Effects of Additive Receiver Noise in Reconstructed Images

Expanding on the prior experiment, image reconstructions were performed to observe the degree to which full images are affected by both the errors and subsequent correction procedure. Test Point # 17 (in reference to the simulation environment discussed in Chapter 4) was tested with an operating bandwidth of 10 MHz. Two trials were performed with normally distributed phase errors: (1) with a mean of 15° and a standard deviation of 5° , and (2) with a mean of 20° and a standard deviation of 10° .

For each trial, two images (with error and after correction) were compared to the ideal three-pixel target image. Visually, the two images from either trial were not noticeably different from the original reconstructions, as is evident in Fig. 5.6. However, the MSE and MSSIM values indicate that the addition of phase errors does, as expected, result in an image that is less similar to the ideal than the original reconstruction. After applying the correction process, the resulting values indicate a shift back towards the ideal image. These values are given in Table 5.1. Despite the relatively minute variations in MSSIM and MSE values in this simulation, the results agree with the hypothesis that applying quadrature phase error correction is beneficial to the reconstruction process.

Table 5.1: Comparison of Test Point #17 Image Reconstructions

	MSSIM	**MSE**
Original	0.7780	41.3593
Trial 1		
With error	0.7753	41.4237
After correction	0.7753	41.3867
Trial 2		
With error	0.7703	41.4745
After correction	0.7708	41.4088

5.3 Conclusion

This chapter describes two methods for increasing target resolution. Both can be included in the reconstruction algorithm as intermediate steps.

The subimage variance technique exploits assumptions in the backward propagation theory. Simulations showed clear improvements in target resolution over the reconstruction simulations described in Chapter 4. Although for some test points the mean-squared error (MSE) was increased in the post-enhancement reconstructions, visual accounts confirmed improved target visibility. The variance plots show favorable contrast at the target cluster but since the majority of the image is low variance, erroneous boosts to pixel values elsewhere can result when forming the composite image. Depending on the exact target and array configuration, this noise may increase the overall image MSE more than the decrease afforded near the target region. Despite this, the results motivate future system designers to include this method in the reconstruction algorithm, especially when a localized target region is under scrutiny. The additional required memory and computation time is minimal, and it may be well worth the cost to run both the enhanced reconstruction with the original for comparison. Other statistical measures such as higher order moments can also be investigated for similar purposes.

The second resolution enhancement technique is used to rectify quadrature receiver errors which arise in the implementation of the imaging system. To show the effects of the errors and its correction, we focus on the time-delay profile itself. We first describe how these errors cause mirroring of the target peaks in the negative-time portion of the profile. More importantly however, the errors degrade

the true peaks in the positive-time portion. By simulating these errors and their subsequent removal, we showed that the mirrored peaks reduced in magnitude in the corrected time-delay profile while the true target peaks grew. Since the prevalence of target peaks in a time-delay profile translates to prevalence of the targets in a space-time reconstructed image, this technique would improve the resolution of the imaging system. Decreases in overall image MSE were observed in image simulations after the phase error correction process was applied to each multistatic track.

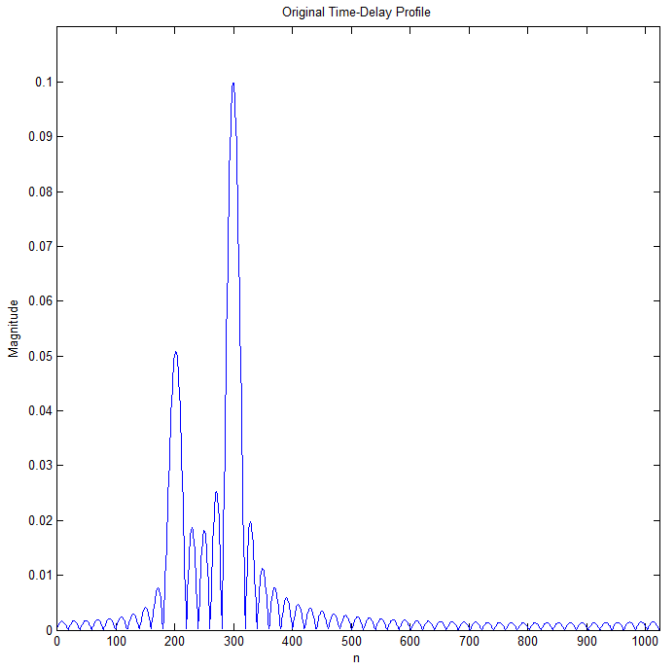

(a) Original time-delay profile without quadrature phase error. Target peaks are located at bins $n = 200$ and $n = 300$.

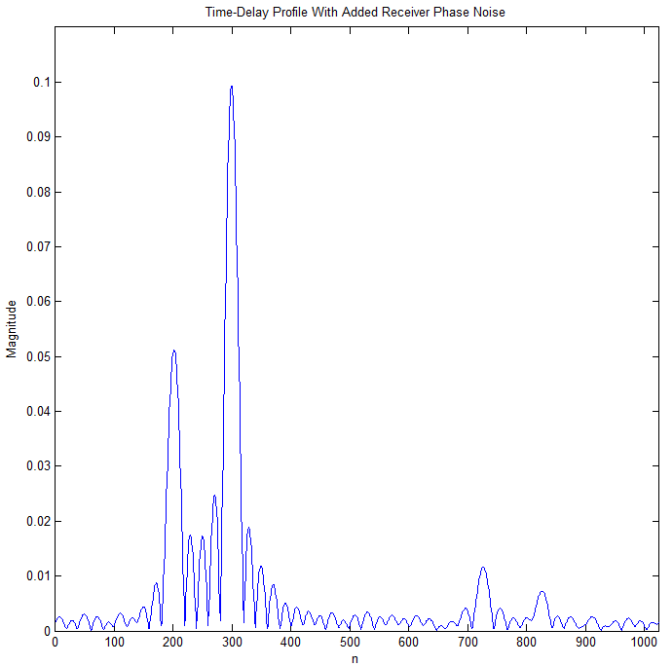

(b) Time-delay profile with added receiver phase noise. Mirrored peaks are seen at bins $n = 823$ and $n = 723$, both in the negative-time half.

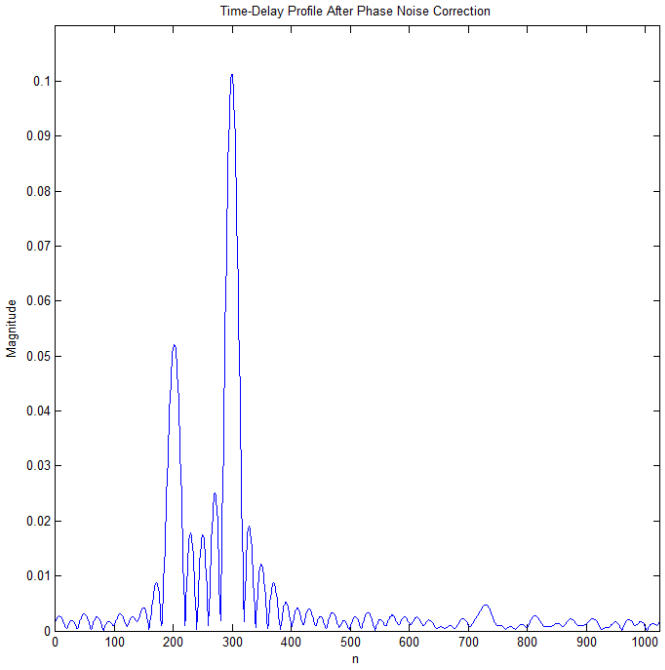

(c) Corrected time-delay profile.

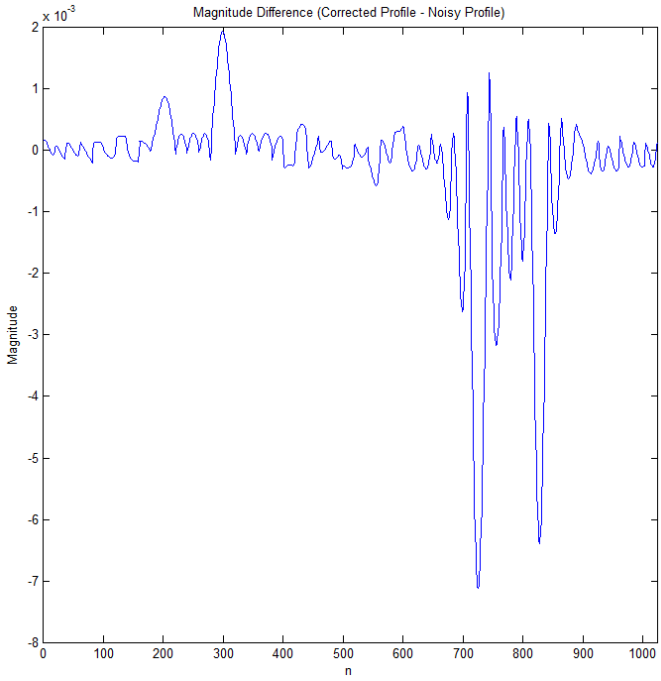

(d) Magnitude plot of the corrected profile after subtraction of noisy profile. Mirrored peaks decreased in magnitude while target peaks increased in magnitude.

Figure 5.5: Correction of quadrature receiver phase error in time-delay profiles.

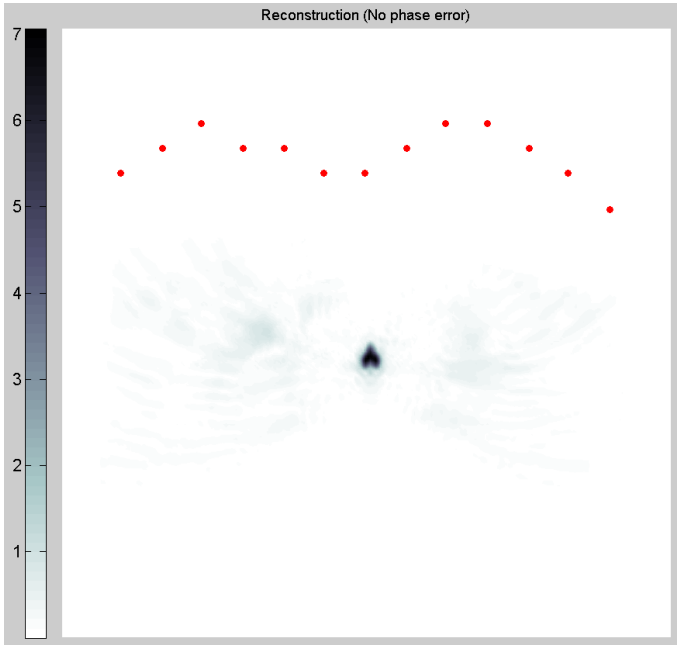

(a) Original reconstruction.

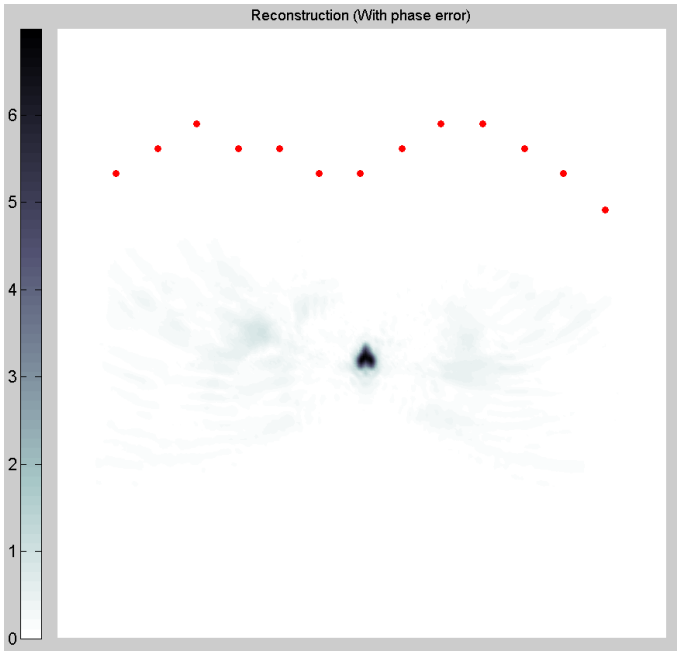

(b) Reconstruction with quadrature phase error.

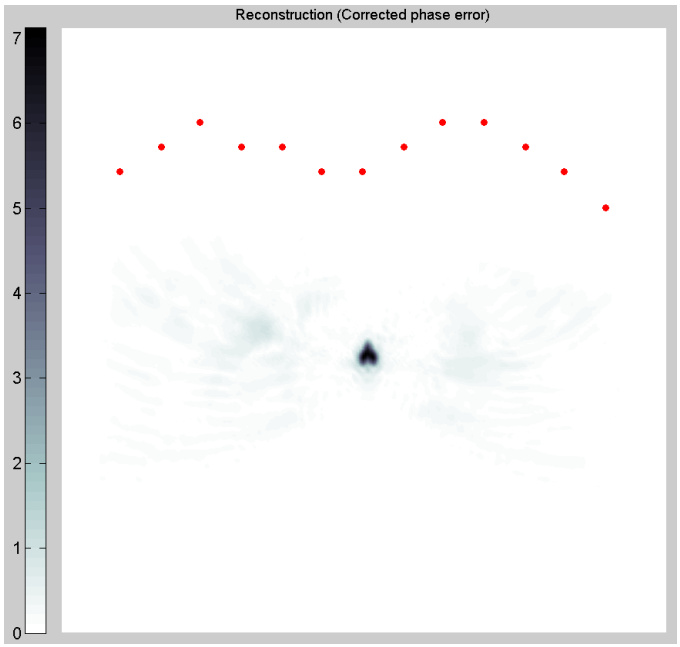

(c) Reconstruction after applying phase error correction procedure.

Figure 5.6: Trial 1 of simulated 10 MHz bandwidth reconstruction of Test Point #17 showed no noticeable visual differences between the original, with phase error, and corrected phase error images.

Chapter 6

Conclusion and Outlook

This thesis presents four primary contributions toward the goal of developing a stepped-FMCW ultrasound system for imaging with reconfigurable arrays:

1. A space-time, multistatic image reconstruction algorithm for the system that addresses the challenges involved with using a large, reconfigurable array. Increasing array size and number of elements provides an ultrasound imaging system with more data and improved resolution. The conventional phased array modality has limited scalability for handling such arrays due to hardware constraints. Instead, we propose a stepped-FMCW modality which allows for arrays to be controlled through a simple multistatic switching while providing lower noise and power output than the traditional pulse echo operation. The foundation of the reconstruction algorithm is coherent backward propagation, which can be formulated into two distinct methods: (1) Space-time reconstruction, and (2) Spatial-frequency reconstruction. Space-time reconstruction becomes the focus of

this thesis because of its ability to accommodate the arbitrary relative positioning of array elements that is characteristic of conformal, reconfigurable ultrasound arrays. We present laboratory experiments that demonstrate the feasibility of stepped-FMCW ranging in an ultrasonic environment, as well as experiments showing the feasibility of space-time image reconstruction using a flexible ultrasound array. In doing so, we have successfully tested four key aspects of an ultrasound imaging system: (1) stepped-FMCW operation, (2) multistatic data acquisition, and (3) space-time reconstruction, and (4) reconfigurable arrays.

2. A simulation method for predicting imaging system performance. With the development of the new imaging system comes the challenge of estimating system performance given a set of basic operating parameters. We present a quick method of simulating full system operation to obtain a best-case result given a stepped-FMCW operating band, and target and element distributions. Imaging results from this simulation method confirmed that (1) large bandwidth, (2) large aperture span angle, and a (3) large number of in-view elements all contributed to lower mean-squared error (MSE) from the ideal reconstruction. Quantifying performance using the mean structural similarity (MSSIM) index instead of MSE did not express the trends as clearly, which may be insightful for future developers engaging in similar analyses.

3. A method for improving image resolution using the variance of multistatic contributions. In the core reconstruction algorithm, pixel locations of targets are distinguished from non-target locations by virtue of its greater magnitude resulting from the sum of multistatic contributions. But implicit in the backward propagation theory is that target pixel contributions are also more *consistently* real and positive than other pixels. In other words, contributions to target location pixels are expected to vary less than those for neighboring non-target pixels. This allows the pixelwise variance of all multistatic values to be used as an additional measure of confidence for target presence. We present a method for creating a composite image that combines variance information with the original reconstruction. Simulation results show that clustered point-targets are more easily identified in the composite image. Increased MSE in some reconstruction trials imply that increased target region resolution may come at the expense of added noise elsewhere in the image. The overall visual enhancement may easily offset the cost, and future researchers may find this method even more beneficial when handling large numbers of array elements.

4. A method for improving image resolution by quantifying and correcting quadrature receiver phase error in time-delay profiles. Quadrature receiver phase error is introduced to stepped-FMCW data when the data acquisition hardware is unable to maintain orthogonality between the two sinu-

soidal signals in the demodulation process. This leads to I_k and Q_k values that no longer correctly give the received signal's projection onto orthogonal axes. When the corrupted I_k and Q_k data is transformed to a time-delay profile, the true target peaks are attenuated and mirrored peaks emerge in the negative-time half of the sequence. We present a method which estimates the phase error for each frequency and then removes then by a simple 2×2 matrix multiplication. Simulation results with added random I_k and Q_k phase noise showed the expected effects, and corrected data values gave a time-delay profile with increased true target peak magnitudes and diminished artifact peaks. By mitigating the effects of an error source arising from the physical implementation of the imaging system, time-delay profiles better express target peaks, increasing image resolution. This is in contrast to variance method, which improves resolution by incorporating previously unused information.

6.1 Future Paths For Research

Although the concept of a large, conformal array provides the motivation for this imaging thesis, the technical contributions presented can see relevance in a wide range of applications in medical imaging and beyond. Fig. 6.1 [8] and Fig. 6.2 [9] show prototyped arrays configurations alongside preliminary imaging

simulations which demonstrate the versatility of the same signaling modality and reconstruction techniques. Non-destructive evaluation (NDE) of metal parts in the manufacturing and transportation sectors also stand to benefit from conformal array imaging in order to better detect flaws. Since specific imaging tasks require custom modifications to system parameters, the simulation work in this thesis may provide a valuable starting point for investigating the capabilities of new applications.

The following avenues may be of interest to future researchers seeking to extend the impact of current work and system development:

Volumetric Imaging and Display: The possibility of system integration with large 2D multistatic arrays lends itself to the investigation of 3D imaging. Since the theory for the 2D and 3D versions of coherent propagation differ only in minor ways, the work presented in this thesis can be expanded to 3 dimensions. Application-specific methods for displaying 3D images can also be investigated. For example, an outward-scanning cardiac catheter image set may benefit from a polar unwrapping algorithm that that displays blood vessel walls in 2D.

Periodic Motion Detection: In experiments involving many image reconstruction cycles for one setting, periodic movements can be detected by analyzing the FFT along a single pixel axis of a series of reconstructed images. For example, a blood vessel wall that moves into and out of a pixel may not be readily apparent

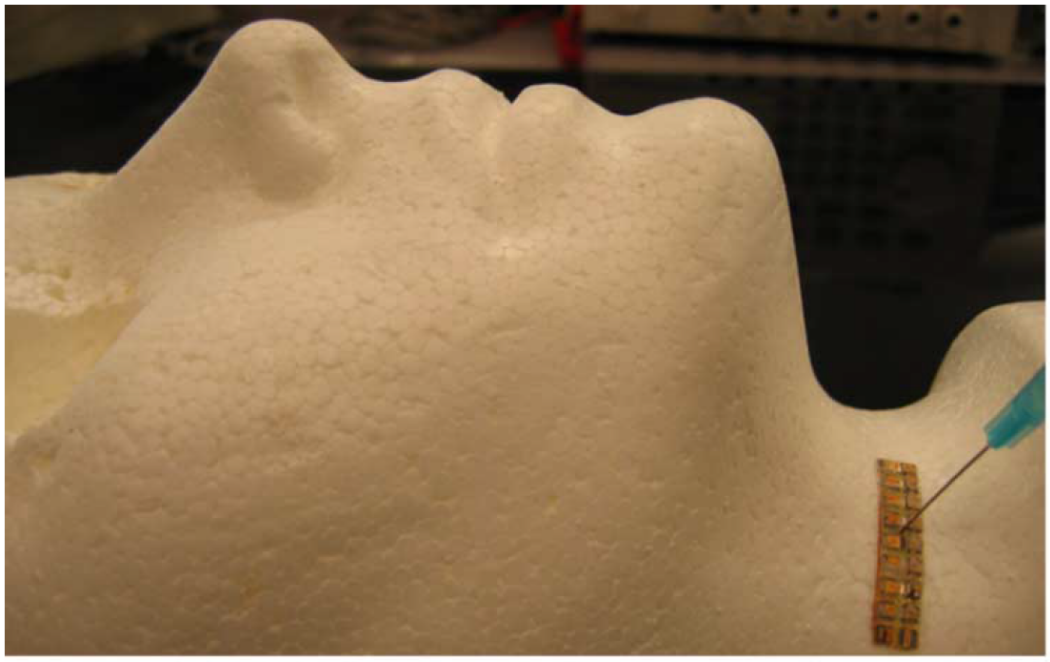

(a) Needle guidance procedure with neck imaging with a reconfigurable ultrasound array.

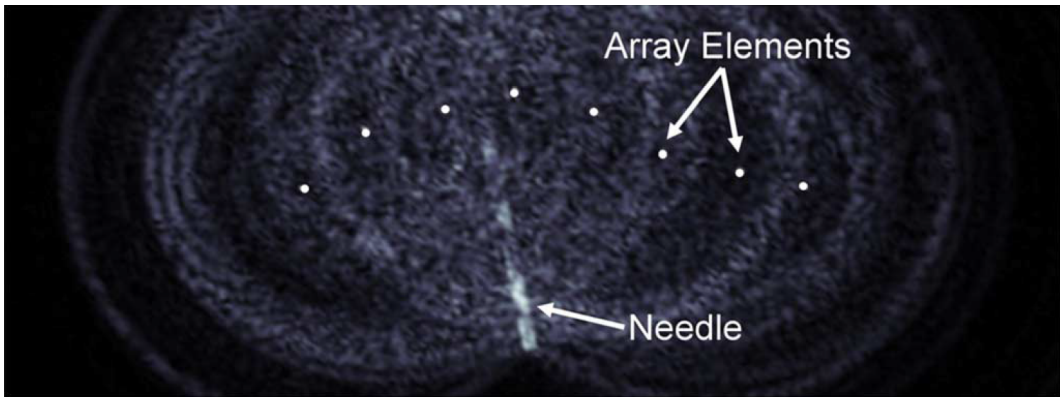

(b) Space-time stepped-FMCW imaging simulation at 2 MHz bandwidth of a 14-gauge needle target.

Figure 6.1: Simulation modeling for development of a needle guidance imaging system.

(a) Conformal array wrapped around a 9F (3 mm diameter) commercial intracardiac ultrasound catheter.

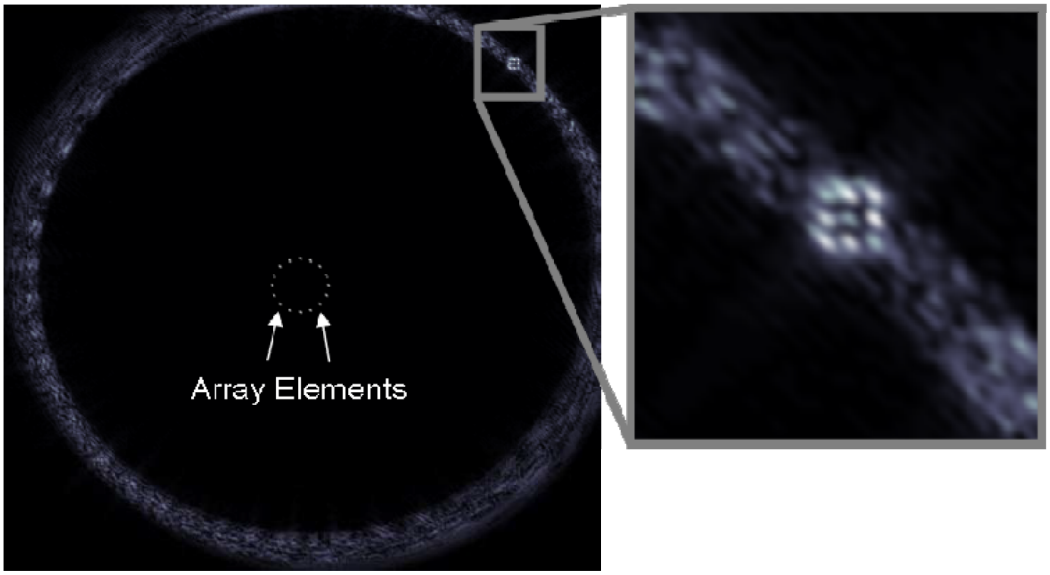

(b) Outward space-time stepped-FMCW imaging simulation at 3 MHz bandwidth of a set of 9 adjacent point targets. Array diameter is 6 mm.

Figure 6.2: Outward radial imaging with circular arrays.

by visual inspection. But with a set of reconstructed images, that pixel bin value will vary periodically. A visualization method for overlaying the magnitude of periodic motion onto an original image may be valuable for distinguishing between normal and abnormal organ function.

Array Configuration Detection: Knowledge of the relative spatial positions of array elements is critical for image reconstruction and the physical development of a detection scheme may not be trivial. One method could involve fabricating an array such that the elements are fixed onto a metal or plastic grid of movable joints. Hinges at these joints have potentiometers whose resistance varies predictably as a function of hinge angle. By continuously sampling resistances at all joints, the configuration of the array can be calculated. A more rudimentary starting point might involve a grid design with joints that hold at only discrete angles. In addition to relative element positioning, detection of array movement *as a whole* is also a desirable system feature. This would permit synthetic aperture data acquisition by gliding the array over a surface and then registering together the collected data. Integrating one or more optical sensors (similar to those used in computer mice) underneath the array facing the imaging surface, would allow the array elements to be tracked across a given path.

Alternate Signaling Methods: One concern regarding the multistatic operation is whether the acoustic energy generated by a single transmitting element

is adequate for effective imaging. Wave attenuation in tissue limits depth of penetration which in turn limits imaging depth. For this reason, investigation into offshoot methods of signaling may offer solutions to these problems should they arise. For instance, Daher and Yen [10] have experimented with using entire rows of array elements for simultaneous transmission and reception instead of individual elements. Similar techniques present tradeoffs between computation time reduction and resolution, the acceptable combination of which is largely dictated by application.

Bibliography

[1] Ian F. Akyildiz, Dario Pompili, and Tommaso Melodia. Underwater acoustic sensor networks: Research challenges. *Ad Hoc Networks (Elsevier)*, 3:257–279, 2005.

[2] Ultrasound Institute at the University of South Carolina School of Medicine. Neck ultrasound probe, 2014.

[3] R.S. Blum. Distributed detection for diversity reception of fading signals in noise. *Information Theory, IEEE Transactions on*, 45(1):158–164, Jan 1999.

[4] R.S. Blum, S.A. Kassam, and H.V. Poor. Distributed detection with multiple sensors i. advanced topics. *Proceedings of the IEEE*, 85(1):64–79, Jan 1997.

[5] Xiuzhen Cheng, Haining Shu, Qilian Liang, and D.H.-C. Du. Silent positioning in underwater acoustic sensor networks. *Vehicular Technology, IEEE Transactions on*, 57(3):1756–1766, May 2008.

[6] V.S. Chernyak. *Fundamentals of Multisite Radar Systems: Multistatic Radars and Multistatic Radar Systems*. Taylor & Francis, 1998.

[7] D. Christensen. *Ultrasonic Bioinstrumentation*. Wiley, 1988.

[8] Martin O Culjat, David B Bennett, Michael Lee, Elliott R Brown, Hua Lee, Warren S Grundfest, and Rahul S Singh. Polyimide-based conformal ultrasound transducer array for needle guidance. *Sensors Journal, IEEE*, 9(10):1244–1245, 2009.

[9] Martin O Culjat, Aaron E Dann, Michael Lee, David B Bennett, Peter G Schulam, Hua Lee, WS Grundfest, and Rahul S Singh. Transurethral ultrasound catheter-based transducer with flexible polyimide joints. In *Ultrasonics Symposium (IUS), 2009 IEEE International*, pages 2209–2212. IEEE, 2009.

[10] N.M. Daher and J.T. Yen. 2-D array for 3-D ultrasound imaging using synthetic aperture techniques. *Ultrasonics, Ferroelectrics, and Frequency Control, IEEE Transactions on*, 53(5):912–924, May 2006.

[11] A. Dogandzic and Arye Nehorai. Cramer-Rao bounds for estimating range, velocity, and direction with an active array. *Signal Processing, IEEE Transactions on*, 49(6):1122–1137, Jun 2001.

[12] Lin Du, Jian Li, and Petre Stoica. User parameter free approaches to multistatic adaptive ultrasound imaging. In *Biomedical Imaging: From Nano to Macro, 2008. ISBI 2008. 5th IEEE International Symposium on*, pages 1287–1290, May 2008.

[13] Francis A. Duck, A.C Baker, and H.C. Starritt. *Ultrasound in Medicine*. Medical science series. Taylor & Francis, 1998.

[14] M. Erol-Kantarci, H.T. Mouftah, and S. Oktug. Localization techniques for underwater acoustic sensor networks. *Communications Magazine, IEEE*, 48(12):152–158, December 2010.

[15] M. Erol-Kantarci, H.T. Mouftah, and S. Oktug. A survey of architectures and localization techniques for underwater acoustic sensor networks. *Communications Surveys Tutorials, IEEE*, 13(3):487–502, Third 2011.

[16] Anthony J. Fischetti and Richard C. Scott. Basic ultrasound beam formation and instrumentation. *Clinical Techniques in Small Animal Practice*, 22(3):90 – 92, 2007.

[17] E. Fishler, A Haimovich, R.S. Blum, L.J. Cimini, D. Chizhik, and R.A Valenzuela. Spatial diversity in radars — models and detection performance. *Signal Processing, IEEE Transactions on*, 54(3):823–838, March 2006.

[18] M.T. Frankford, K.B. Stewart, N. Majurec, and J.T. Johnson. Numerical and experimental studies of target detection with MIMO radar. *Aerospace and Electronic Systems, IEEE Transactions on*, 50(2):1569–1577, April 2014.

[19] H. Godrich, A.M. Haimovich, and R.S. Blum. Cramer Rao bound on target localization estimation in MIMO radar systems. In *Information Sciences and Systems, 2008. CISS 2008. 42nd Annual Conference on*, pages 134–139, March 2008.

[20] Ali Cafer Gurbuz, James H McClellan, and Waymond R Scott. A compressive sensing data acquisition and imaging method for stepped frequency GPRs. *Signal Processing, IEEE Transactions on*, 57(7):2640–2650, 2009.

[21] A.M. Haimovich, R.S. Blum, and L.J. Cimini. MIMO radar with widely separated antennas. *Signal Processing Magazine, IEEE*, 25(1):116–129, 2008.

[22] A. Hassanien and S.A. Vorobyov. Phased-MIMO radar: A tradeoff between phased-array and MIMO radars. *Signal Processing, IEEE Transactions on*, 58(6):3137–3151, June 2010.

[23] Siemens Healthcare Inc. Abdomen probe, 2014.

[24] Siemens Healthcare Inc. Ultrasound image of fetus in womb, 2014.

[25] G. Isbitiren and O.B. Akan. Three-dimensional underwater target tracking with acoustic sensor networks. *Vehicular Technology, IEEE Transactions on*, 60(8):3897–3906, Oct 2011.

[26] Don H. Johnson and Dan E. Dudgeon. *Array Signal Processing: Concepts and Techniques*. Simon & Schuster, 1992.

[27] J.A. Johnson, Mustafa Karaman, and B.T. Khuri-Yakub. Coherent-array imaging using phased subarrays. Part I: Basic principles. *Ultrasonics, Ferroelectrics, and Frequency Control, IEEE Transactions on*, 52(1):37–50, Jan 2005.

[28] J.A. Johnson, O. Oralkan, S. Ergun, U. Demirci, Mustafa Karaman, and B.T. Khuri-Yakub. Coherent array imaging using phased subarrays. Part II: Simulations and experimental results. *Ultrasonics, Ferroelectrics, and Frequency Control, IEEE Transactions on*, 52(1):51–64, Jan 2005.

[29] Mustafa Karaman, Ira O Wygant, Ömer Oralkan, and Butrus T Khuri-Yakub. Minimally redundant 2-D array designs for 3-D medical ultrasound imaging. *Medical Imaging, IEEE Transactions on*, 28(7):1051–1061, 2009.

[30] Steven M. Kay. *Fundamentals of Statistical Signal Processing: Estimation Theory*. Prentice-Hall, Inc., Upper Saddle River, NJ, USA, 1993.

[31] Hua Lee. Resolution trade-off analysis for aperture size and signaling bandwidth of diffraction tomography based on spatial-frequency spectral coverage. *International Journal of Imaging Systems and Technology*, 19(1):1–4, 2009.

[32] Michael Lee and Daniel Doonan. Estimation and correction of quadrature-receiver phase errors of stepped-frequency FMCW systems for high-resolution imaging. In *Proceedings of International Telemetering Conference*. International Foundation for Telemetering, 2012.

[33] Michael Lee and Daniel Doonan. Resolution analysis and system integration of a dynamically reconfigurable FMCW medical ultrasound imaging system. In *Proceedings of International Telemetering Conference*. International Foundation for Telemetering, 2012.

[34] Michael Lee, W. S. Grundfest, and Hua Lee. Image reconstruction and resolution enhancement algorithm for FMCW medical ultrasound imaging systems. In *Proceedings of International Telemetering Conference*. International Foundation for Telemetering, 2011.

[35] Michael Lee and Hua Lee. Modeling imaging performance of multistatic acoustic arrays of non-uniform geometries. *The Journal of the Acoustical Society of America*, 134(5):4170–4170, 2013.

[36] Michael Lee and Sashi Ono. Optimization and integration of high-performance ground penetrating imaging radar system: A research prototype. *International Journal of Imaging Systems and Technology*, 15(4):220–223, 2005.

[37] Michael Lee, Rahul S Singh, Martin O Culjat, Shyam Natarajan, Brian P Cox, Elliott R Brown, Warren S Grundfest, and Hua Lee. Space-time image reconstruction algorithm for diverse ultrasound transducer element distributions. In *Biomedical Imaging: From Nano to Macro, 2009. ISBI'09. IEEE International Symposium on*, pages 177–180. IEEE, 2009.

[38] Michael Lee, Rahul S Singh, Martin O Culjat, Shyam Natarajan, Brian P Cox, Elliott R Brown, Warren S Grundfest, and Hua Lee. Waveform synthesis for the design and image reconstruction of step FMCW ultrasound imaging systems with conformal transducer arrays. In *SPIE Medical Imaging*, pages 72650C–72650C. International Society for Optics and Photonics, 2009.

[39] Michael Lee, Rahul S Singh, Martin O Culjat, Scott Stubbs, Shyam Natarajan, Elliott R Brown, Warren S Grundfest, and Hua Lee. Designing multistatic ultrasound imaging systems using software analysis. In *SPIE Medical Imaging*, pages 76290S–76290S. International Society for Optics and Photonics, 2010.

[40] N.H. Lehmann, A.M. Haimovich, R.S. Blum, and L. Cimini. High resolution capabilities of MIMO radar. In *Signals, Systems and Computers, 2006. ACSSC '06. Fortieth Asilomar Conference on*, pages 25–30, Oct 2006.

[41] Timothy G. Leighton. What is ultrasound? *Progress in Biophysics and Molecular Biology*, 93(13):3 – 83, 2007.

[42] Y. Liu, Y.K. Deng, R. Wang, and X. Wang. Signal mode and imaging algorithn for spaceborne interrupted continuous-wave synthetic aperture radar. *Radar, Sonar Navigation, IET*, 6(5):348–358, June 2012.

[43] L. Maslikowski, P. Samczynski, M. Baczyk, P. Krysik, and K. Kulpa. Passive bistatic sar imaging x2014; challenges and limitations. *Aerospace and Electronic Systems Magazine, IEEE*, 29(7):23–29, July 2014.

[44] Shyam Natarajan, Rahul S Singh, Michael Lee, Brian P Cox, Martin O Culjat, Warren S Grundfest, and Hua Lee. Accurate step-FMCW ultrasound ranging and comparison with pulse-echo signaling methods. In *SPIE Medical Imaging*, pages 76290D–76290D. International Society for Optics and Photonics, 2010.

[45] Shyam Natarajan, Rahul S Singh, Michael Lee, Brian P Cox, Martin O Culjat, Hua Lee, and Warren S Grundfest. Step-FMCW signaling and target detection for ultrasound imaging systems with conformal transducer arrays. In *BiOS*, pages 75550M–75550M. International Society for Optics and Photonics, 2010.

[46] Guillaume Neau and Deborah Hopkins. The promise of ultrasonic phased arrays and the role of modeling in specifying systems. In *Proc. ASNT Fall Conference & Quality Testing Show, Houston*, pages 23–27, 2006.

[47] Alan V. Oppenheim, Ronald W. Schafer, and John R. Buck. *Discrete-time Signal Processing (2nd Ed.)*. Prentice-Hall, Inc., Upper Saddle River, NJ, USA, 1999.

[48] C. Podilchuk, M. Bajor, W. Stoddart, L. Barinov, W. Hulbert, A. Jairaj, and R. Mammone. Speckle reduction using stepped-frequency continuous wave ultrasound. In *Signal Processing in Medicine and Biology Symposium (SPMB), 2012 IEEE*, pages 1–4, Dec 2012.

[49] T. Rastello, C. Haas, D. Vray, M. Krueger, K. Schroeder, E. Brusseau, G. Gimenez, and H. Ermert. A new fourier-based multistatic synthetic aperture focusing technique for intravascular ultrasound imaging. In *Ultrasonics Symposium, 1998. Proceedings., 1998 IEEE*, volume 2, pages 1725–1728 vol.2, 1998.

[50] M. Rodriguez-Cassola, P. Prats-Iraola, G. Krieger, A. Reigber, and A. Moreira. Bistatic SAR image formation: A systematic approach. In *Geoscience and Remote Sensing Symposium (IGARSS), 2014 IEEE International*, pages 3945–3948, July 2014.

[51] L.L. Scharf and C. Demeure. *Statistical Signal Processing: Detection, Estimation, and Time Series Analysis*. Addison-Wesley series in electrical and computer engineering. Addison-Wesley Publishing Company, 1991.

[52] Rahul S Singh, Shyam Natarajan, Michael Lee, AE Dann, Brian P Cox, David B Bennett, Elliott R Brown, Hua Lee, Warren S Grundfest, and Martin O Culjat. Development of an ultrasound imaging system for needle guidance. In *Ultrasonics Symposium (IUS), 2009 IEEE International*, pages 1852–1855. IEEE, 2009.

[53] M.H. Skjelvareid, Y. Birkelund, and Y. Larsen. Synthetic aperture focusing of outwardly directed cylindrical ultrasound scans. *Ultrasonics, Ferroelectrics, and Frequency Control, IEEE Transactions on*, 59(11):2460–2469, November 2012.

[54] M.I. Skolnik. *Introduction to Radar Systems*. Electrical engineering series. McGraw-Hill, 2001.

[55] Mehrdad Soumekh. Bistatic synthetic aperture radar inversion with application in dynamic object imaging. *Signal Processing, IEEE Transactions on*, 39(9):2044–2055, 1991.

[56] Mehrdad Soumekh. *Fourier Array Imaging*. Prentice-Hall, Inc., Upper Saddle River, NJ, USA, 1994.

[57] Tadeusz Stepinski. An implementation of synthetic aperture focusing technique in frequency domain. *Ultrasonics, Ferroelectrics and Frequency Control, IEEE Transactions on*, 54(7):1399–1408, 2007.

[58] T.L. Szabo. *Diagnostic Ultrasound Imaging: Inside Out*. Academic Press series in biomedical engineering. Elsevier Academic Press, 2004.

[59] Y Tasinkevych, I Trots, A Nowicki, and PA Lewin. Modified synthetic transmit aperture algorithm for ultrasound imaging. *Ultrasonics*, 52(2):333–342, 2012.

[60] R. Viswanathan and P.K. Varshney. Distributed detection with multiple sensors i. fundamentals. *Proceedings of the IEEE*, 85(1):54–63, Jan 1997.

[61] D. Vray, C. Haas, T. Rastello, M. Krueger, E. Brusseau, K. Schroeder, G. Gimenez, and Helmut Ermert. Synthetic aperture-based beam compression for intravascular ultrasound imaging. *Ultrasonics, Ferroelectrics, and Frequency Control, IEEE Transactions on*, 48(1):189–201, Jan 2001.

[62] V.T. Vu, T.K. Sjogren, and M.I. Pettersson. Fast backprojection algorithm for UWB bistatic SAR. In *Radar Conference (RADAR), 2011 IEEE*, pages 431–434, May 2011.

[63] V.T. Vu, T.K. Sjogren, M.I. Pettersson, and H. Hellsten. An impulse response function for evaluation of UWB SAR imaging. *Signal Processing, IEEE Transactions on*, 58(7):3927–3932, July 2010.

[64] W.-Q. Wang. Phased-MIMO radar with frequency diversity for range-dependent beamforming. *Sensors Journal, IEEE*, 13(4):1320–1328, April 2013.

[65] Zhou Wang and AC. Bovik. A universal image quality index. *Signal Processing Letters, IEEE*, 9(3):81–84, March 2002.

[66] Zhou Wang, AC. Bovik, H.R. Sheikh, and E.P. Simoncelli. Image quality assessment: from error visibility to structural similarity. *Image Processing, IEEE Transactions on*, 13(4):600–612, April 2004.